A SUPER-RESOLUTION METHOD OF SOURCE RECONSTRUCTION USING NEAR FIELD ANTENNA MEASUREMENTS

Tapan K. Sarkar

Department of Electrical Engineering and Computer Science

Syracuse University, Syracuse, NY 13244 USA

Phone: + 315 443 3775, Fax: + 315 443 4441;

tksarkar@syr.edu

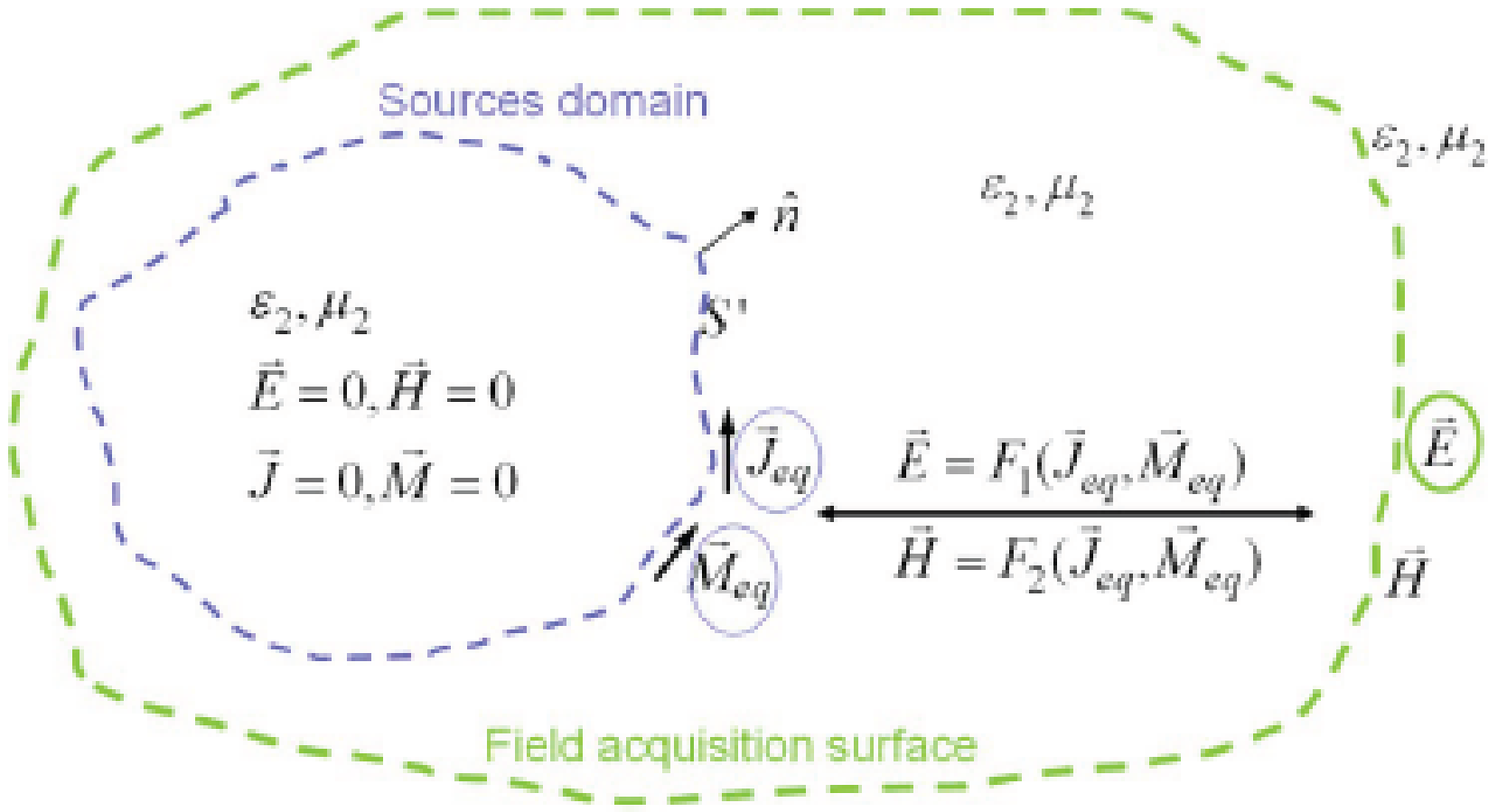

Fig. 2. Relationship between the field acquisition domain and the equivalent sources on their respective surfaces.

Sub-wavelength Imaging

1. **Fields need not be sampled at the Nyquist rate of 0.5λ. The fields can be computed further apart.**
2. **Existence of evanescent waves improves the resolution of the reconstruction of the sources. The presence of evanescent waves does not make the solution procedure unstable.**
3. **Sub-wavelength resolution of imaging as the sampling is relegated to the source plane.**
4. **Fields need not be measured on a canonical surface. It can be measured along a line, along a plane, or over an arbitrary shaped surface.**

Sub-wavelength Imaging

5. **No need to mechanically move a probe. One could place an array of receiving antennas.**
6. **Truncation error in the measurement has less influence on the accuracy of the source/far field reconstruction.**
7. **For planar measurement planes, this method is more accurate than the conventional Fourier techniques at the expense of 3 to 4 times slower computationally than the FFT as it is implemented through the conjugate gradient and the FFT technique.**

Sub-wavelength Imaging

8. **Can easily be extended to amplitude-only data measured over one plane or over multiple planes.**
9. **This methodology is based on Maxwellian Physics and therefore the transformations are quite accurate and in most cases even exact.**

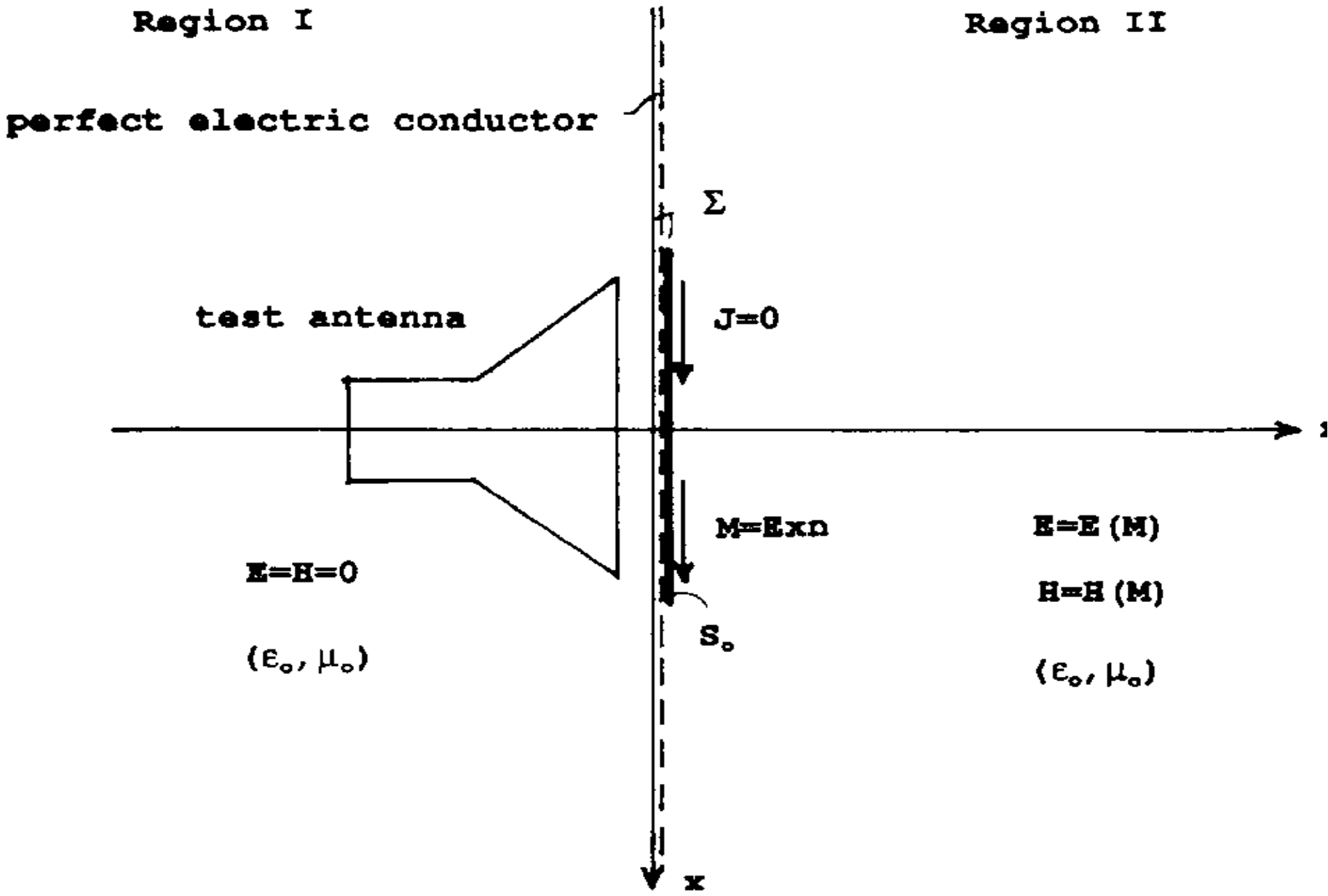

Figure 2: Equivalent Magnetic Current Approach

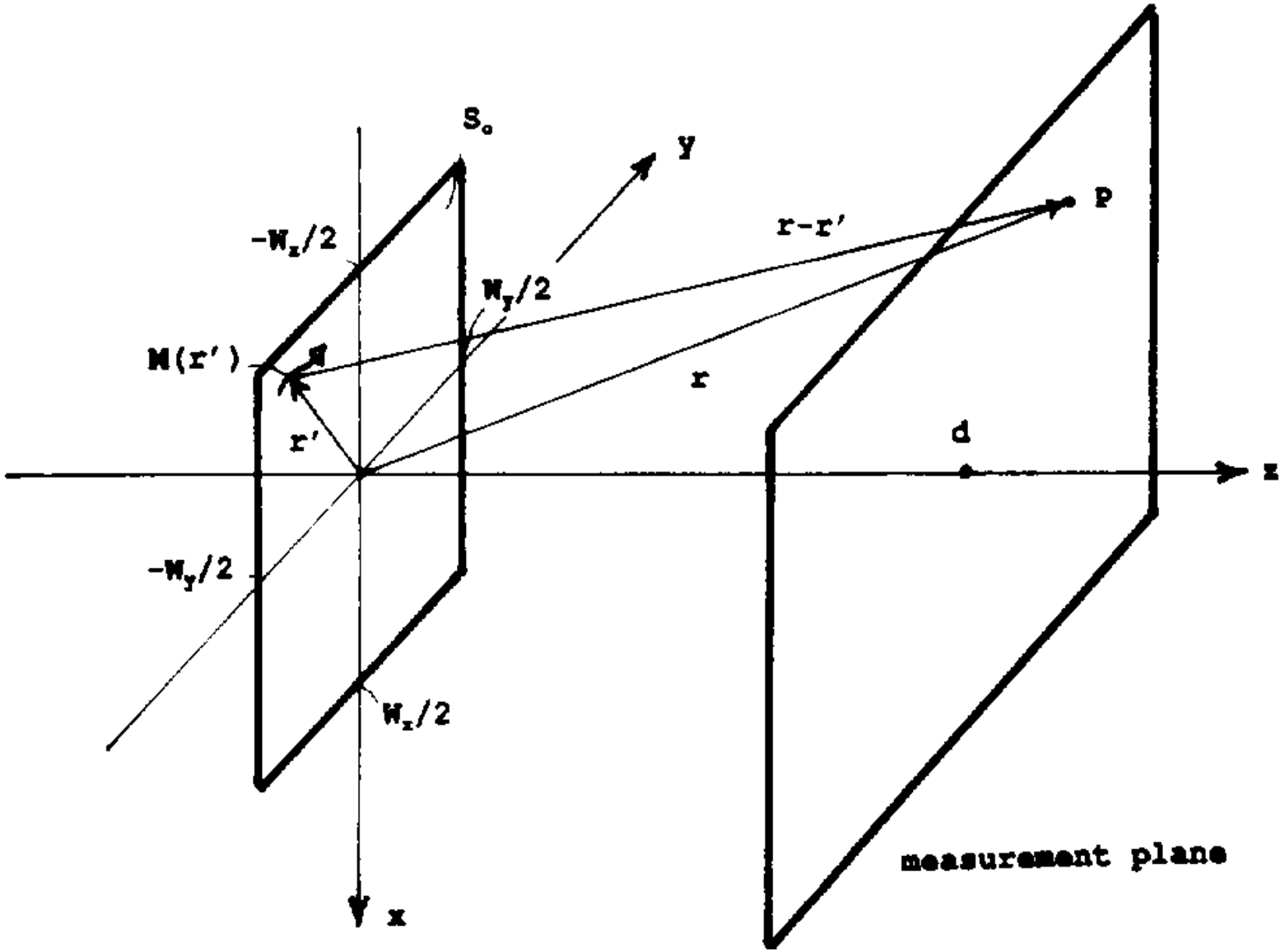

Figure 1: Planar Scanning

$$\overline{\mathbf{M}} = 2\overline{\mathbf{E}} \times \bar{n} \quad \text{on } S_0$$

$$\overline{\mathbf{E}}_{\text{meas}} = \overline{\mathbf{E}}(\overline{\mathbf{M}})$$

$$\overline{\mathbf{E}}(\bar{\mathbf{r}}) = -\int_{S_0}\int [\overline{\mathbf{M}}(\bar{\mathbf{r}}') \times \nabla' g(\bar{\mathbf{r}}, \bar{\mathbf{r}}')]\, ds'$$

$$g(\bar{\mathbf{r}}, \bar{\mathbf{r}}') = \frac{e^{-jk_0|\bar{\mathbf{r}} - \bar{\mathbf{r}}'|}}{4\pi|\bar{\mathbf{r}} - \bar{\mathbf{r}}'|}.$$

$$\begin{bmatrix} E_{\text{meas},\,x}(\bar{\mathbf{r}}) \\ E_{\text{meas},\,y}(\bar{\mathbf{r}}) \end{bmatrix}$$

$$= -\int_{S_0}\int \begin{bmatrix} 0 & \dfrac{\partial g(\bar{\mathbf{r}},\bar{\mathbf{r}}')}{\partial z'} \\ -\dfrac{\partial g(\bar{\mathbf{r}},\bar{\mathbf{r}}')}{\partial z'} & 0 \end{bmatrix} \begin{bmatrix} M_x(\bar{\mathbf{r}}') \\ M_y(\bar{\mathbf{r}}') \end{bmatrix} ds'.$$

$$E_{\text{meas},\,x}(\bar{\mathbf{r}}) = -\int_{S_0}\int \frac{\partial g(\bar{\mathbf{r}},\bar{\mathbf{r}}')}{\partial z'} M_y(\bar{\mathbf{r}}')\, ds'$$

$$E_{\text{meas},\,y}(\bar{\mathbf{r}}) = \int_{S_0}\int \frac{\partial g(\bar{\mathbf{r}},\bar{\mathbf{r}}')}{\partial z'} M_x(\bar{\mathbf{r}}')\, ds'.$$

$$M_x(x', y') = \sum_{i=1}^{M} \sum_{j=1}^{N} \alpha_{ij} \Pi_{ij}(x', y')$$

$$M_y(x', y') = \sum_{i=1}^{M} \sum_{j=1}^{N} \beta_{ij} \Pi_{ij}(x', y')$$

$$\Pi_{ij}(x', y') = \begin{cases} 1 & \text{if } x_i - \dfrac{\Delta x}{2} \le x' \le x_i + \dfrac{\Delta x}{2} \\ & y_j - \dfrac{\Delta y}{2} \le y' \le y_j + \dfrac{\Delta y}{2}, \\ & \text{and 0} \qquad \text{otherwise.} \end{cases}$$

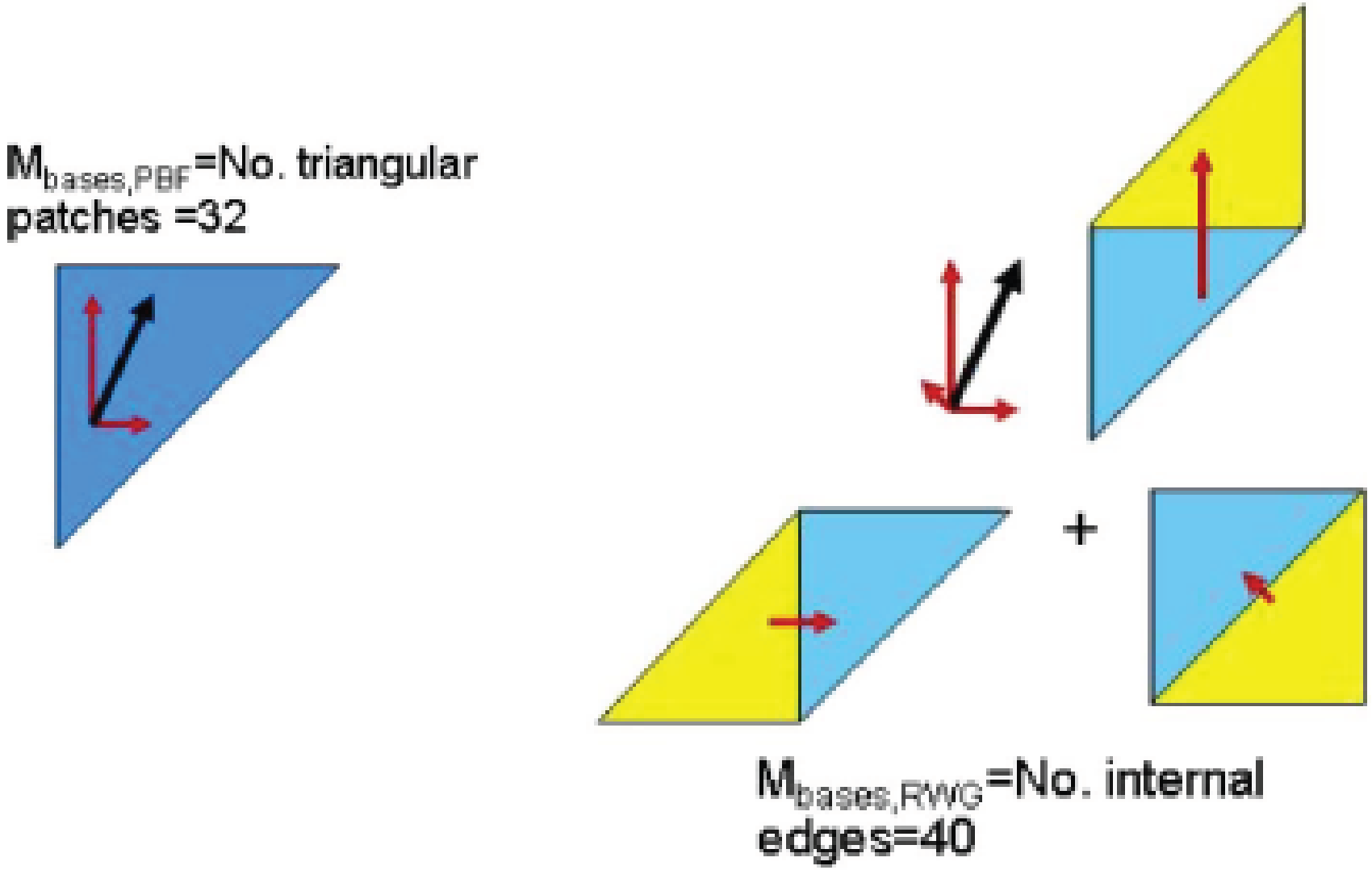

Fig. 4. Influence of the mesh edge orientation for expanding the currents using the RWG basis. (a) Some edges are coincident with the orientation of the currents. (b) Edges and currents do no have coincident orientations. (c) Definition of the current orientation when using the pulse basis. (d) Definition of the current orientation when using the RWG basis.

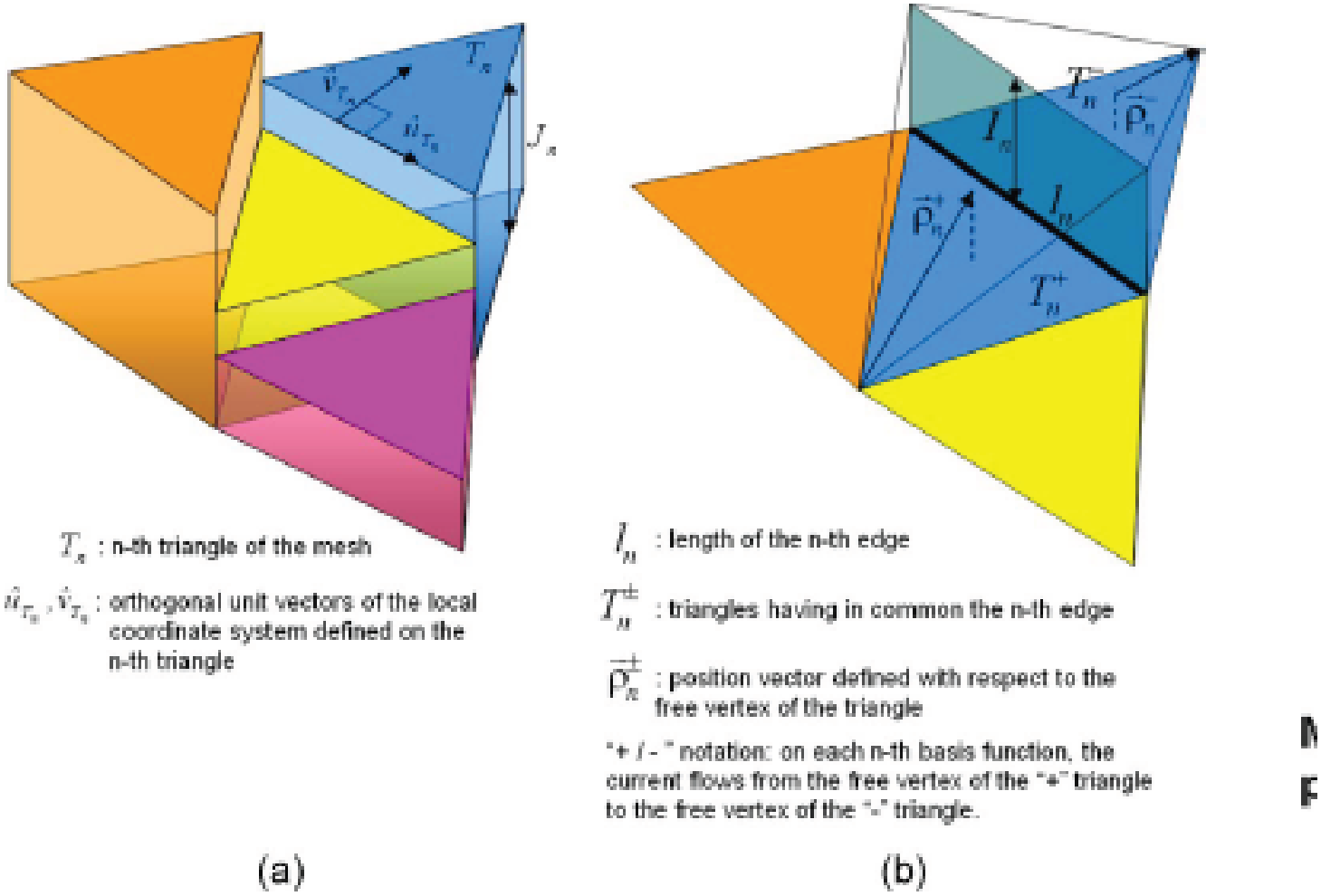

Fig. 3. Current expansion using (a) pulse basis functions and (b) RWG basis functions.

$$\mathbf{E}_{\text{meas},\,x} = -\mathbf{GM}_y$$

$$\mathbf{E}_{\text{meas},\,y} = \mathbf{GM}_x$$

$$\mathbf{G}_{k,l} = \int_{\Omega_l}\int \frac{e^{-jk_0R}}{4\pi R^2}(z_k - z')\left[jk_0 + \frac{1}{R}\right] ds'$$

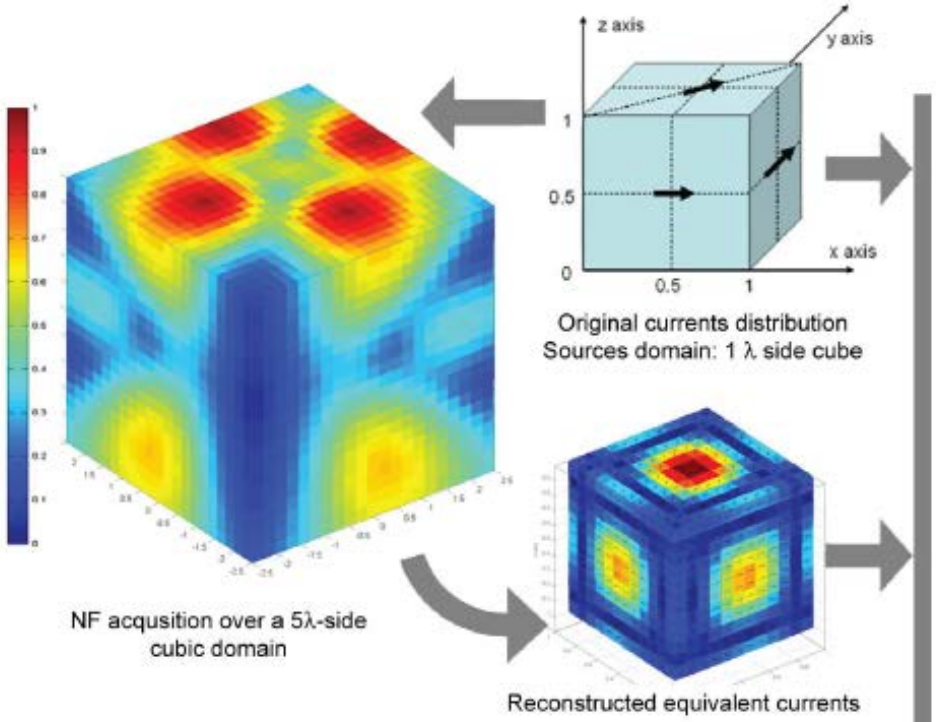

Original currents distribution
Sources domain: 1 λ side cube

NF acqusition over a 5λ-side cubic domain

Reconstructed equivalent currents

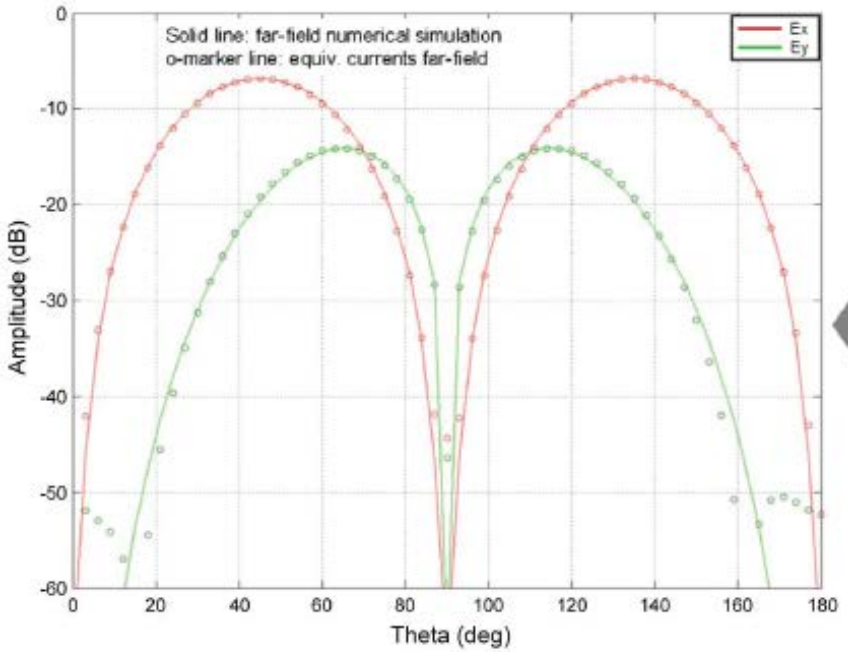

Radiation pattern: theoretical and calculated from equivalent currents

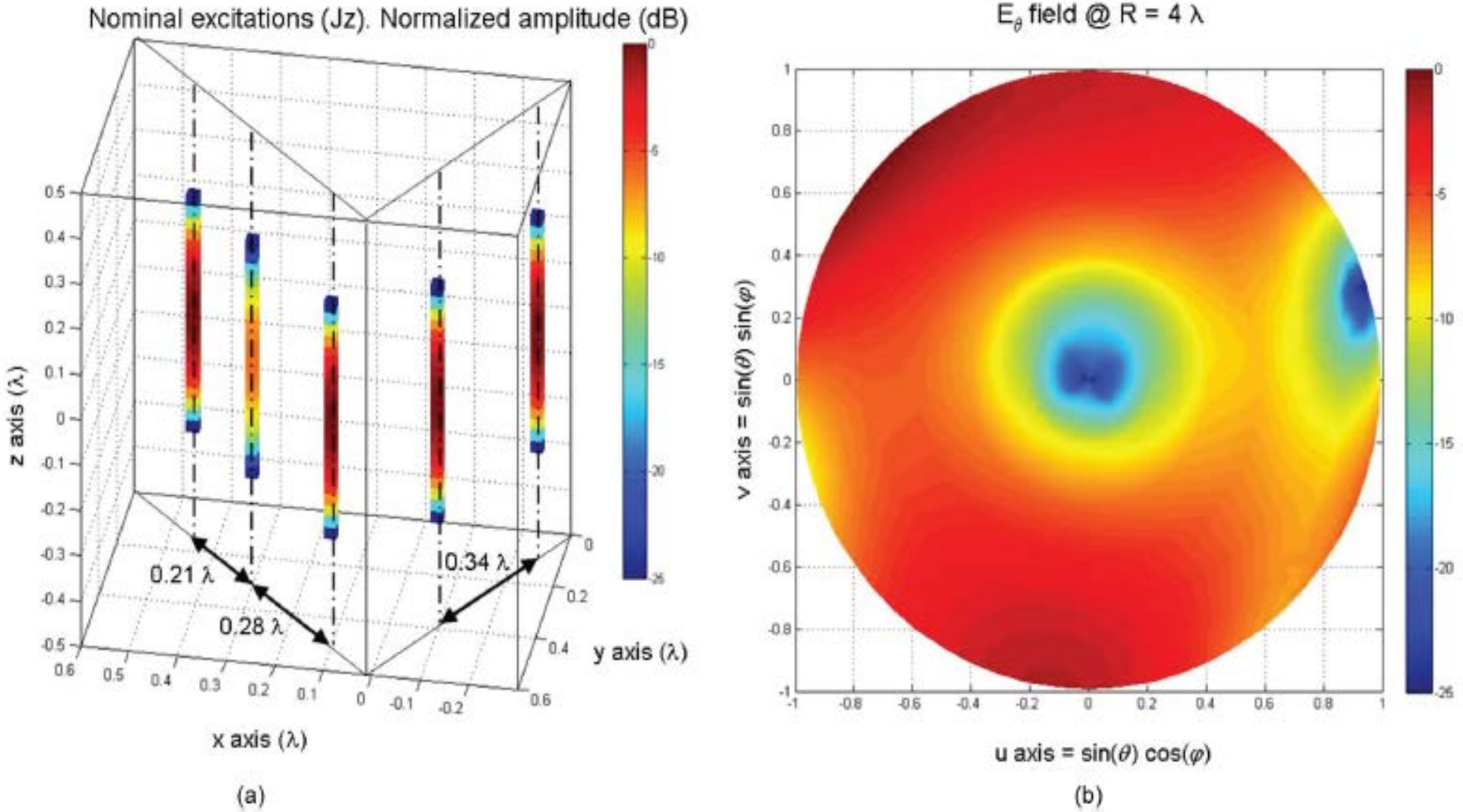

Fig. 5. (a) Array of five dipoles and the separation between them. (b) Field radiated by the array of dipoles (calculated at $R = 4\ \lambda$). E_θ component (normalized amplitude, in decibels). U–V representation.

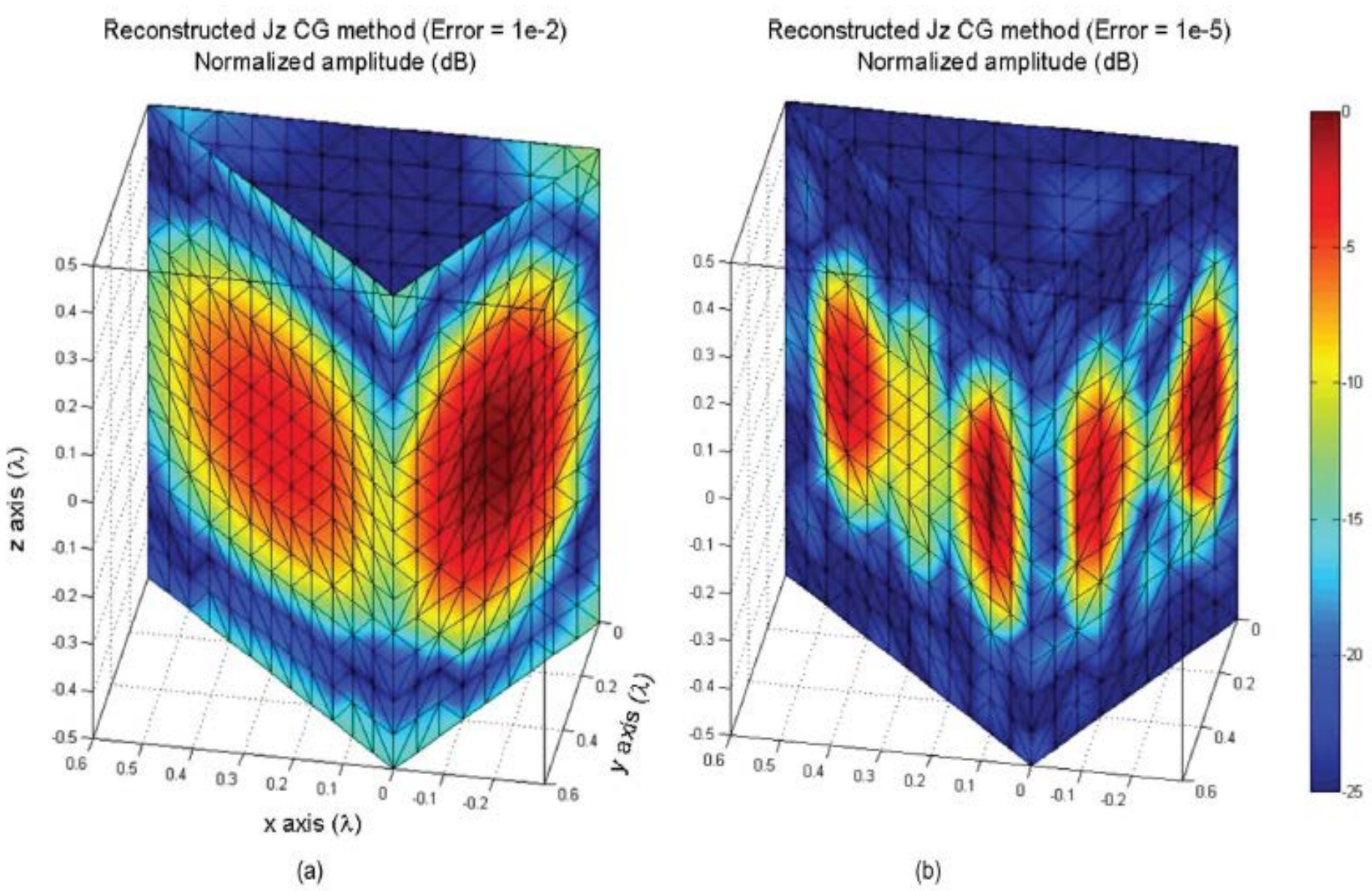

Fig. 8. Reconstructed equivalent electric currents when using the CG method. (a) Residuals $= 1e-2$. (b) Residuals $= 1e-5$.

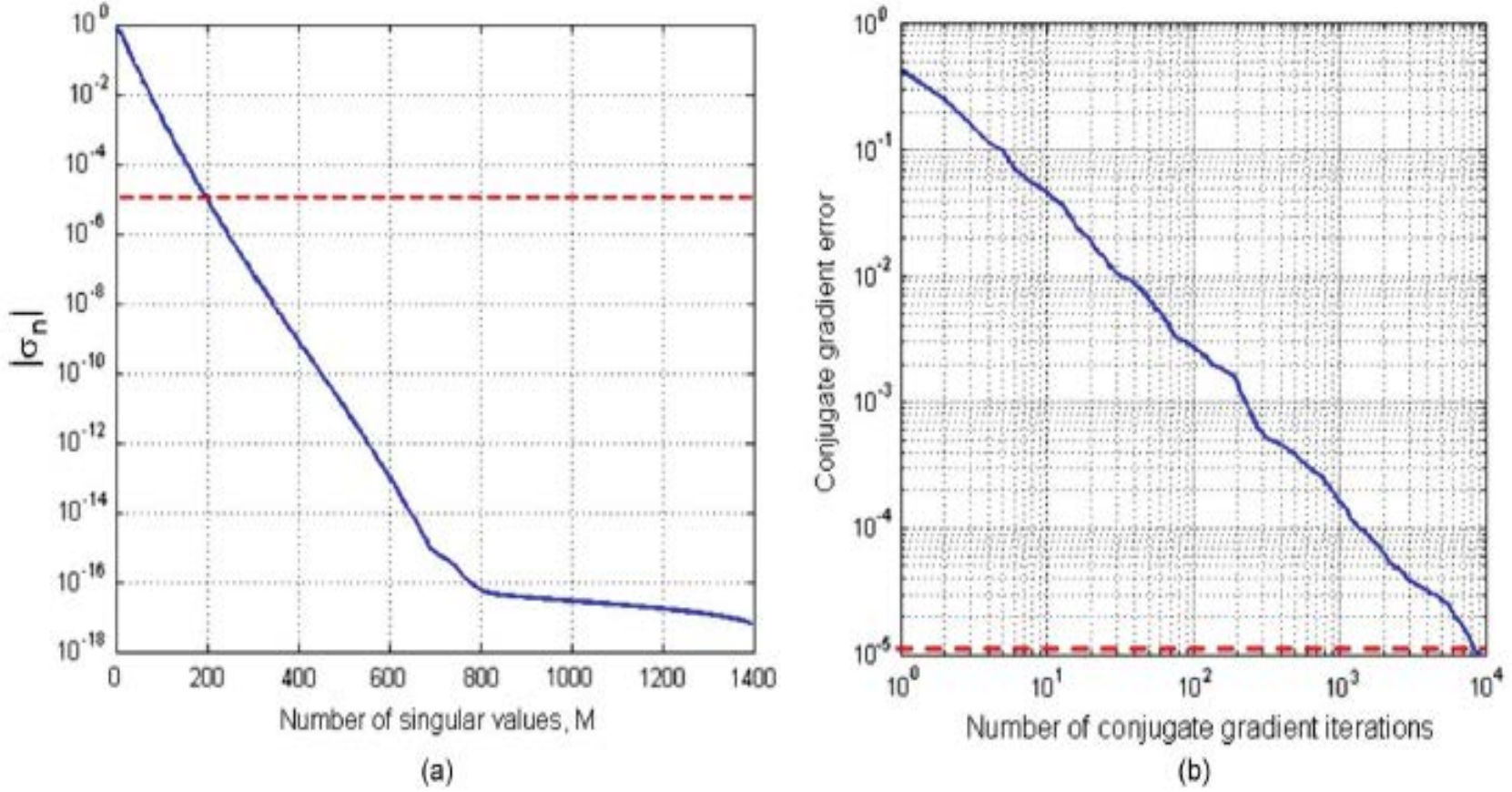

Fig. 6. (a) Number of singular values of the matrix. (b) Rate of convergence of the conjugate gradient method along with the residuals. The dashed red line represents the 1e − 5 threshold.

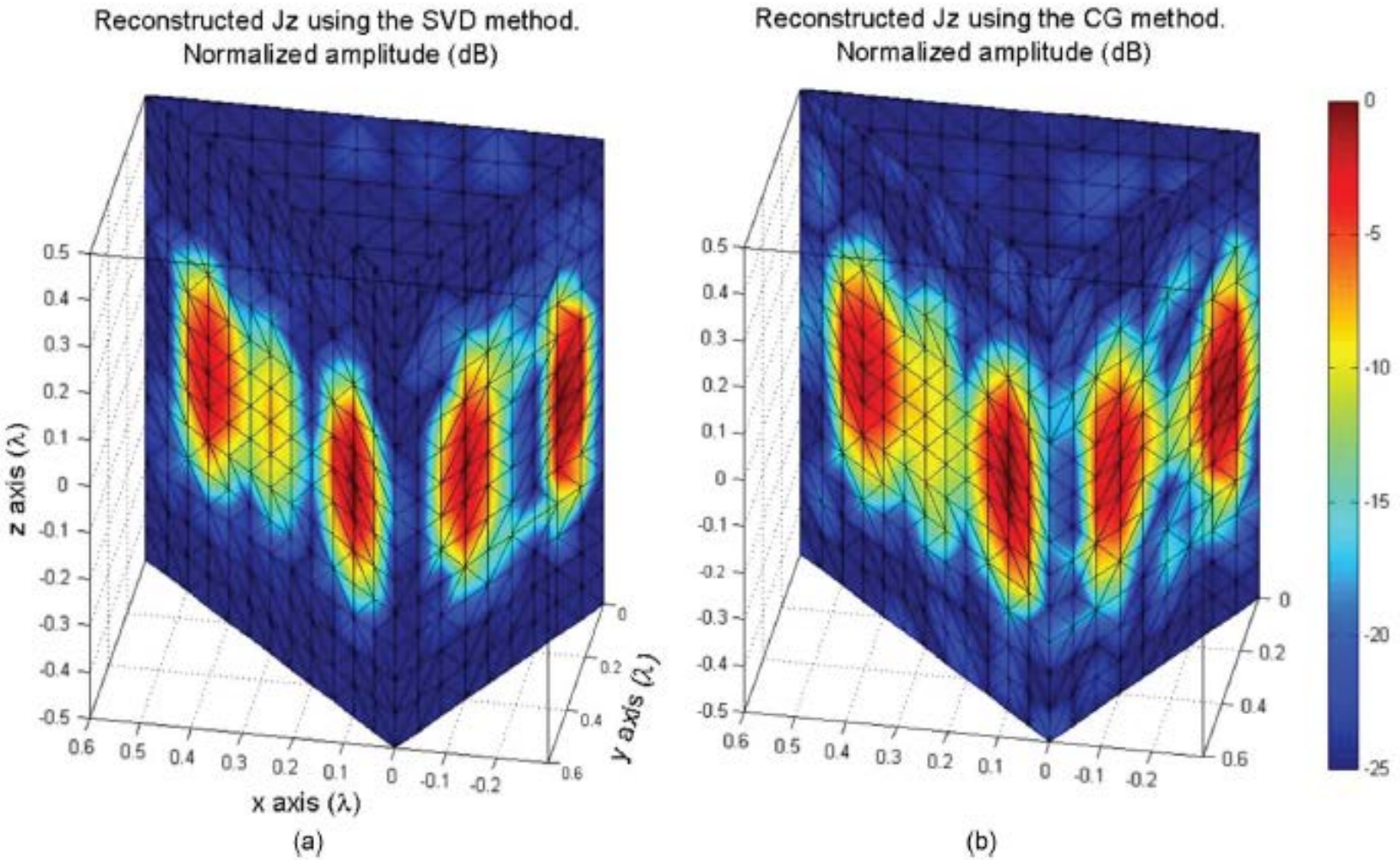

Fig. 7. Reconstructed equivalent electric currents using the simulated fields at $R = 4\ \lambda$. (a) Using the SVD (threshold at $\sigma_T = 1e-5$). (b) Generated by the CG method when solving the system of equations.

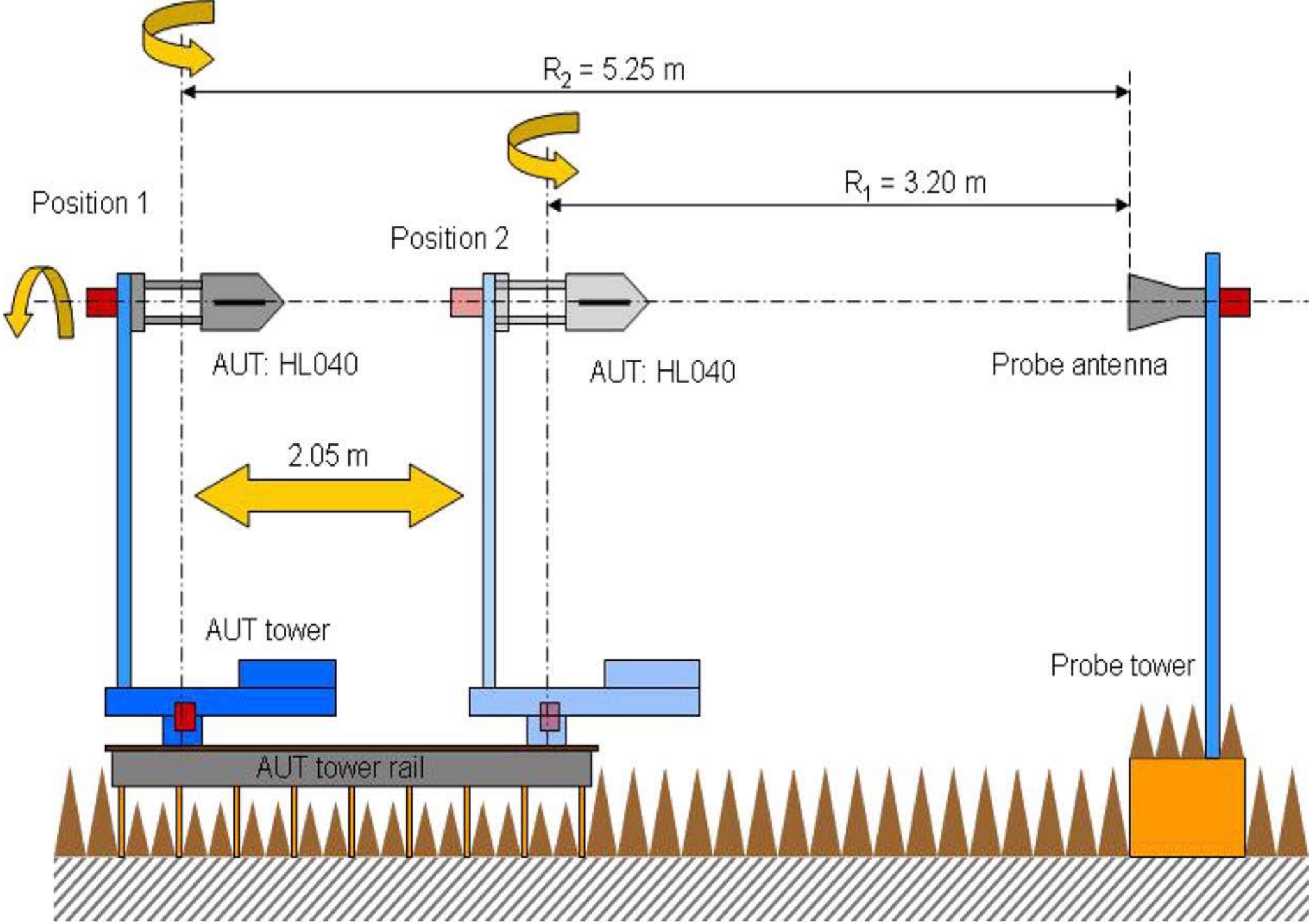

Antenna measurement in the anechoic chamber. Representation of the AUT tower displacement.

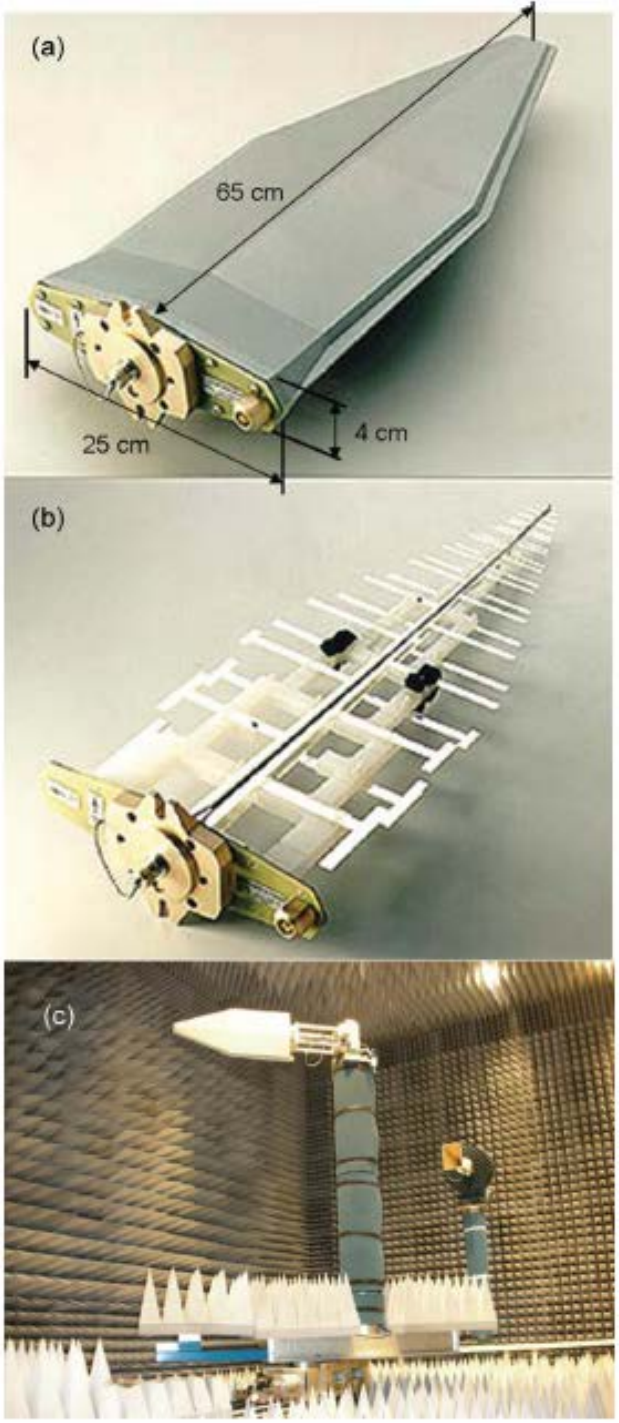
(a)
65 cm
25 cm
4 cm
(b)
(c)

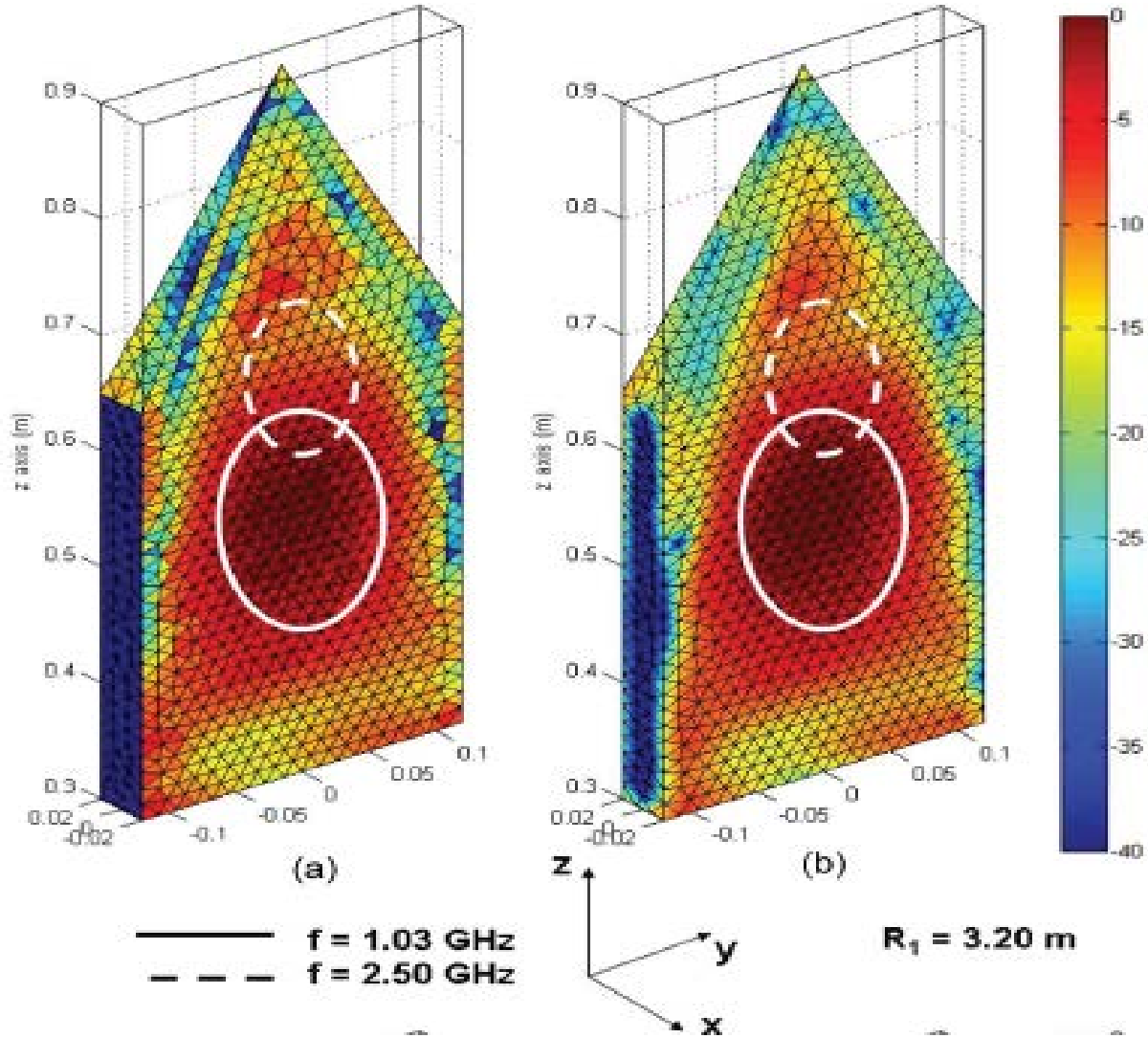

Fig. 13. Reconstructed equivalent currents. J_y component (normalized amplitude, in decibels). $R_1 = 3.20$ m: (a) $f = 1.03$ GHz, pulse basis; (b) $f = 1.03$ GHz, RWG basis; (c) $f = 2.50$ GHz, pulse basis; and (d) $f = 2.50$ GHz, RWG basis.

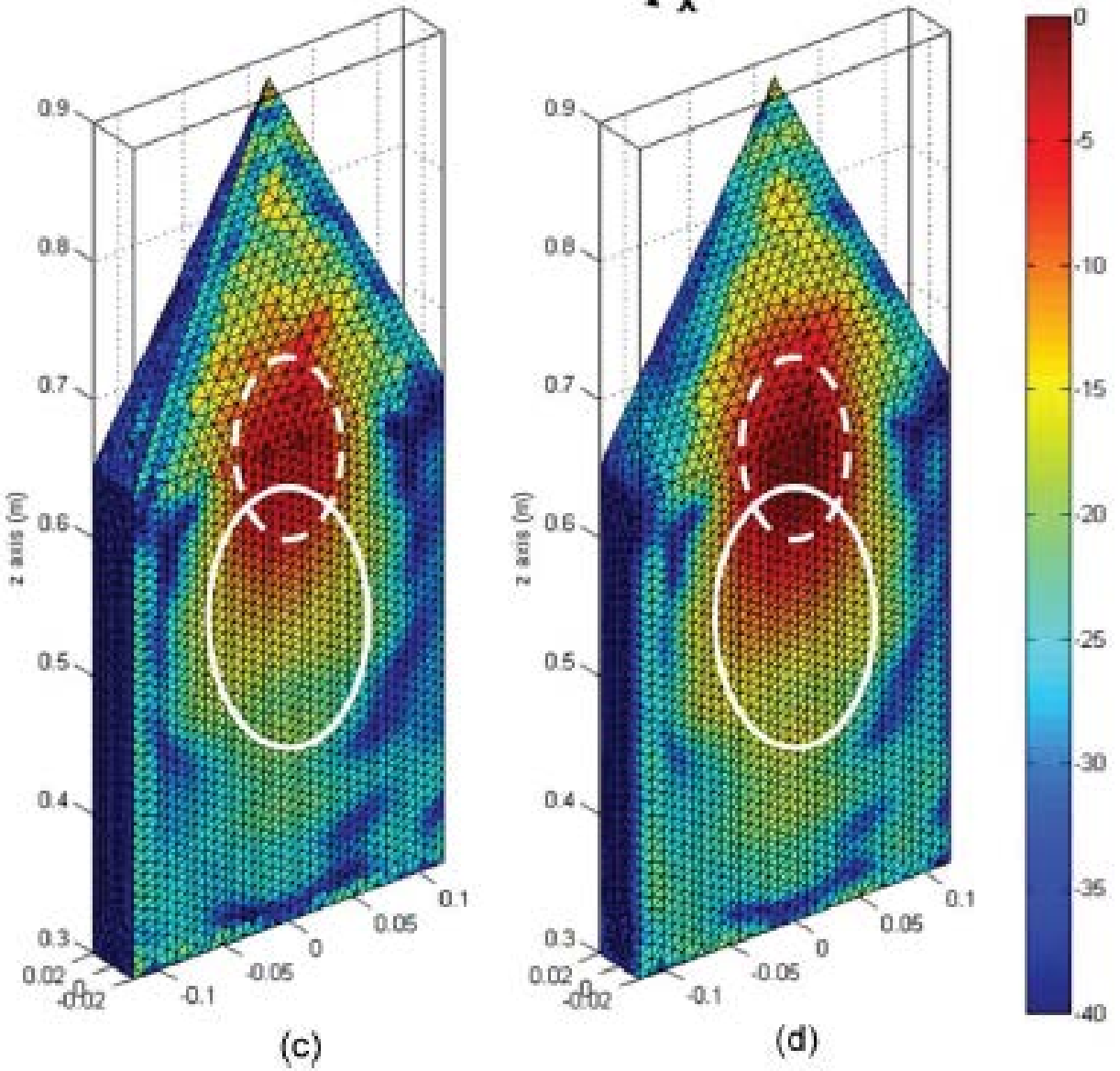

Fig. 13. Reconstructed equivalent currents. J_y component (normalized amplitude, in decibels). $R_1 = 3.20$ m: (a) $f = 1.03$ GHz, pulse basis; (b) $f = 1.03$ GHz, RWG basis; (c) $f = 2.50$ GHz, pulse basis; and (d) $f = 2.50$ GHz, RWG basis.

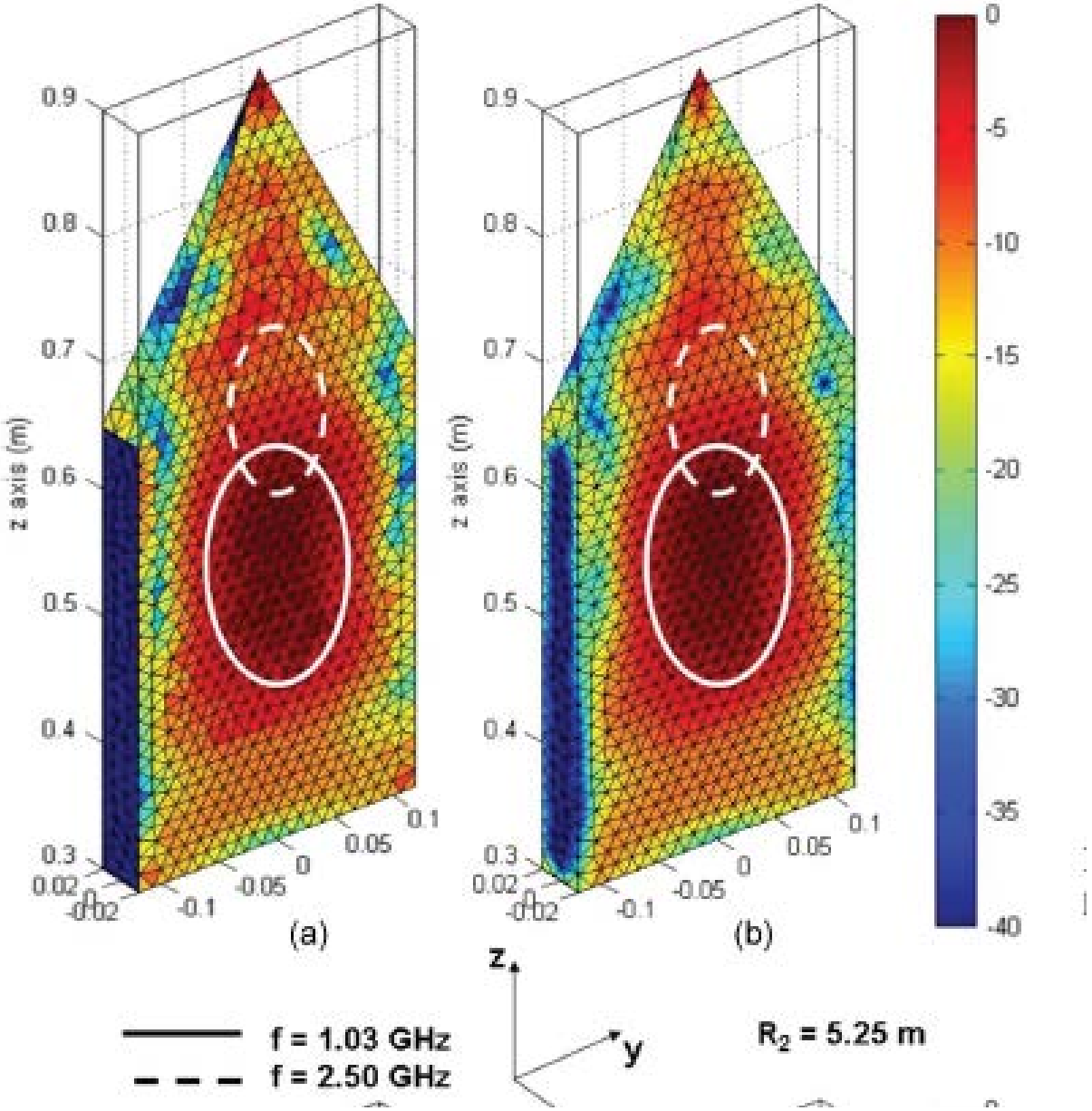

Fig. 14. Reconstructed equivalent currents. J_y component (normalized amplitude, in decibels). $R_2 = 5.25$ m: (a) $f = 1.03$ GHz, pulse basis; (b) $f = 1.03$ GHz, RWG basis; (c) $f = 2.50$ GHz, pulse basis; and (d) $f = 2.50$ GHz, RWG basis.

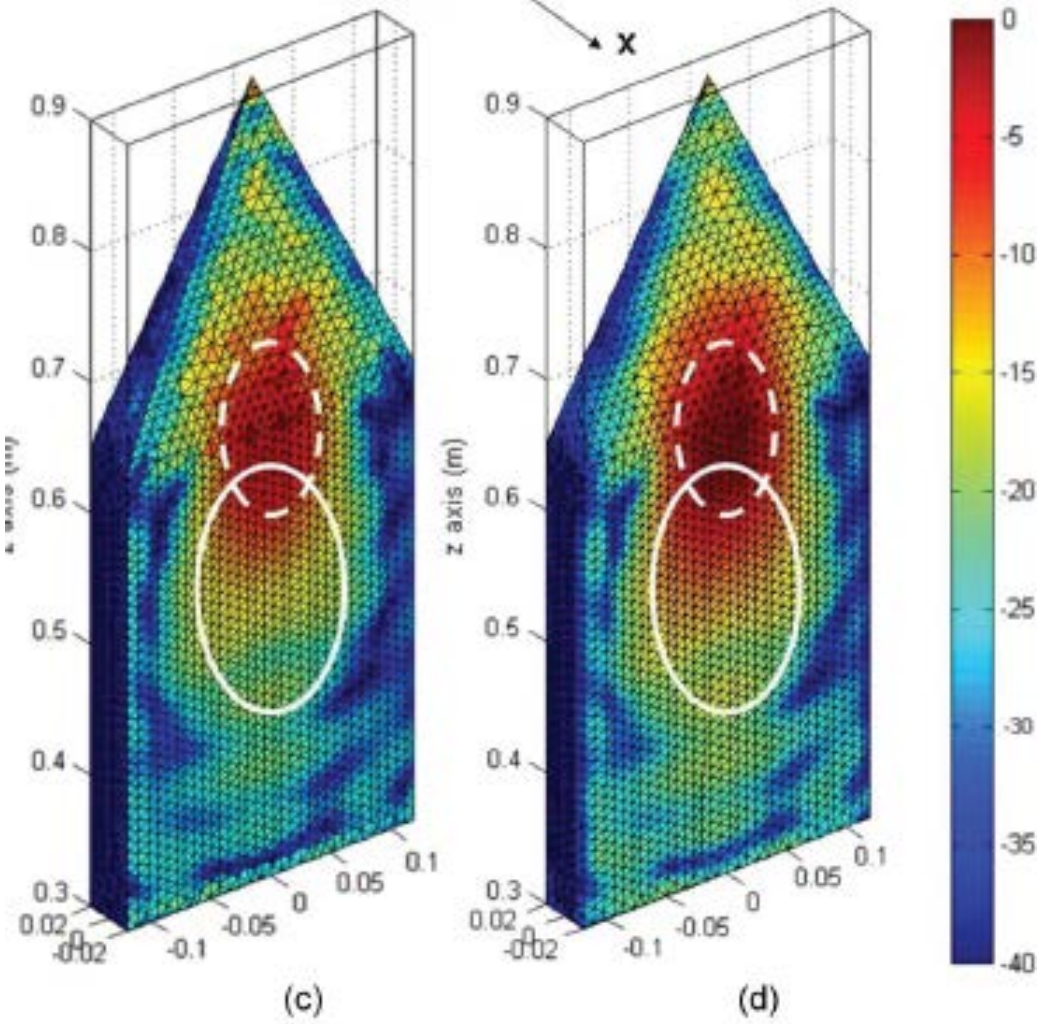

Fig. 14. Reconstructed equivalent currents. J_y component (normalized amplitude, in decibels). $R_2 = 5.25$ m: (a) $f = 1.03$ GHz, pulse basis; (b) $f = 1.03$ GHz, RWG basis; (c) $f = 2.50$ GHz, pulse basis; and (d) $f = 2.50$ GHz, RWG basis.

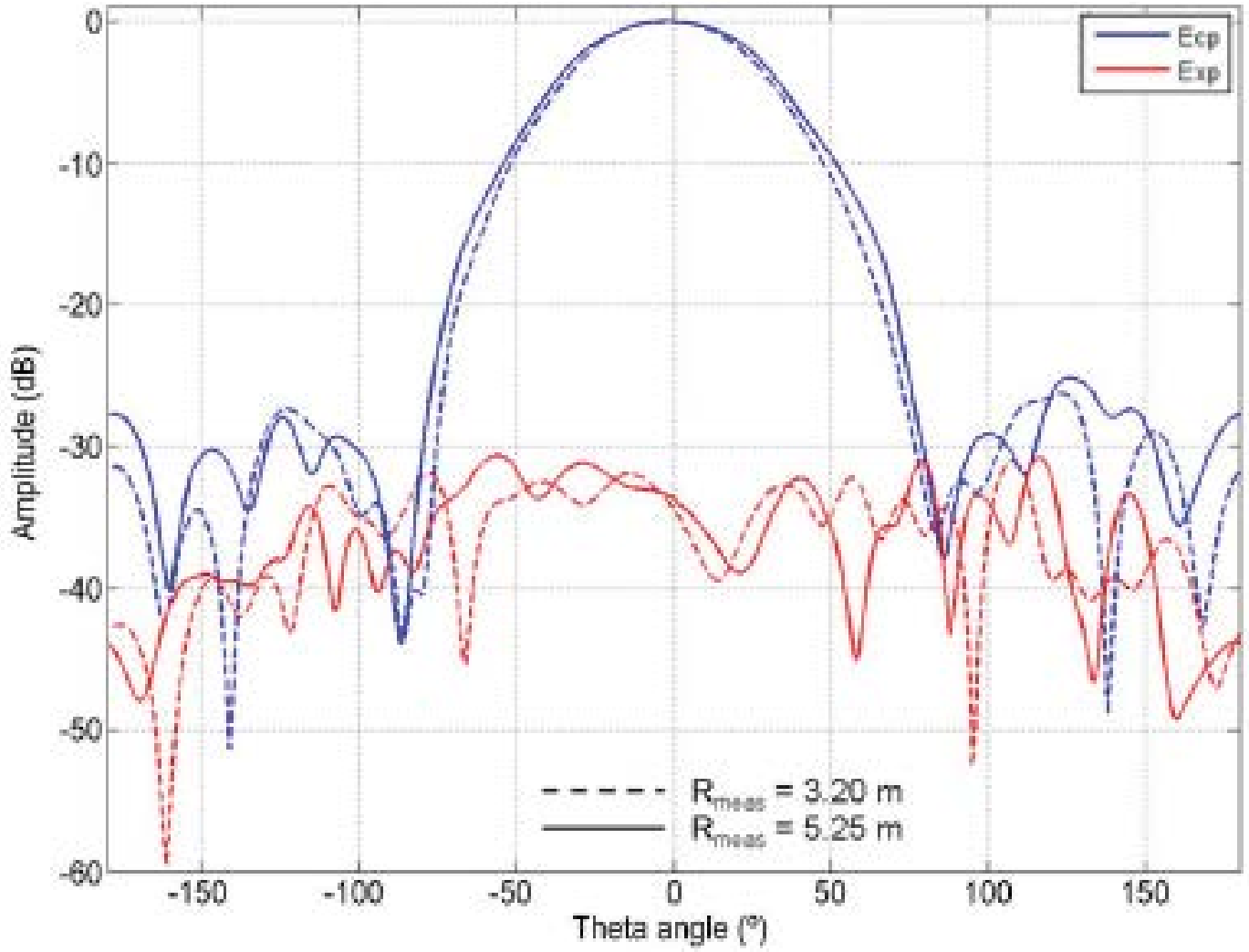

Fig. 11. Measured electric field (normalized amplitude, in decibels) at distances corresponding to $R_1 = 3.20$ m and $R_2 = 5.25$ m and plane $\varphi = 0°$. (a) $f = 1.03$ GHz. (b) $f = 2.50$ GHz. Blue line: field copolar component (E_y). Red line: field crosspolar component (E_x).

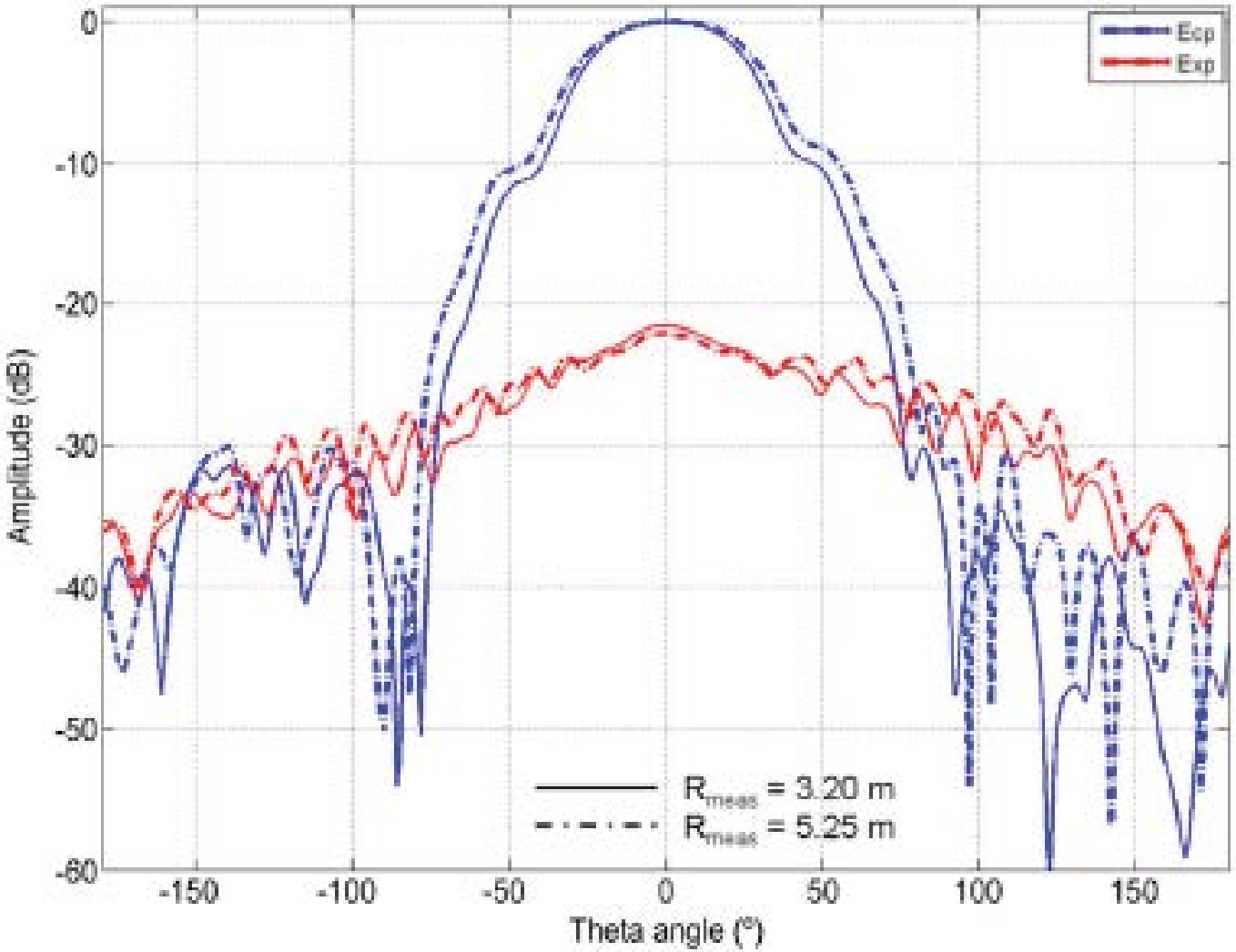

Fig. 11. Measured electric field (normalized amplitude, in decibels) at distances corresponding to $R_1 = 3.20$ m and $R_2 = 5.25$ m and plane $\varphi = 0°$. (a) $f = 1.03$ GHz. (b) $f = 2.50$ GHz. Blue line: field copolar component (E_y). Red line: field crosspolar component (E_x).

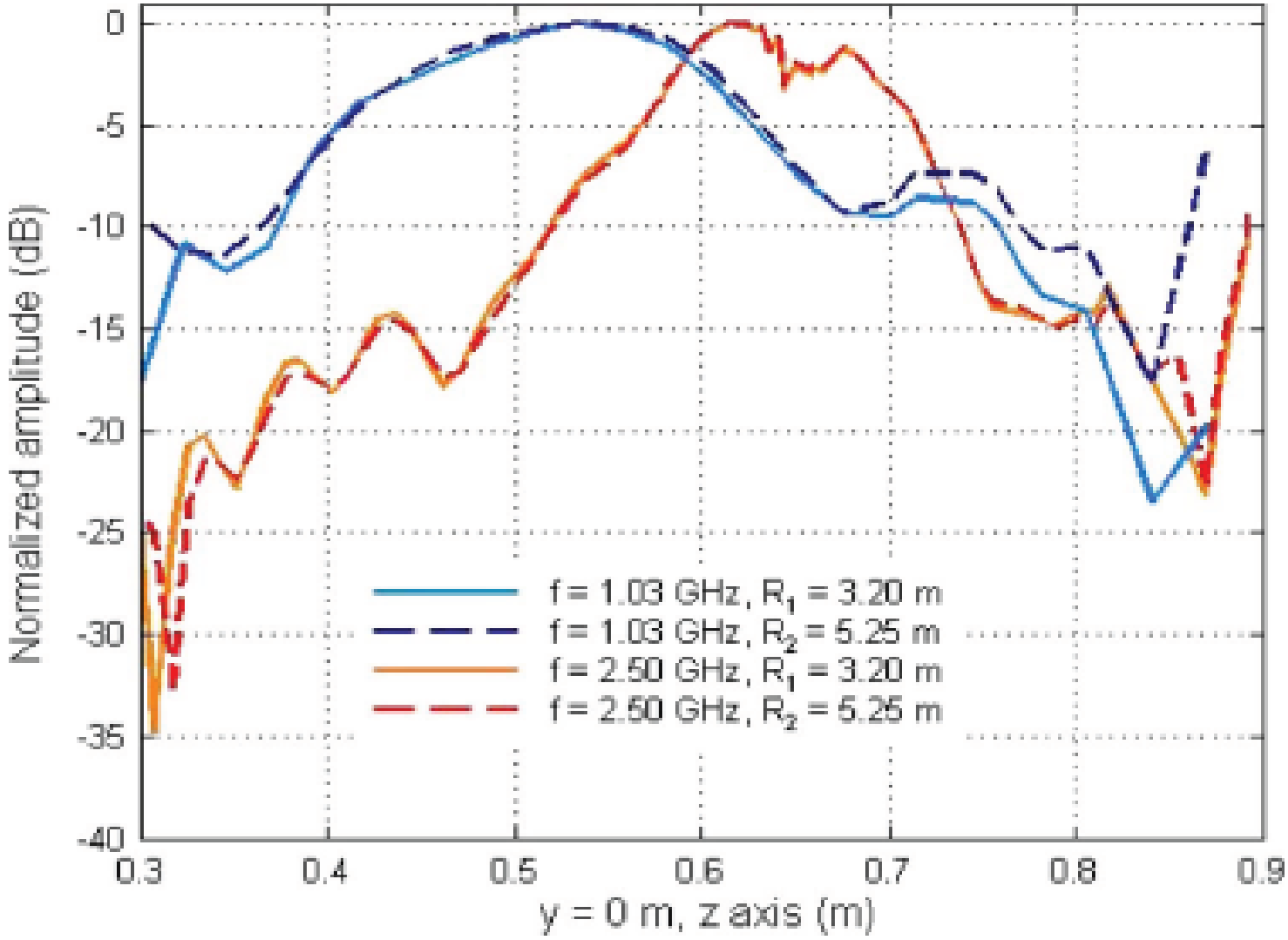

Fig. 15. Reconstructed equivalent currents. J_y component (normalized amplitude, in decibels) along the z-axis ($y = 0$ m).

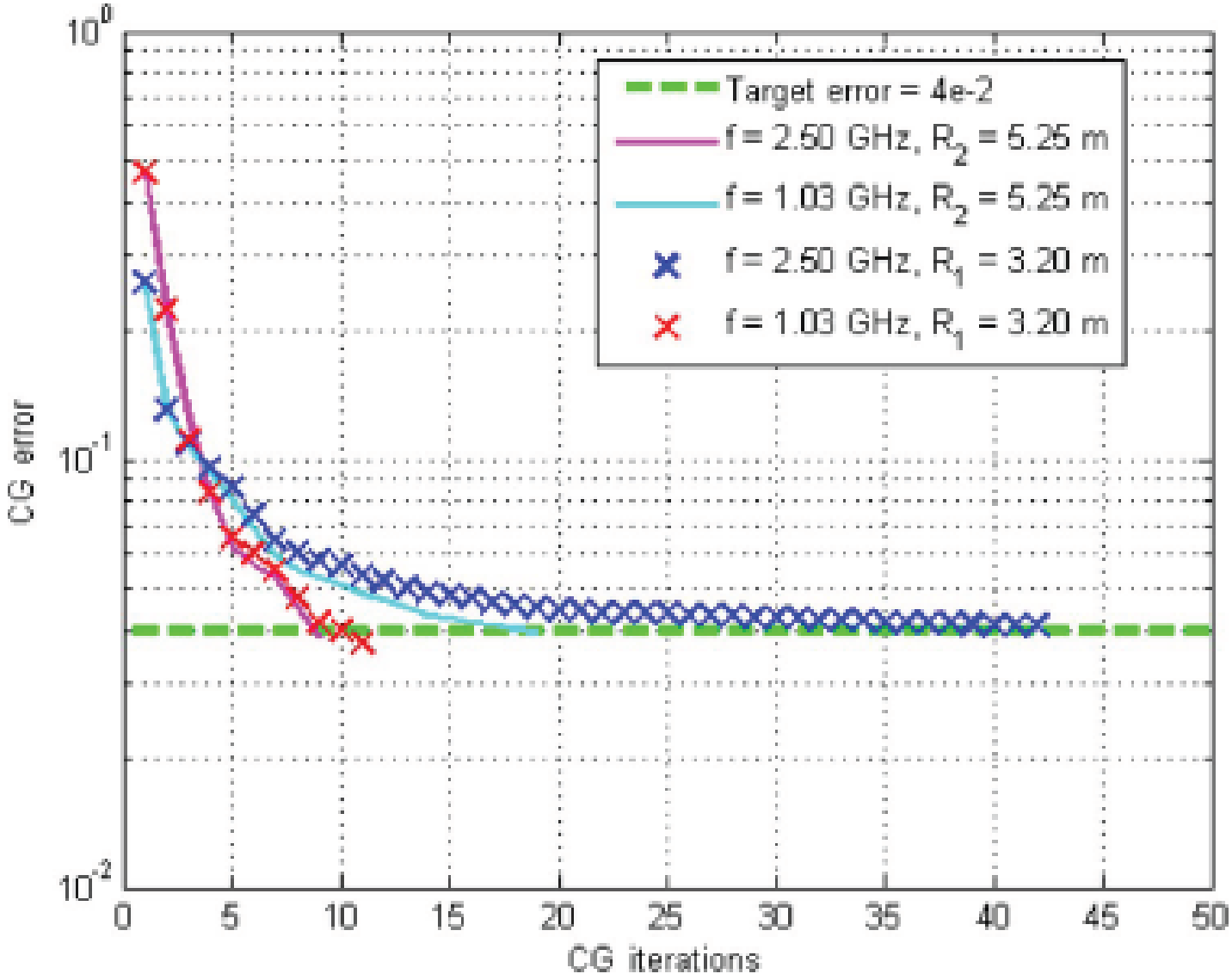

Fig. 12. Rate of convergence of the CG method for different problem configurations when using the RWG basis functions.

Example 1

SOURCE: Four y-directed dipoles placed at the corners of a $4\lambda \times 4\lambda$ planar surface

ASSUMED SOURCE: a $5\lambda \times 5\lambda$ planar magnetic current sheet containing M_x and M_y components divided into 25 × 25 current patches.

MEASUREMENT: Near fields sampled over the $5\lambda \times 5\lambda$ plane at a distance $3\ \lambda$ from the source.

Equivalent magnetic current patches are used to approximate the dipoles.

Modal expansion will be valid only over

$\tan^{-1}([2.5\text{-}2.0]/3) = \pm 10^{o}$

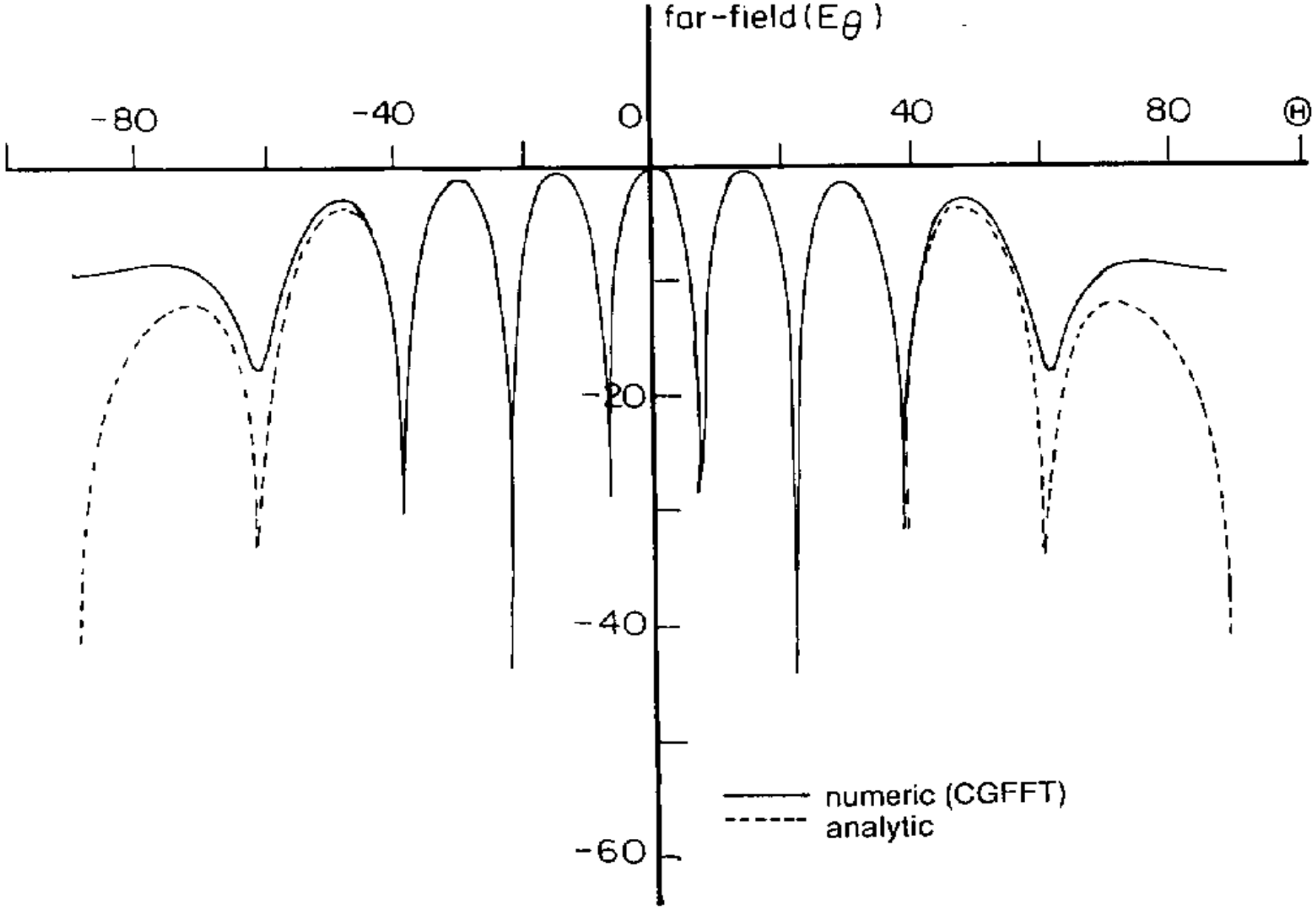

Fig. 3. Comparison of exact and computed far fields for $\Phi = 90$ cut for 2×2 electric dipoles on a $4\lambda \times 4\lambda$ surface using planar scanning.

Fig. 4. (a) Comparison of exact and computed far fields for $\Phi = 90$ cut for 2×2 magnetic dipoles on a $4\lambda \times 4\lambda$ surface using planar scanning and equivalent magnetic current approach; (b) comparison of exact and computed far fields for $\Phi = 90$ cut for 2×2 magnetic dipoles on a $4\lambda \times 4\lambda$ surface using planar scanning and equivalent magnetic array approximation.

Here 20 × 20 dipole array are used to approximate the current source

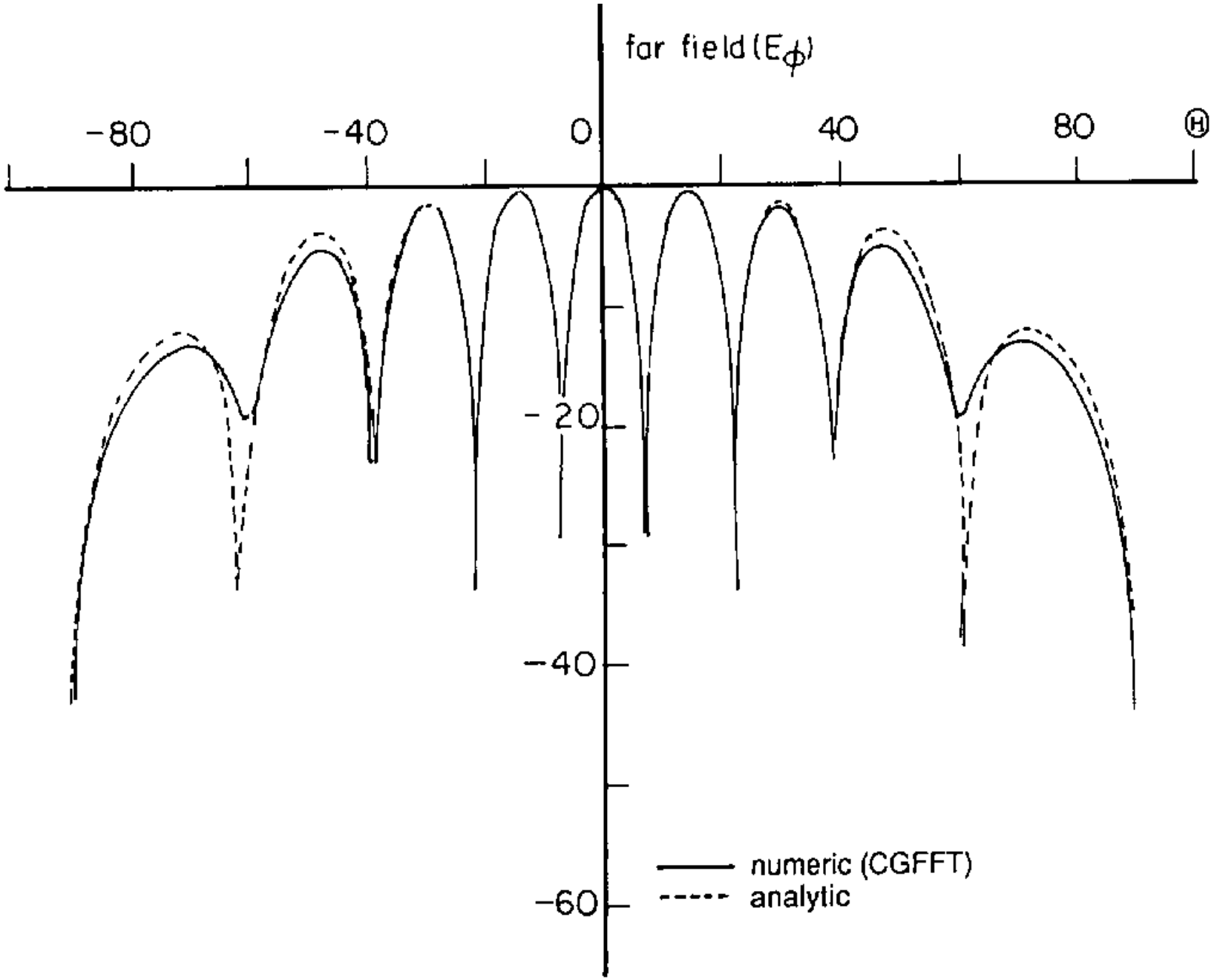

(a)

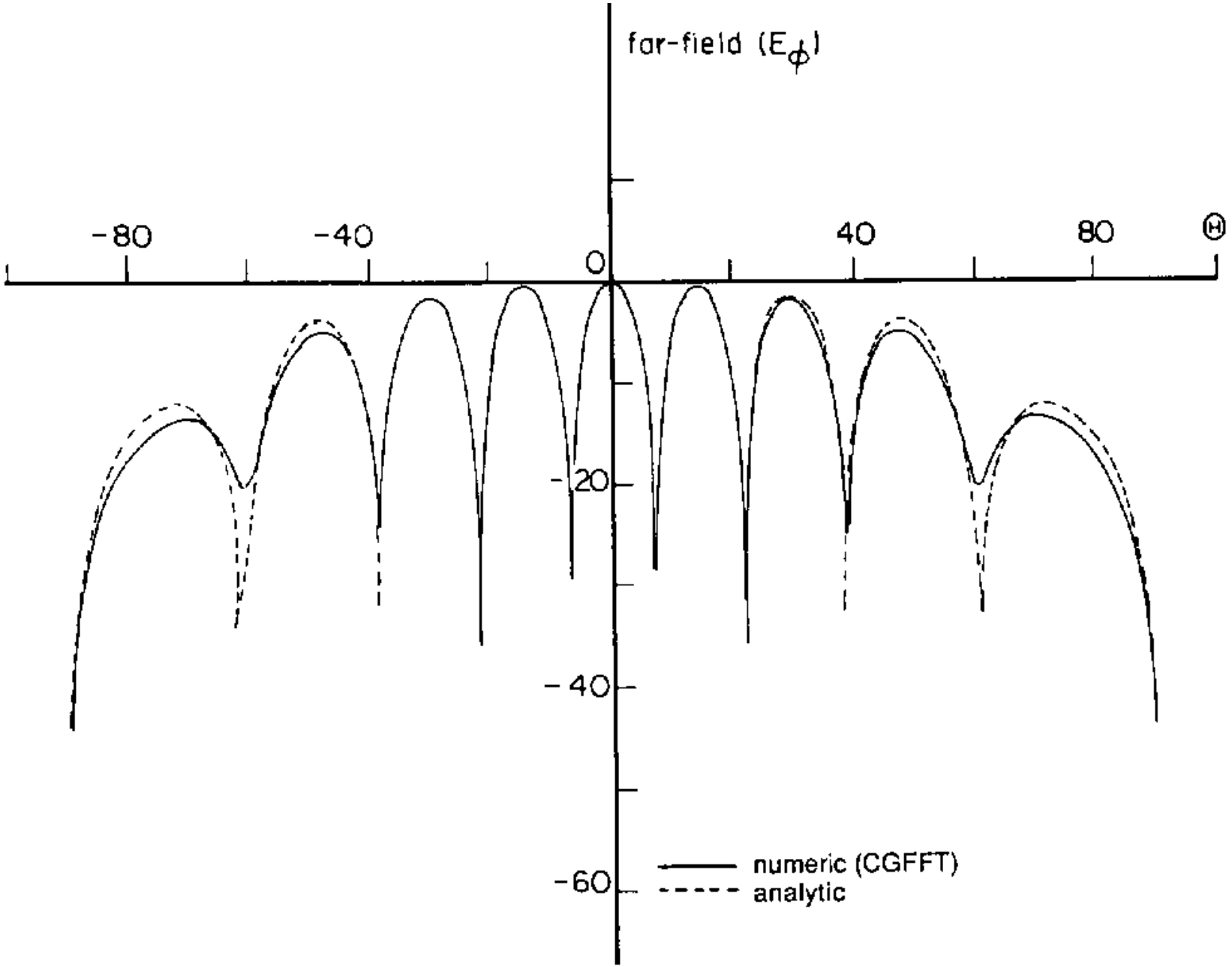

(b)

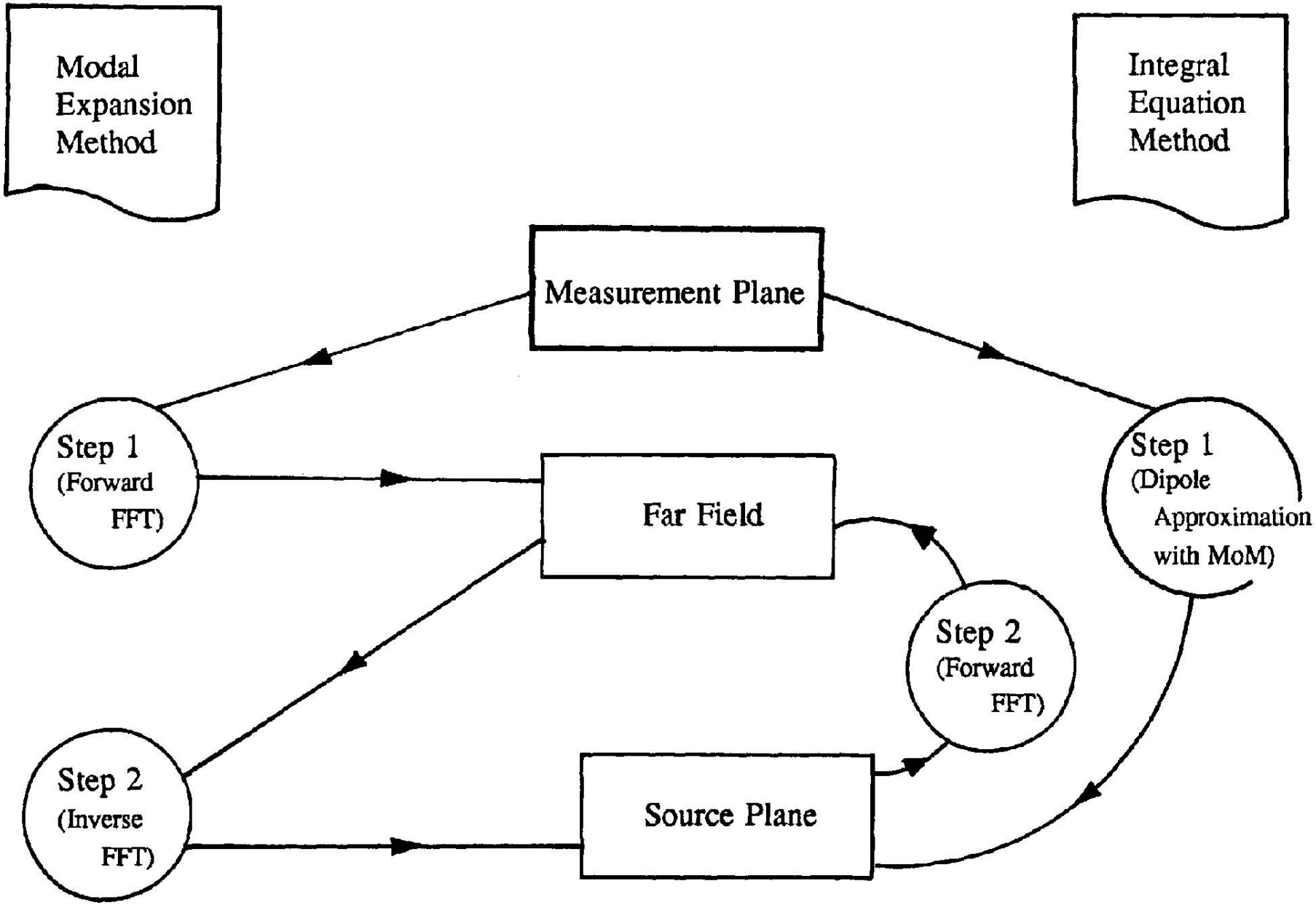

DIFFERENCE IN PROCESSING BETWEEN THE MODAL EXPANSION METHOD AND THE INTEGRAL EQUATION APPROACH

Example 3: Using Measured Data

- 32 × 32 microstrip patch array uniformly distributed over a 1.5m × 1.5m surface. The operating frequency is 3.3 GHz. The array is considered to be in the *x-y* plane. The near field is measured on a 3.24m × 3.24m surface at a distance of 35cm from the array. There are 81 × 81 measured points 4cm apart using a WR 284 waveguide.

EQUIVALENT SOURCE: 39 × 39 magnetic dipole approximation for the source on a 1.56m × 1.56m surface.

MEASUREMENT PLANE: near field is measured at 81 × 81 points on a 3.24m × 3.24m surface at a distance of 35cm from the array.

CONVENTIONAL MODAL EXPANSION will provide good results upto $\tan^{-1}(87/35) = \pm 68^{o}$

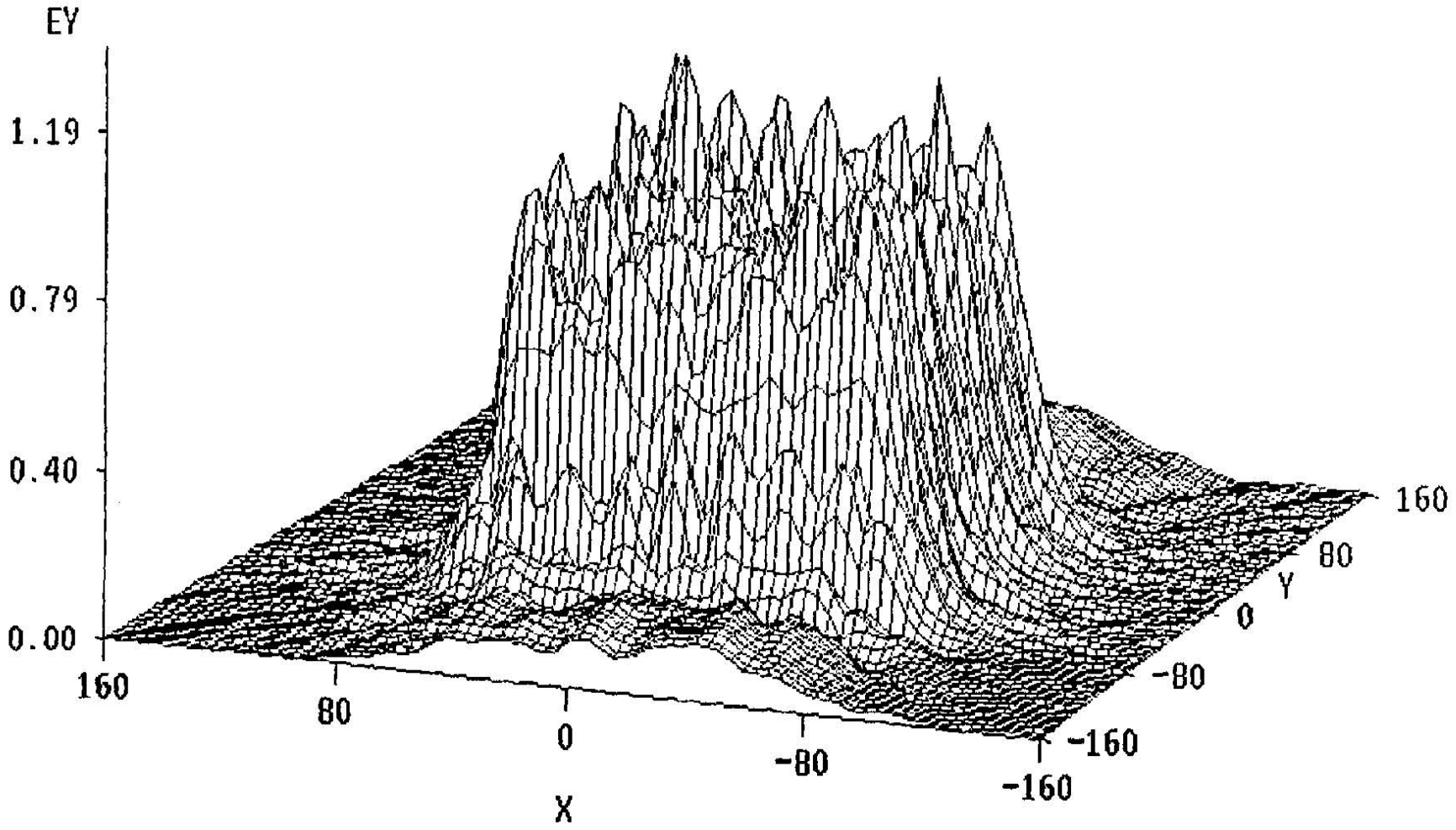
EY
1.19
0.79
0.40
0.00
160
80
0
-80
-160
X
160
80
0
-80
-160
Y

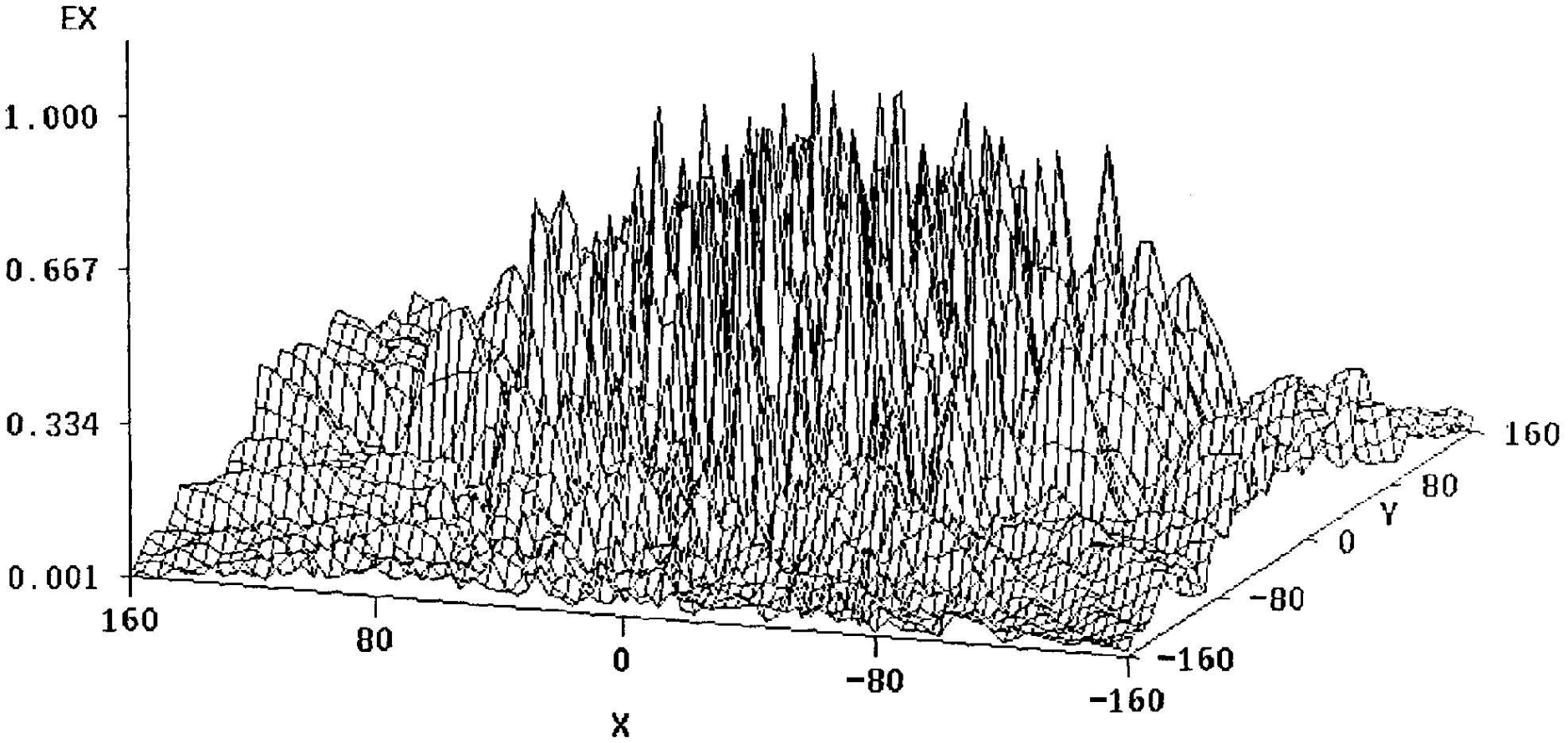
EX
1.000
0.667
0.334
0.001
160
80
0
-80
-160
X
160
80
0
-80
-160
Y

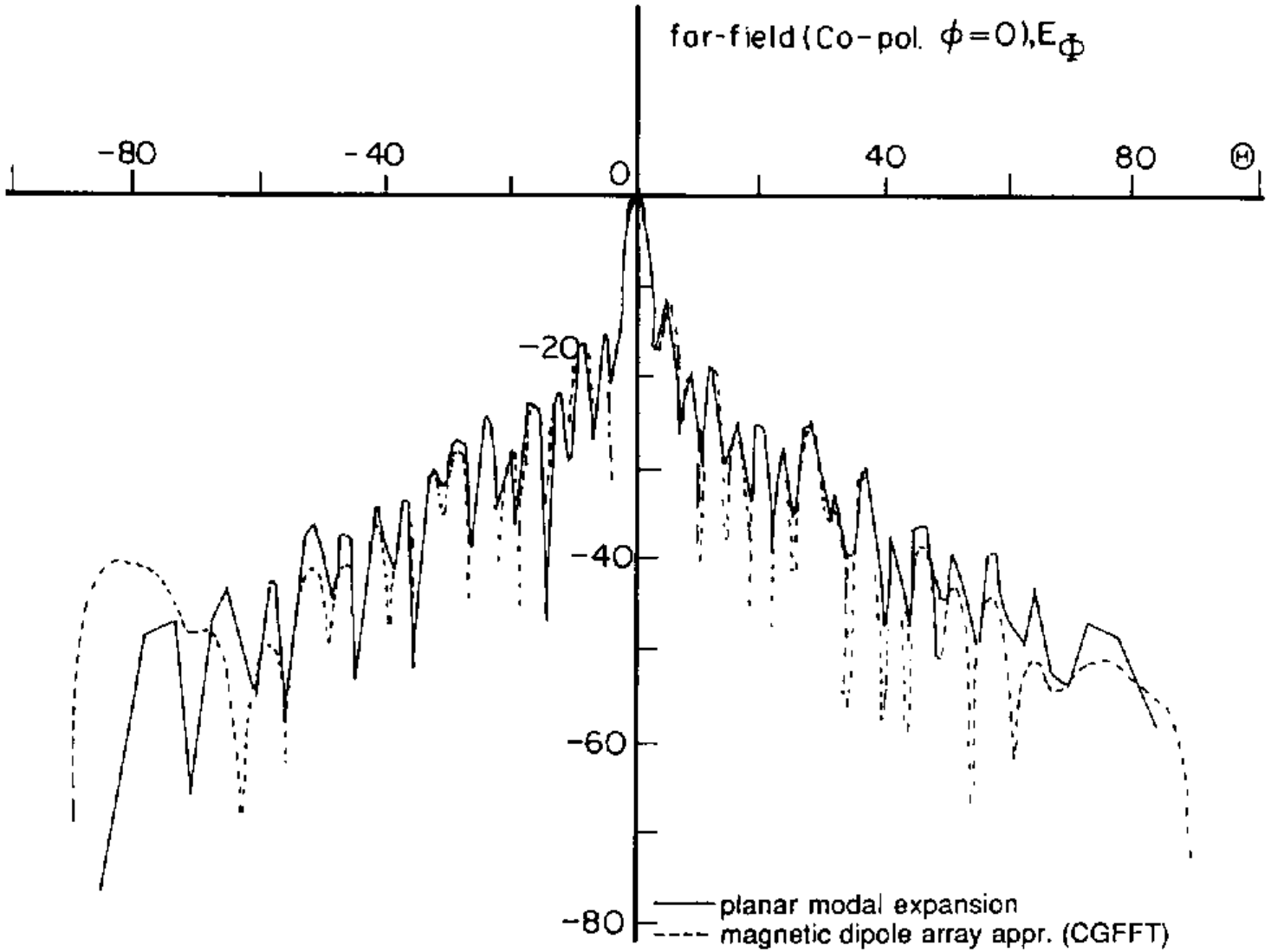

Fig. 5. Copolarization characteristic for $\Phi = 0$ cut for a 32×32 patch microstrip array using planar modal expansion and equivalent magnetic dipole array approximation.

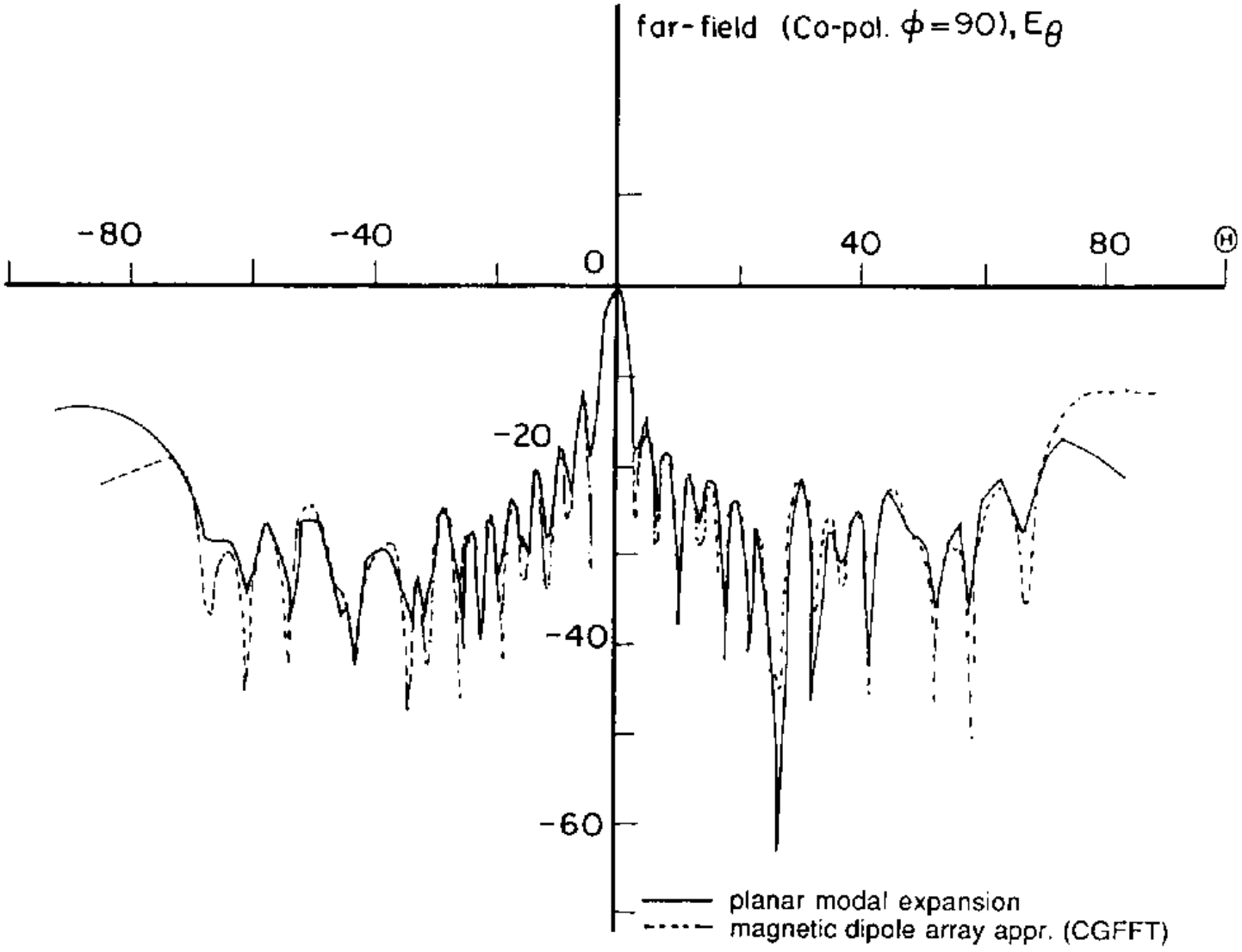

Fig. 6. Copolarization characteristic for $\Phi = 90$ cut for a 32×32 patch microstrip array using planar modal expansion and equivalent magnetic dipole array approximation.

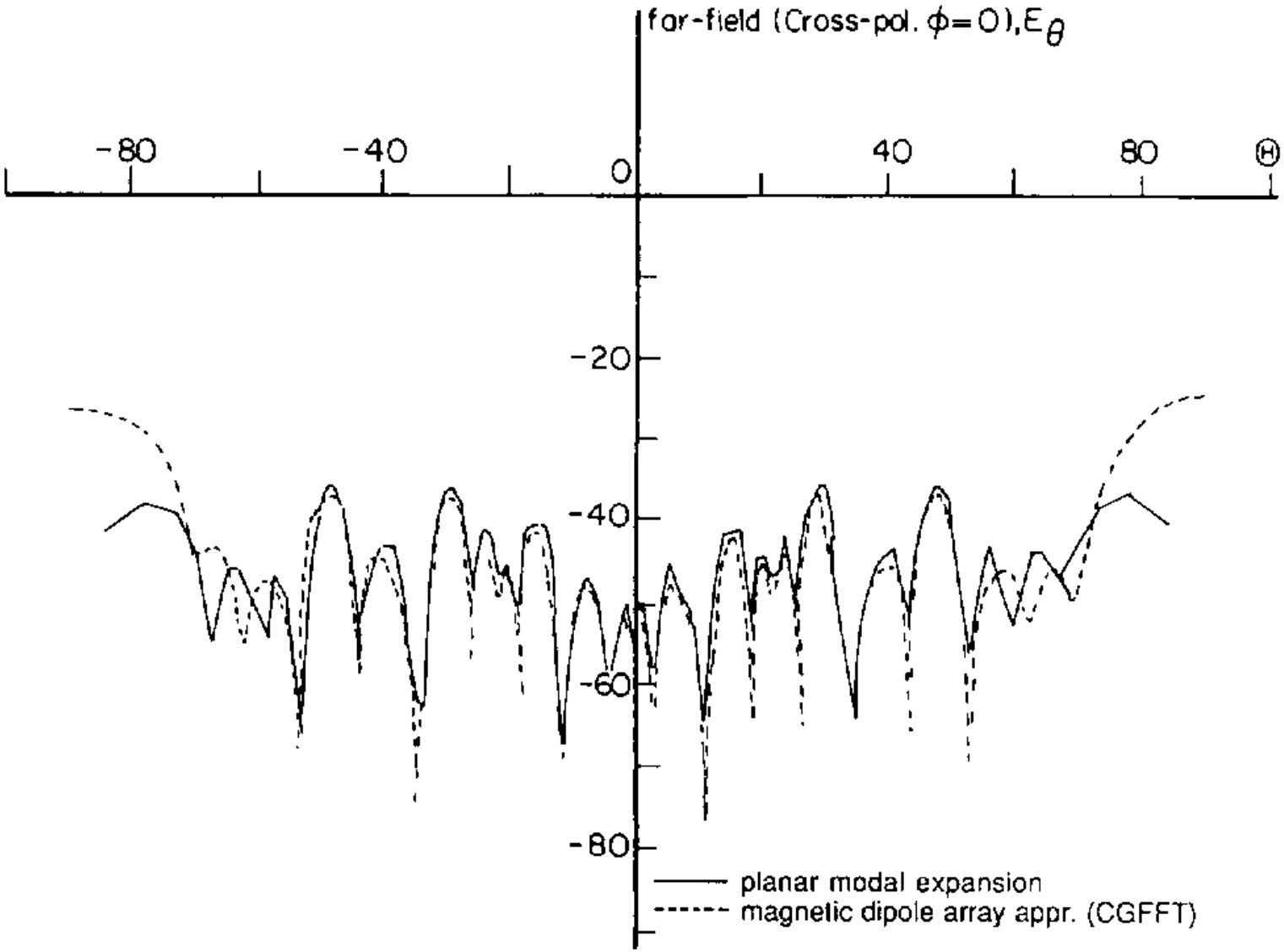

Fig. 7. Cross-polarization characteristic for $\Phi = 0$ cut for a 32×32 patch microstrip array using planar modal expansion and equivalent magnetic dipole array approximation.

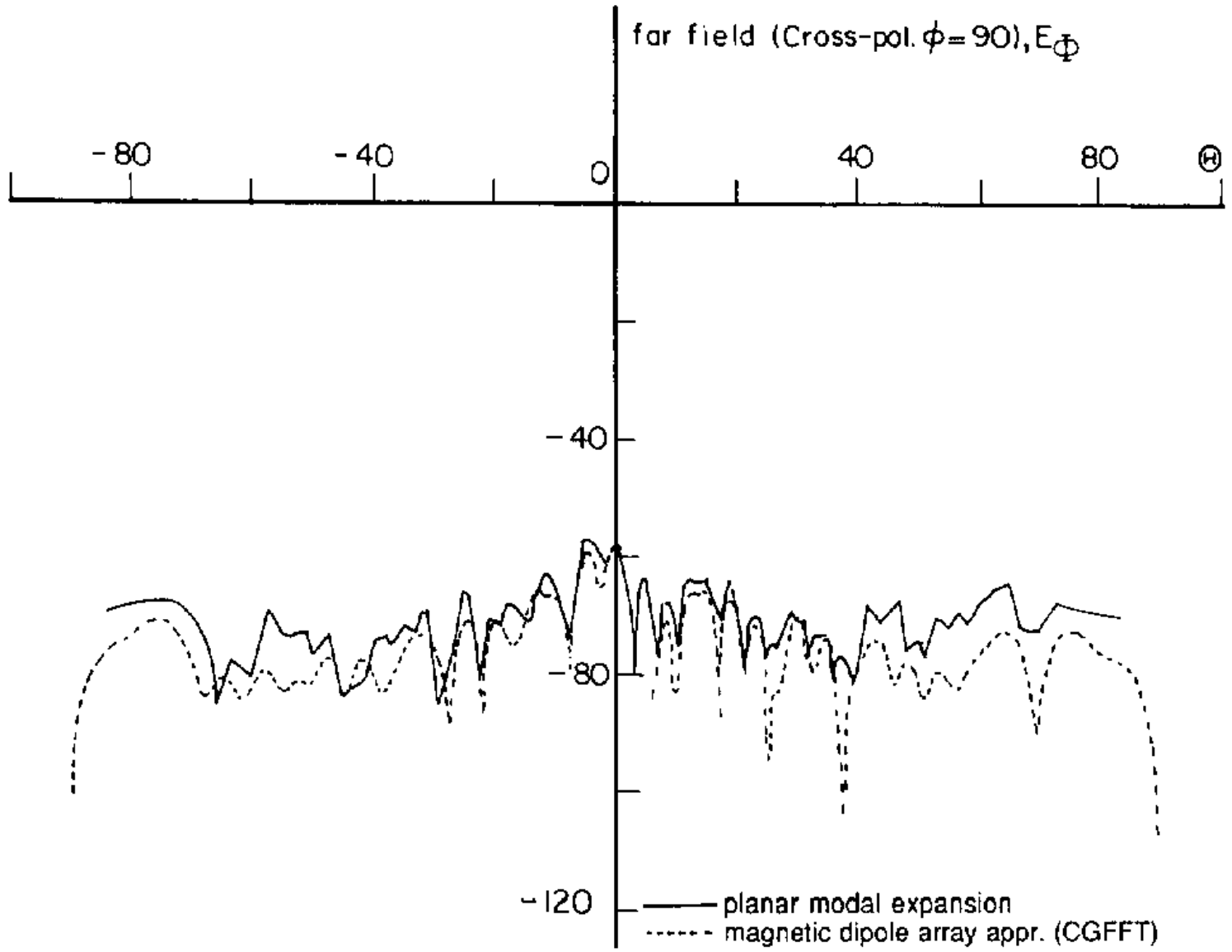

Fig. 8. Cross-polarization characteristic for $\Phi = 90$ cut for a 32×32 patch microstrip array using planar modal expansion and equivalent magnetic dipole array approximation.

Example 4: Using Measured Data

EQUIVALENT SOURCE: 37 × 37 magnetic dipole approximation for the source on a 1.48m × 1.48m surface.

MEASUREMENT PLANE: near field is measured at 37 × 37 points on a 1.48m × 1.48m surface at a distance of 35cm from the array.

CONVENTIONAL MODAL EXPANSION will not work! This approach is still valid to ±35º

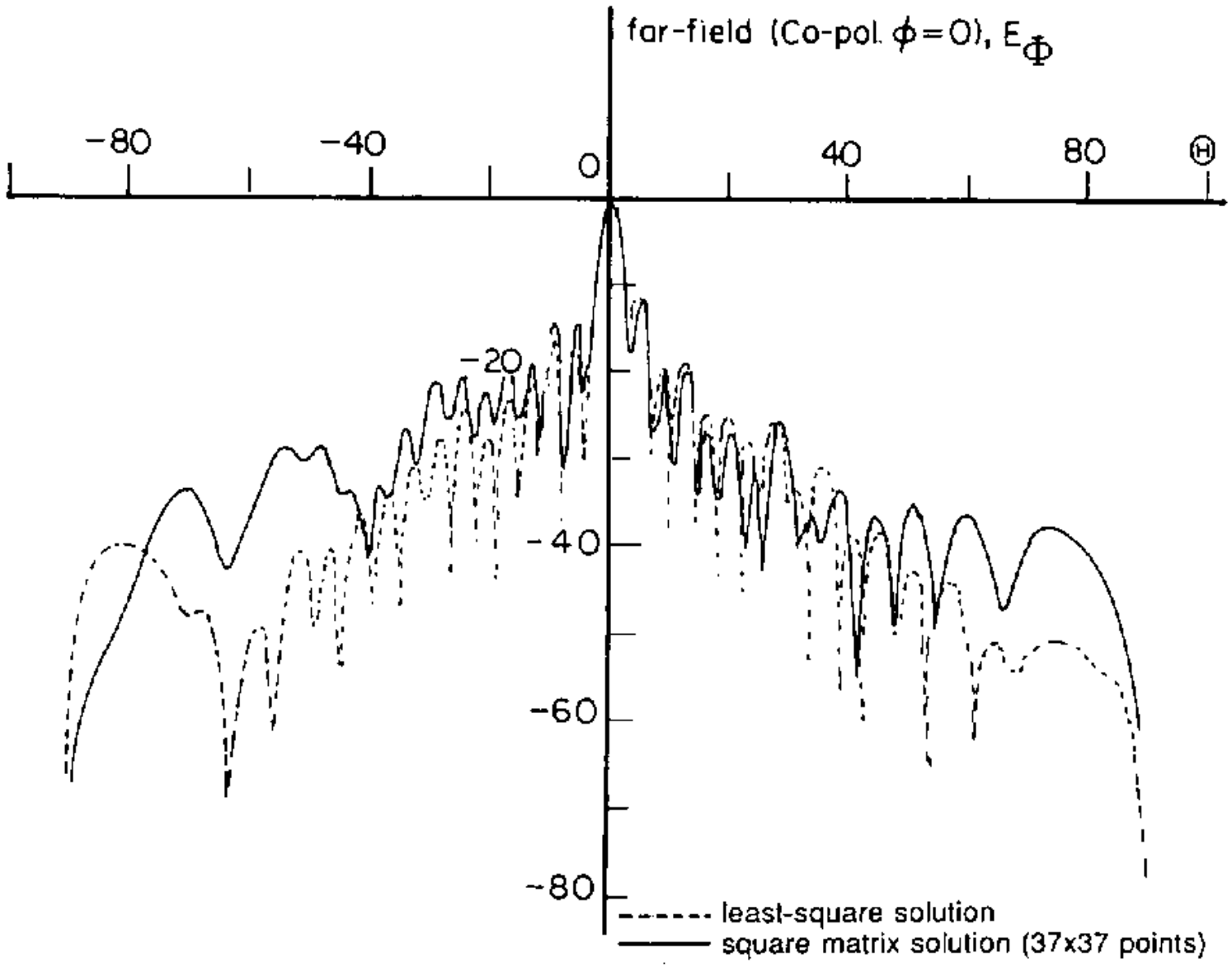

Fig. 9. Copolarization characteristic for $\Phi = 0$ cut for a 32×32 patch microstrip array using least-squares and square matrix solutions.

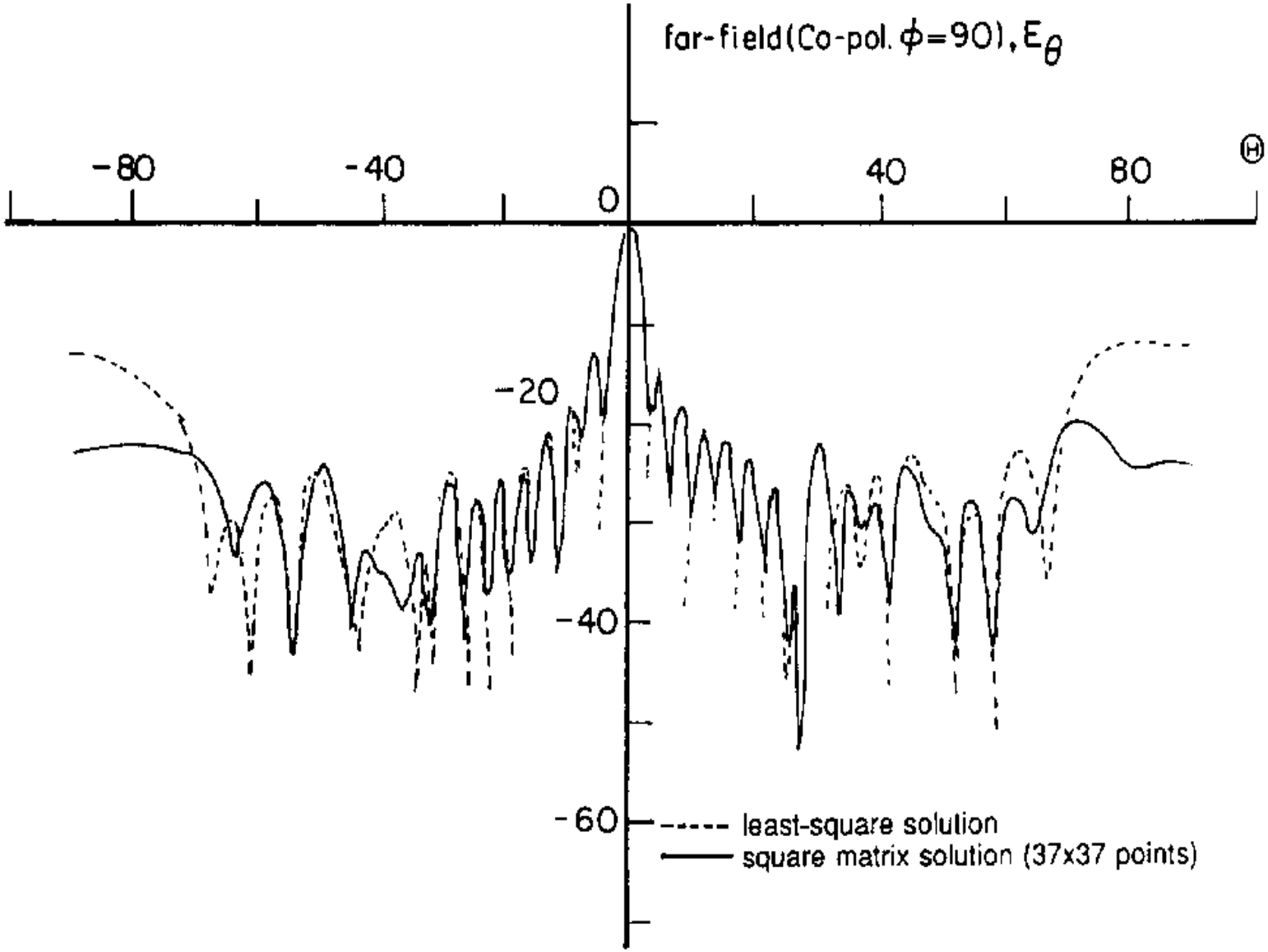

Fig. 10. Copolarization characteristic for $\Phi = 90$ cut for a 32×32 patch microstrip array using least-squares and square matrix solutions.

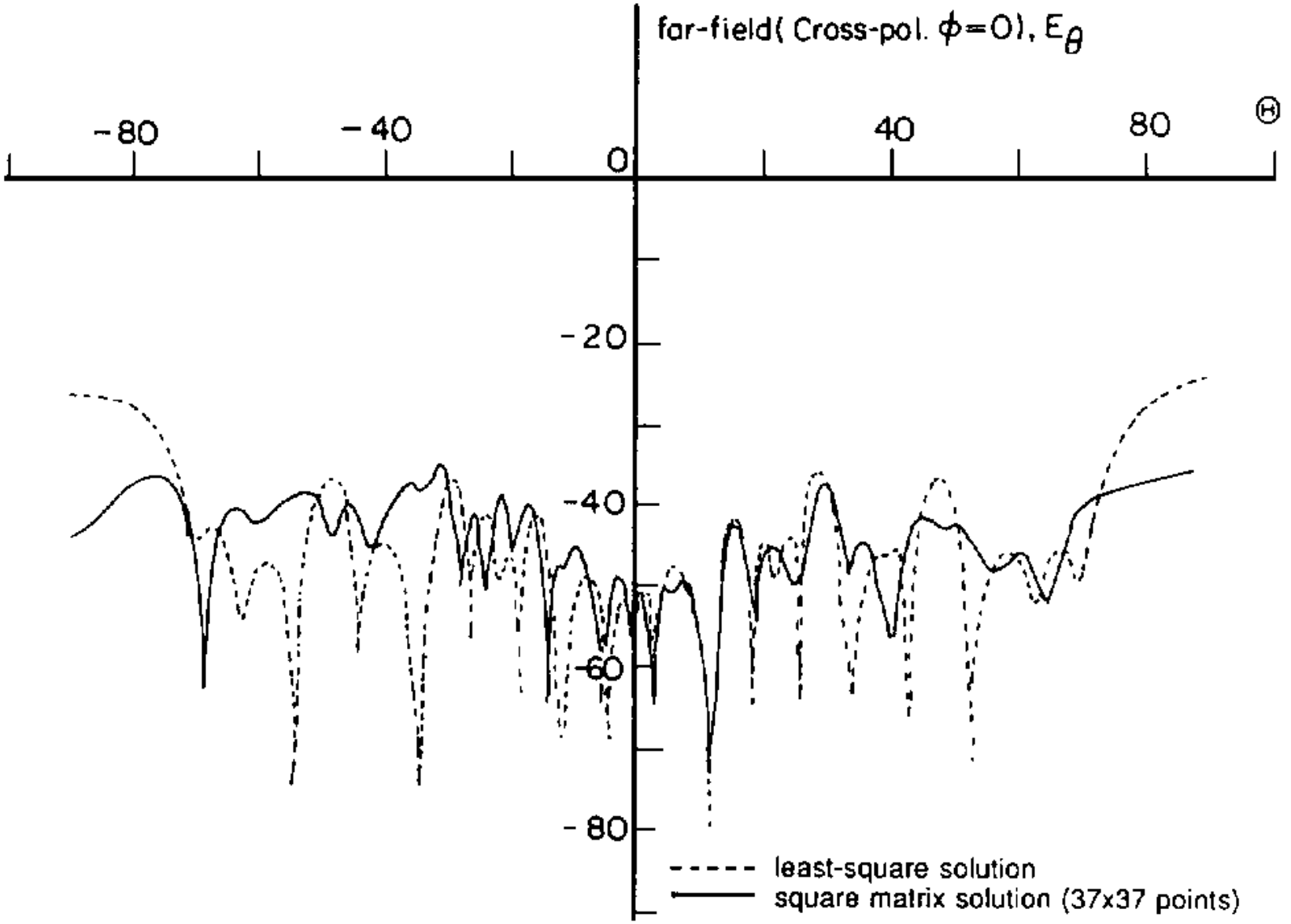

Fig. 11. Cross-polarization characteristic for $\Phi = 0$ cut for a 32×32 patch microstrip array using least-squares and square matrix solutions.

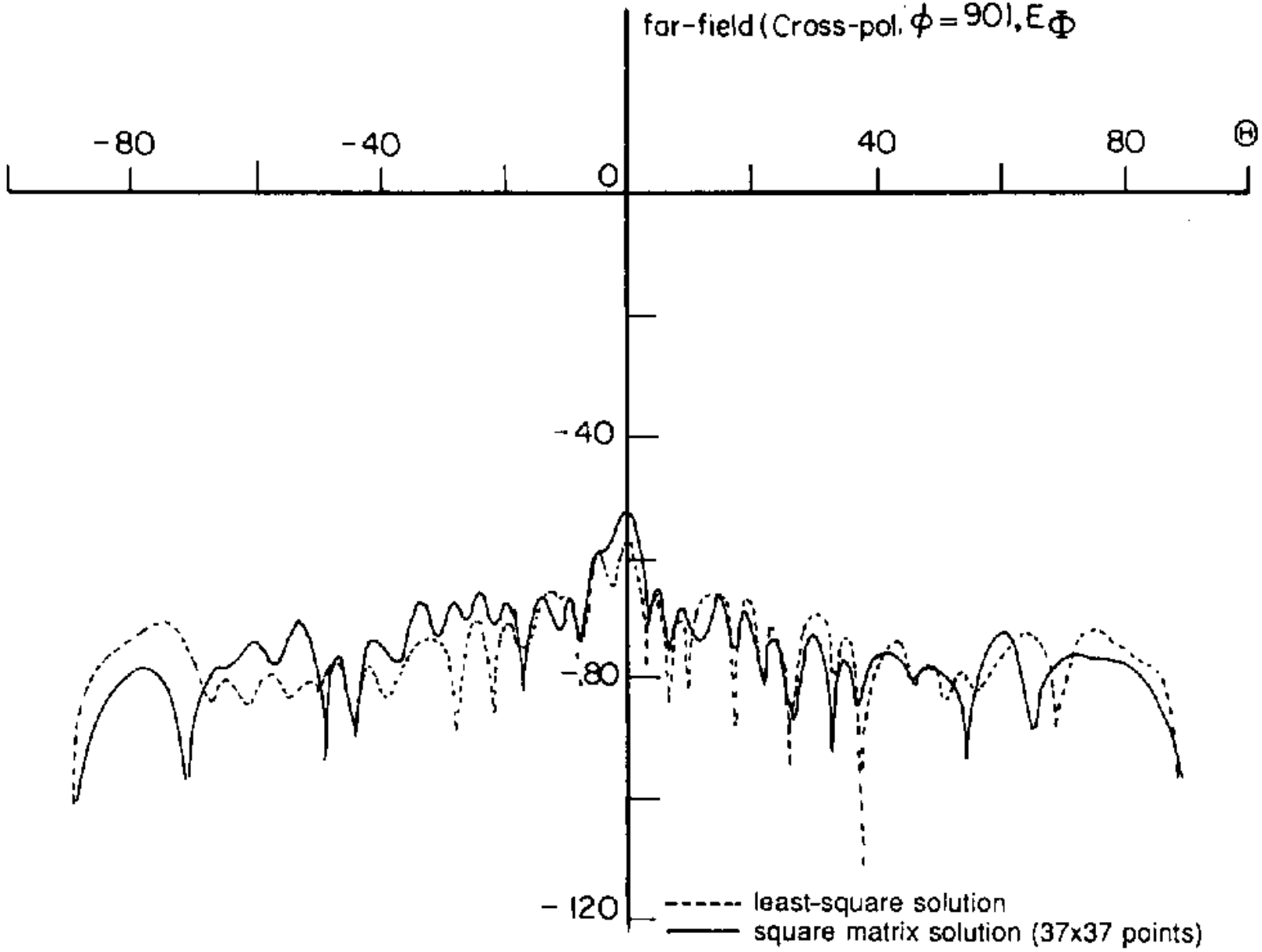

Fig. 12. Cross-polarization characteristic for $\Phi = 90$ cut for a 32×32 patch microstrip array using least-squares and square matrix solutions.

Example 5: Using Measured Data

EQUIVALENT SOURCE: 39 × 39 magnetic dipole approximation for the source on a 1.56m × 1.56m surface.

MEASUREMENT PLANE: near field is measured over a narrow strip at 81 × 19 points on a 3.24m × 0.76m surface at a distance of 35cm from the array.

CONVENTIONAL MODAL EXPANSION will not work!

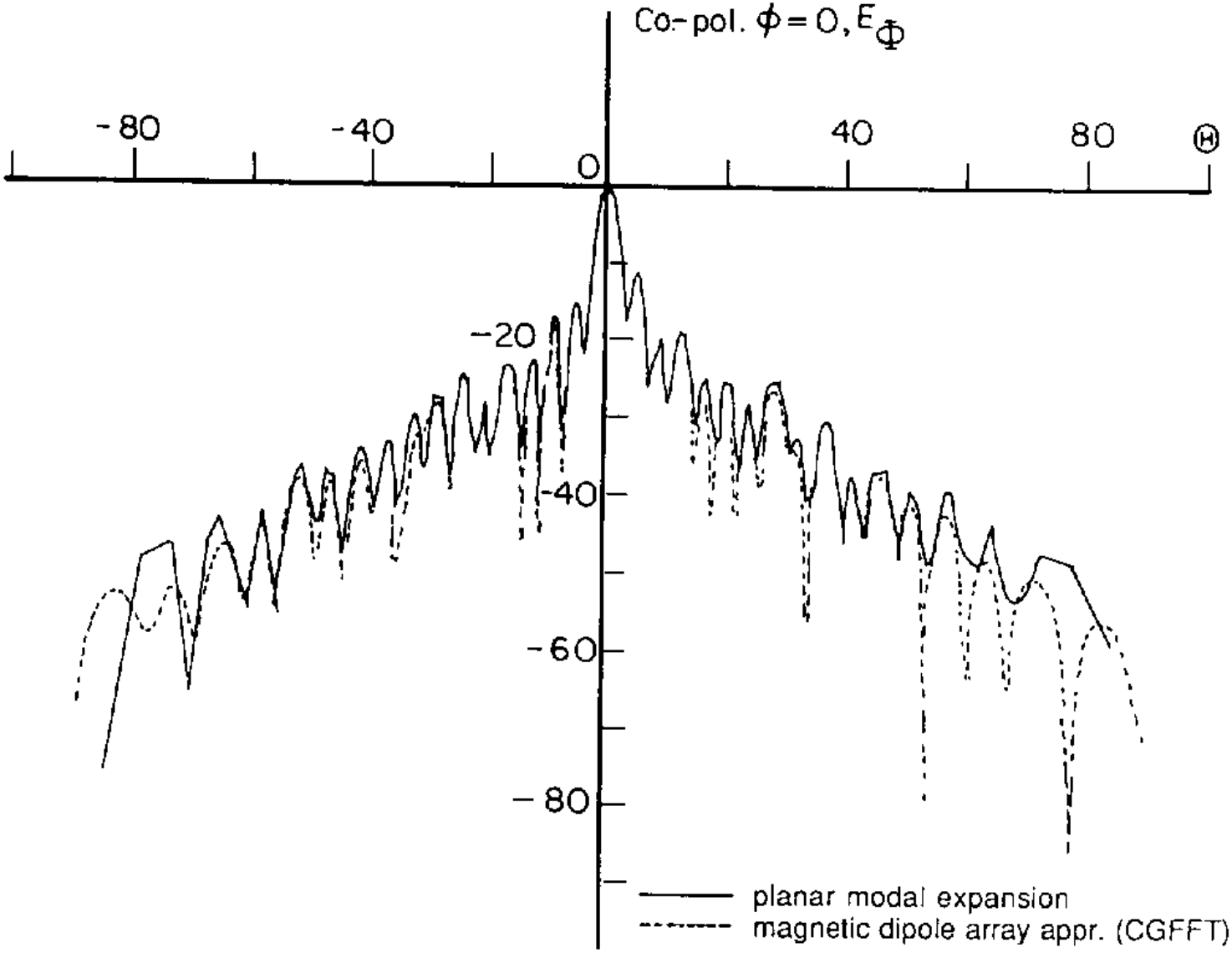

Fig. 13. Copolarization characteristic for $\phi = 0$ cut for the microstrip array when the near-field is measured in a narrow region (3.24 × 0.76 m) as opposed to (3.24 × 3.24 m).

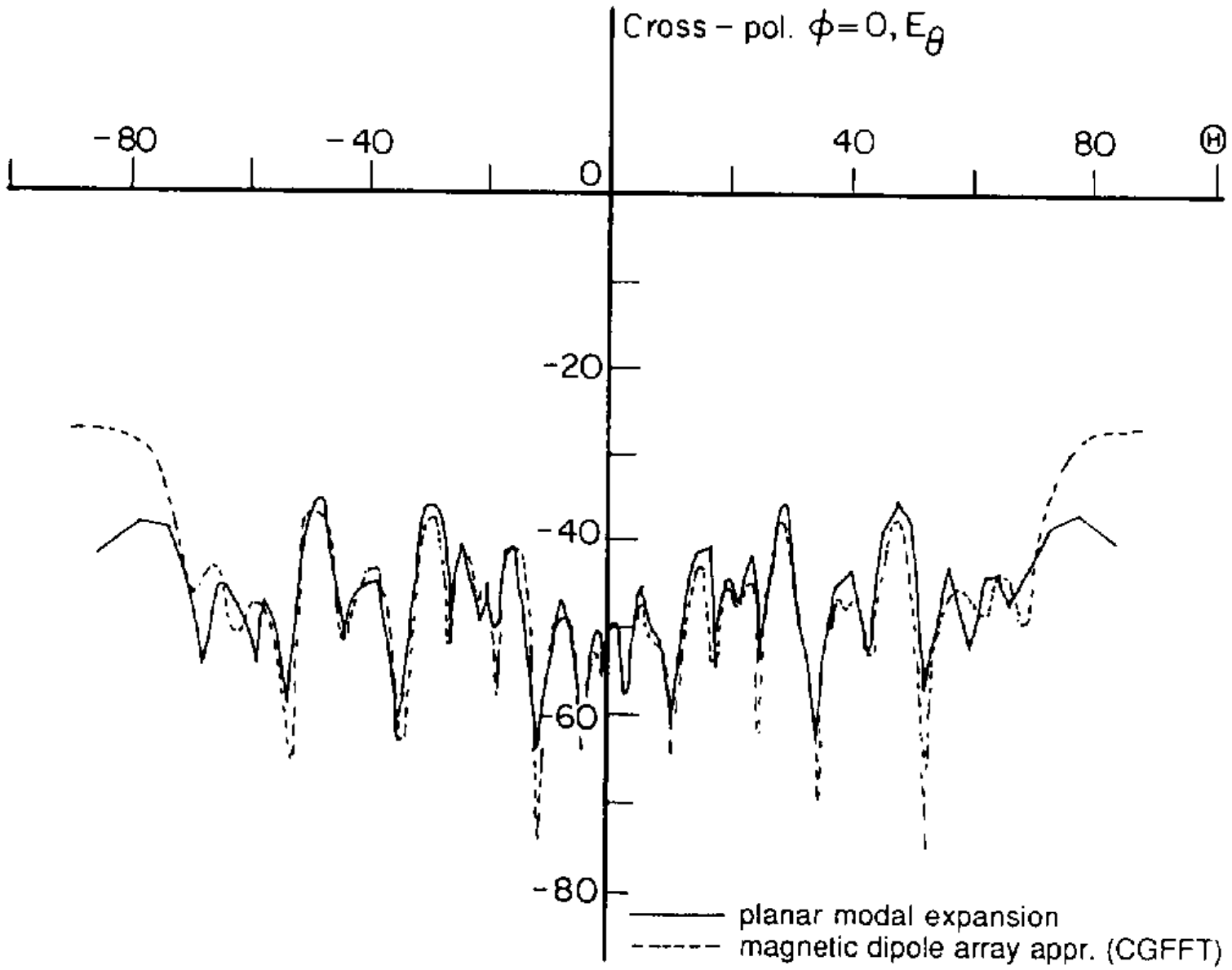

Fig. 14. Cross-polarization characteristic for $\phi = 0°$ for the microstrip array with data measured on a narrow region (3.24 × 0.76 m).

Example 6: Using Measured Data

EQUIVALENT SOURCE: 39 × 39 magnetic dipole approximation for the source on a 1.56m × 1.56m surface.

MEASUREMENT PLANE: near field is measured over a narrow strip at 19 × 81 points on a 0.76m × 3.24m surface at a distance of 35cm from the array.

CONVENTIONAL MODAL EXPANSION will not work!

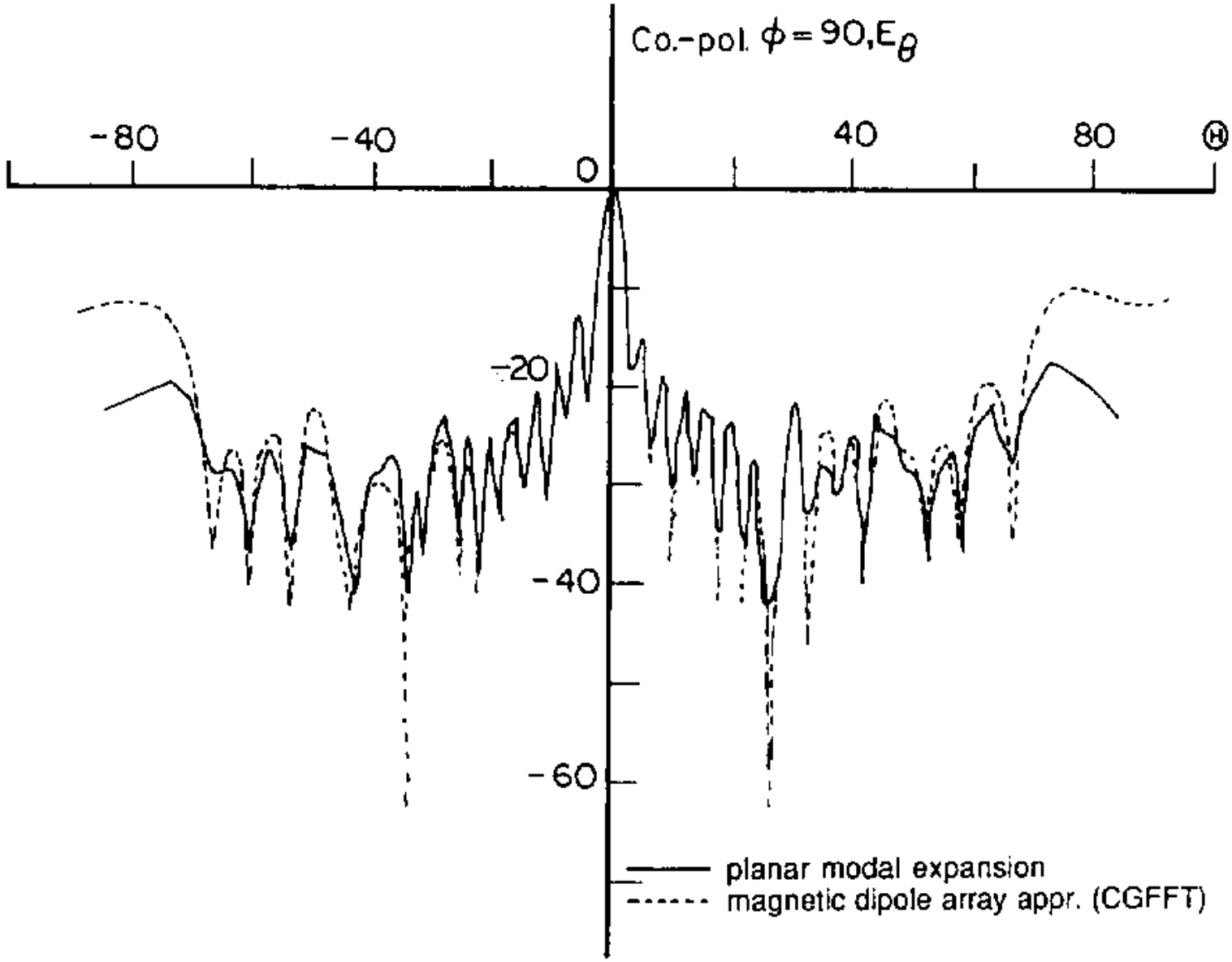

Fig. 15. Copolarization characteristic for $\phi = 90°$ cut for the microstrip array with data measured on a narrow region (0.76 × 3.24 m).

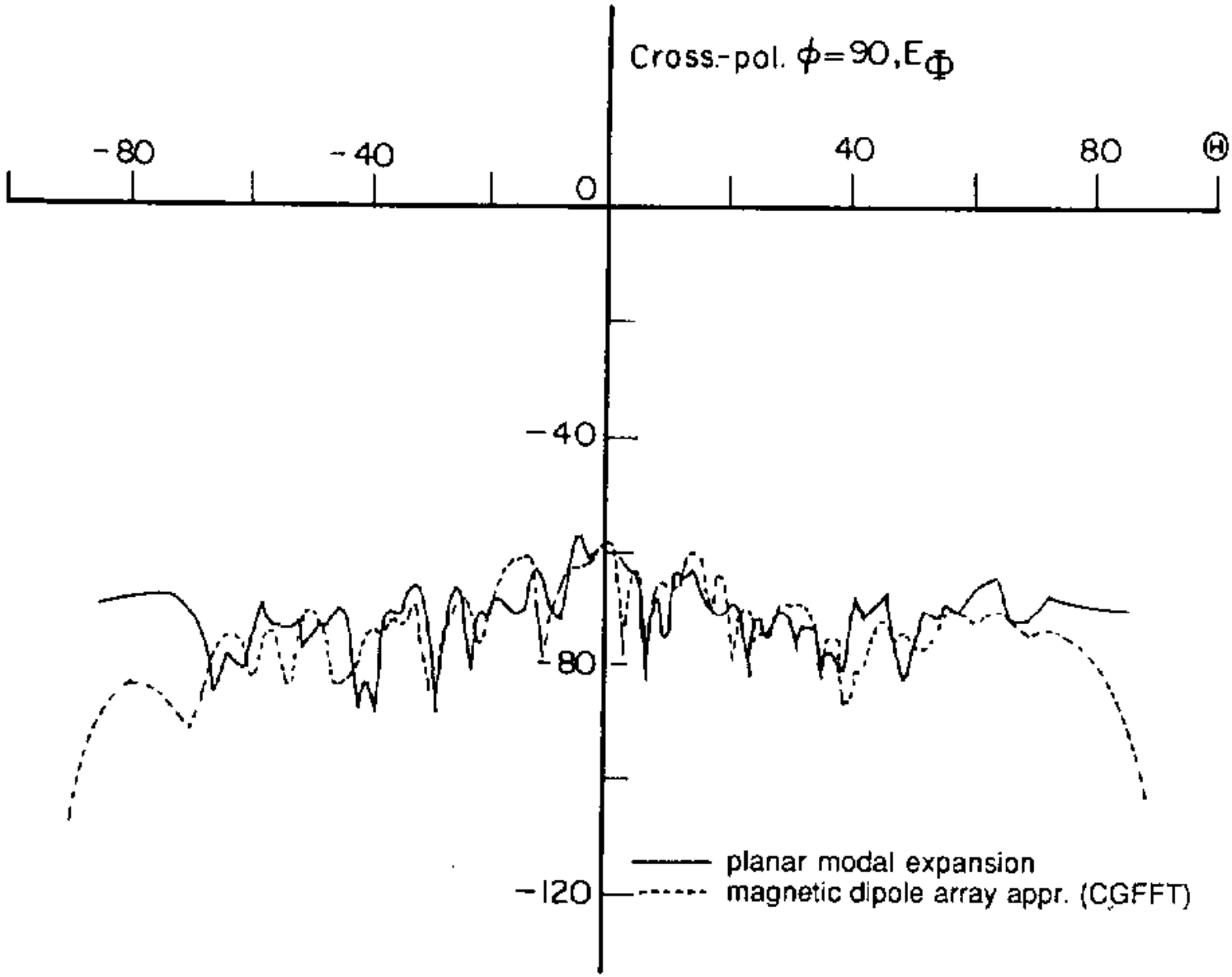

Fig. 16. Cross-polarization characteristic for $\phi = 90°$ cut for the microstrip array with data measured on a narrow region (0.76 × 3.24 m).

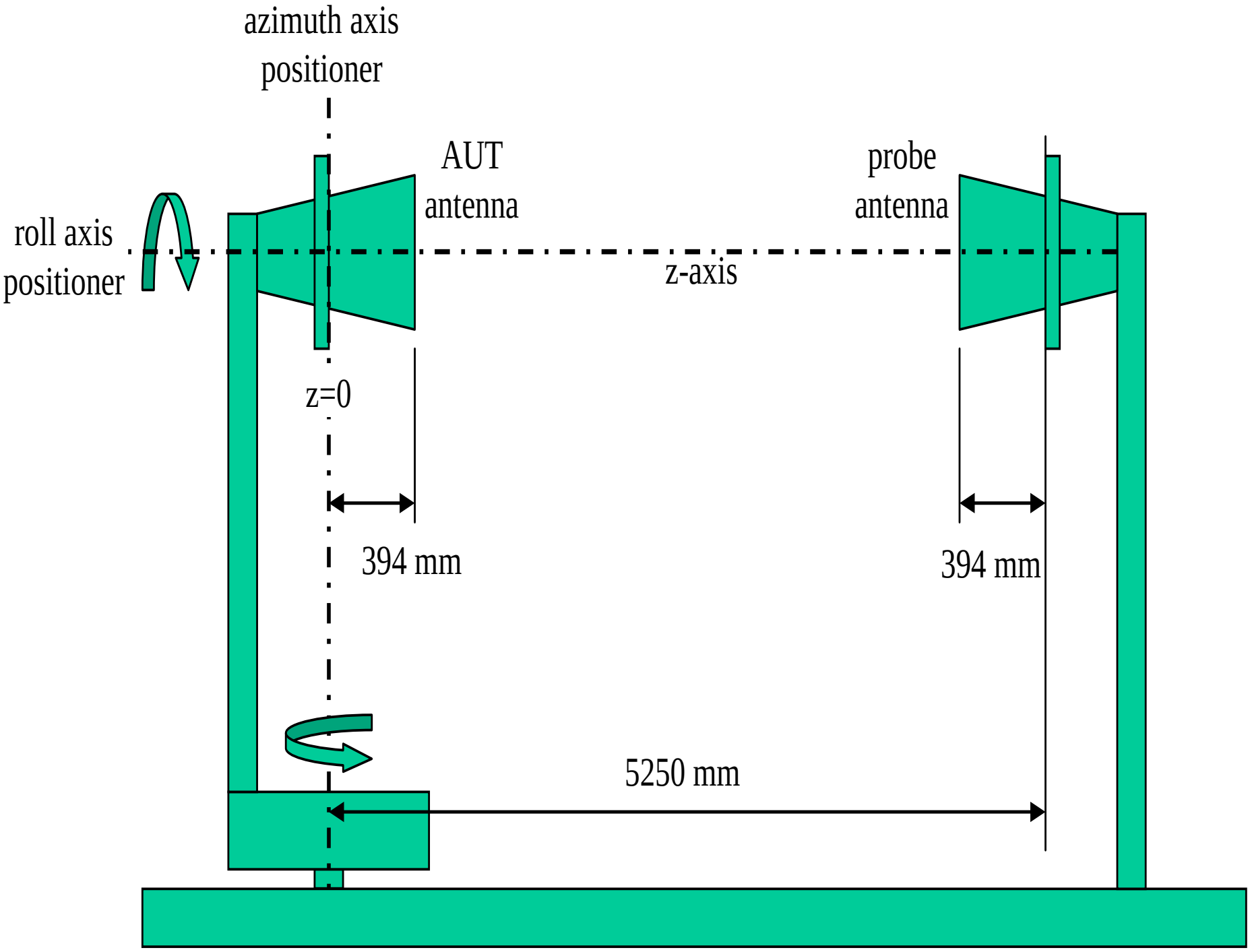
azimuth axis
positioner
AUT
antenna
probe
antenna
roll axis
positioner
z-axis
z=0
394 mm
394 mm
5250 mm

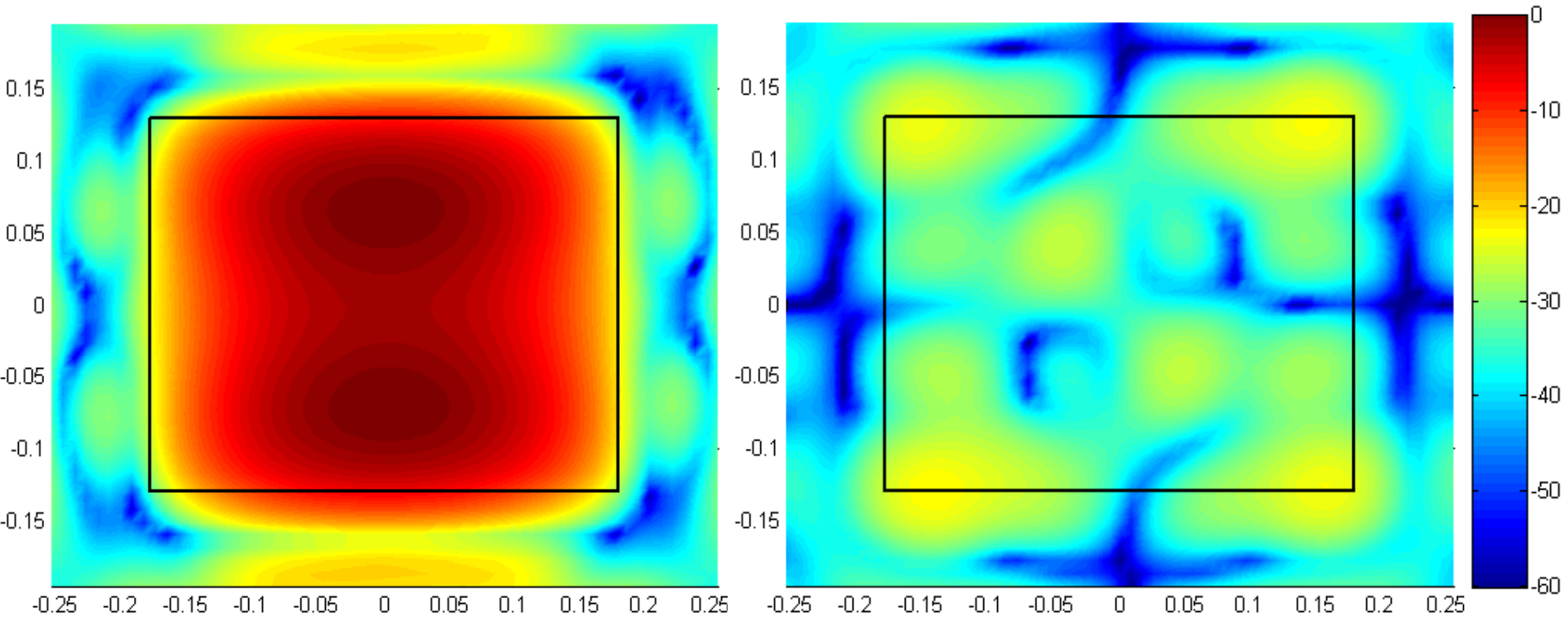

F=2.5 GHz; Planes located at z1 = 0.394 m, and z2 = 0 m ;
A planar domain of size 520 mm × 400 mm
(antenna: 348.6 mm × 259.6 mm)
EqMC consisted of 57 × 57 Hertzian dipoles separated 0.2 λ as basis functions

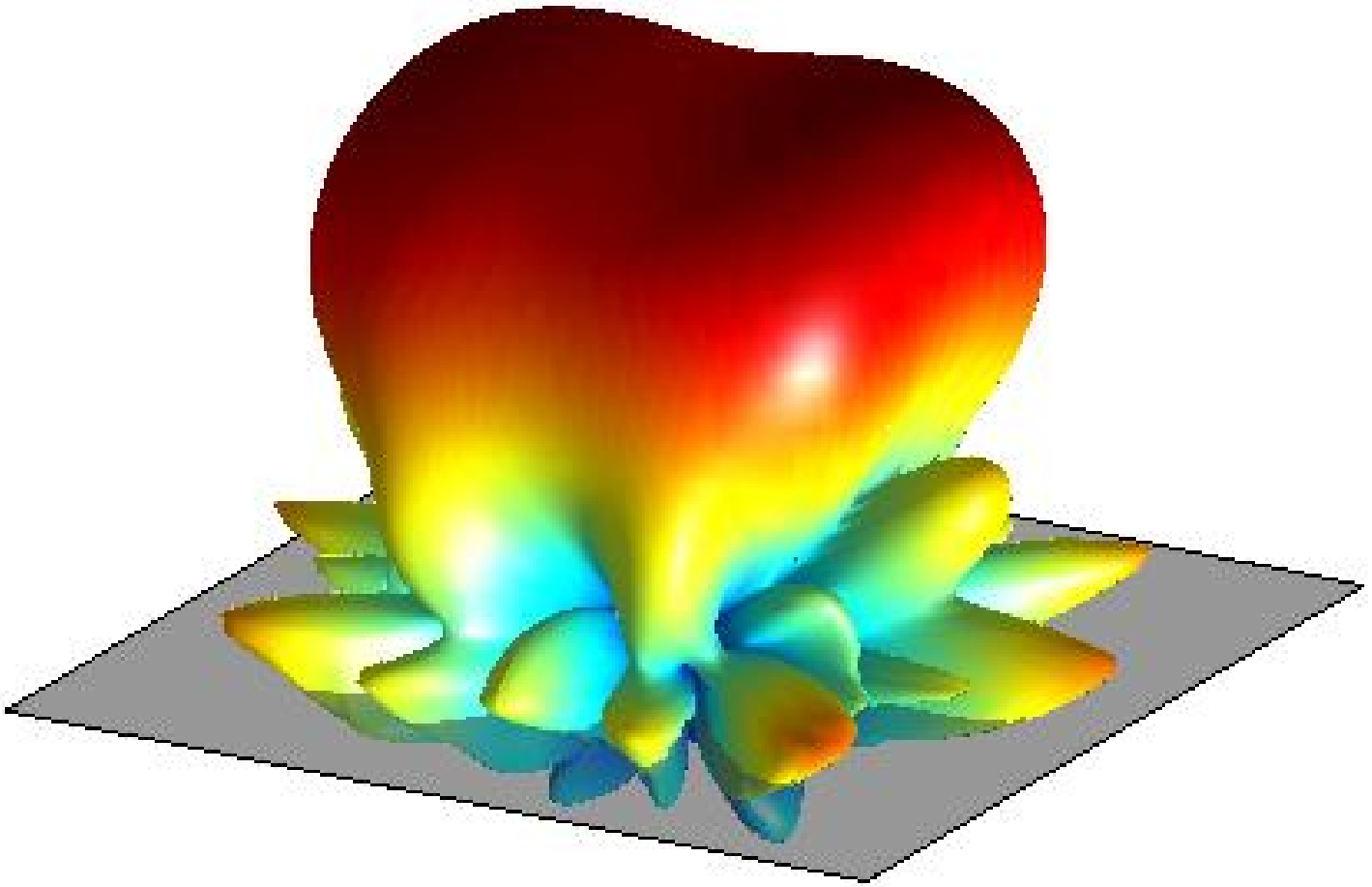

Polar plot of the fields at 20 cm

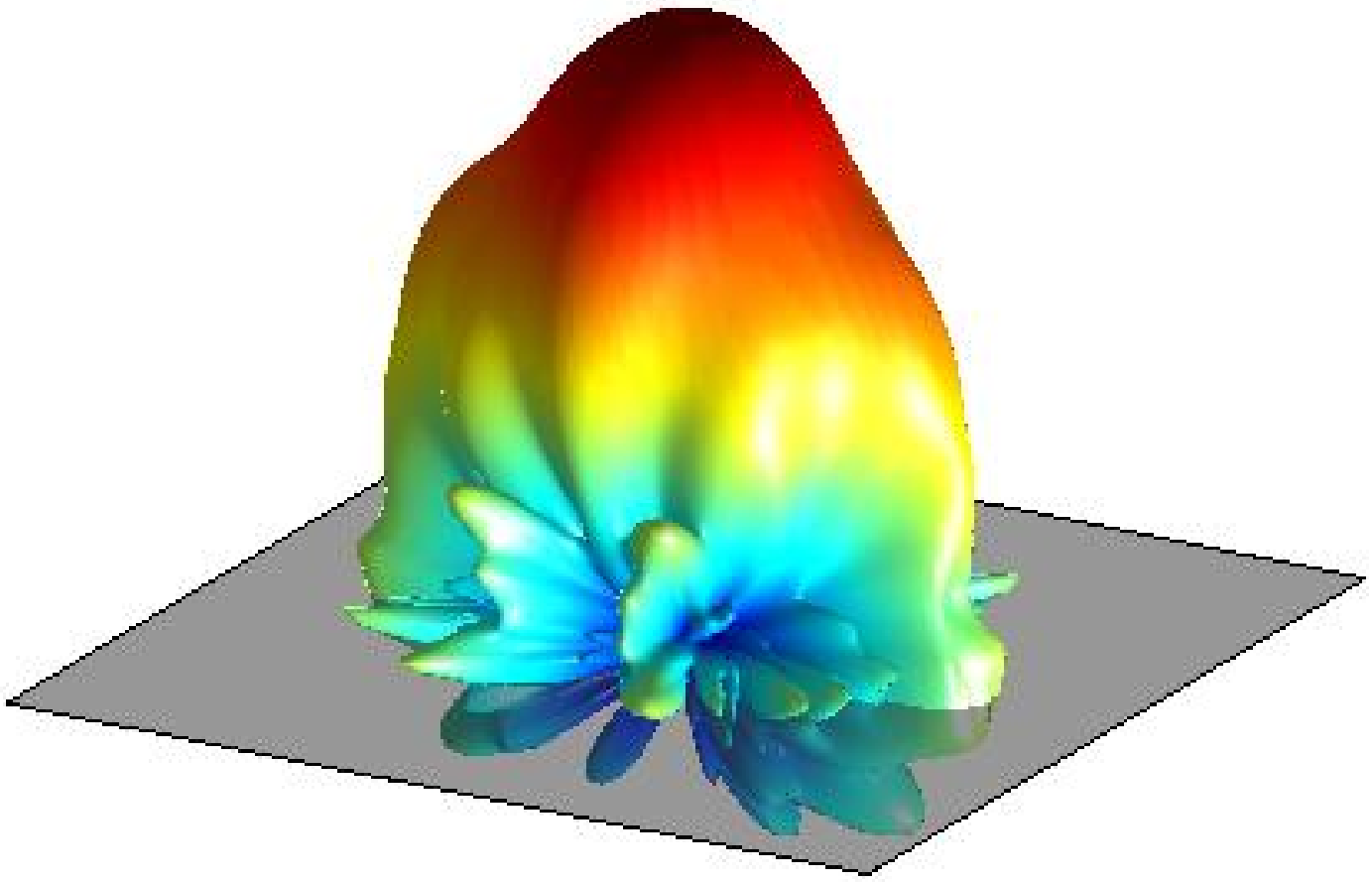

Polar plot of the fields at 50 cm

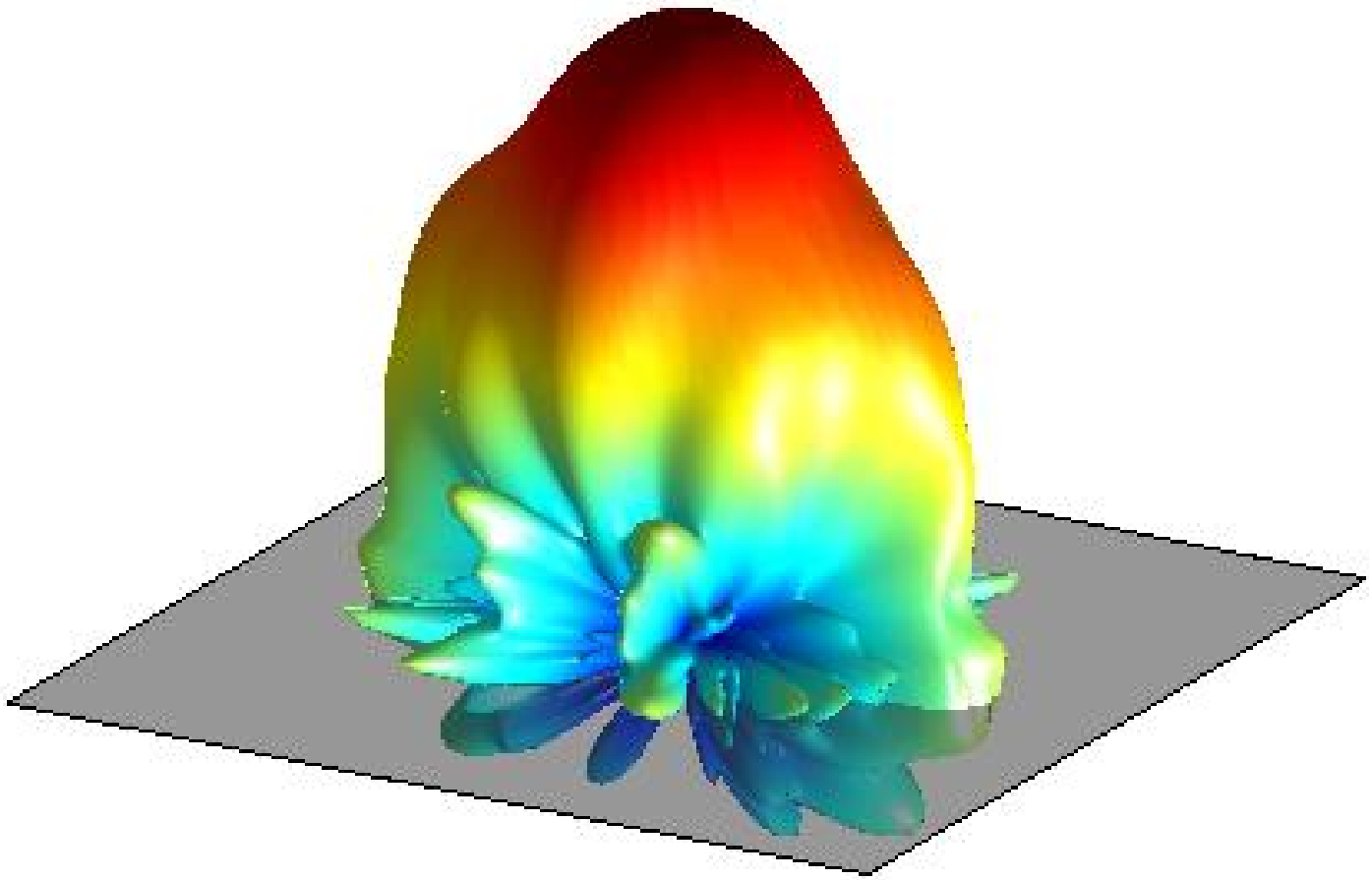

Polar plot of the fields at 1m

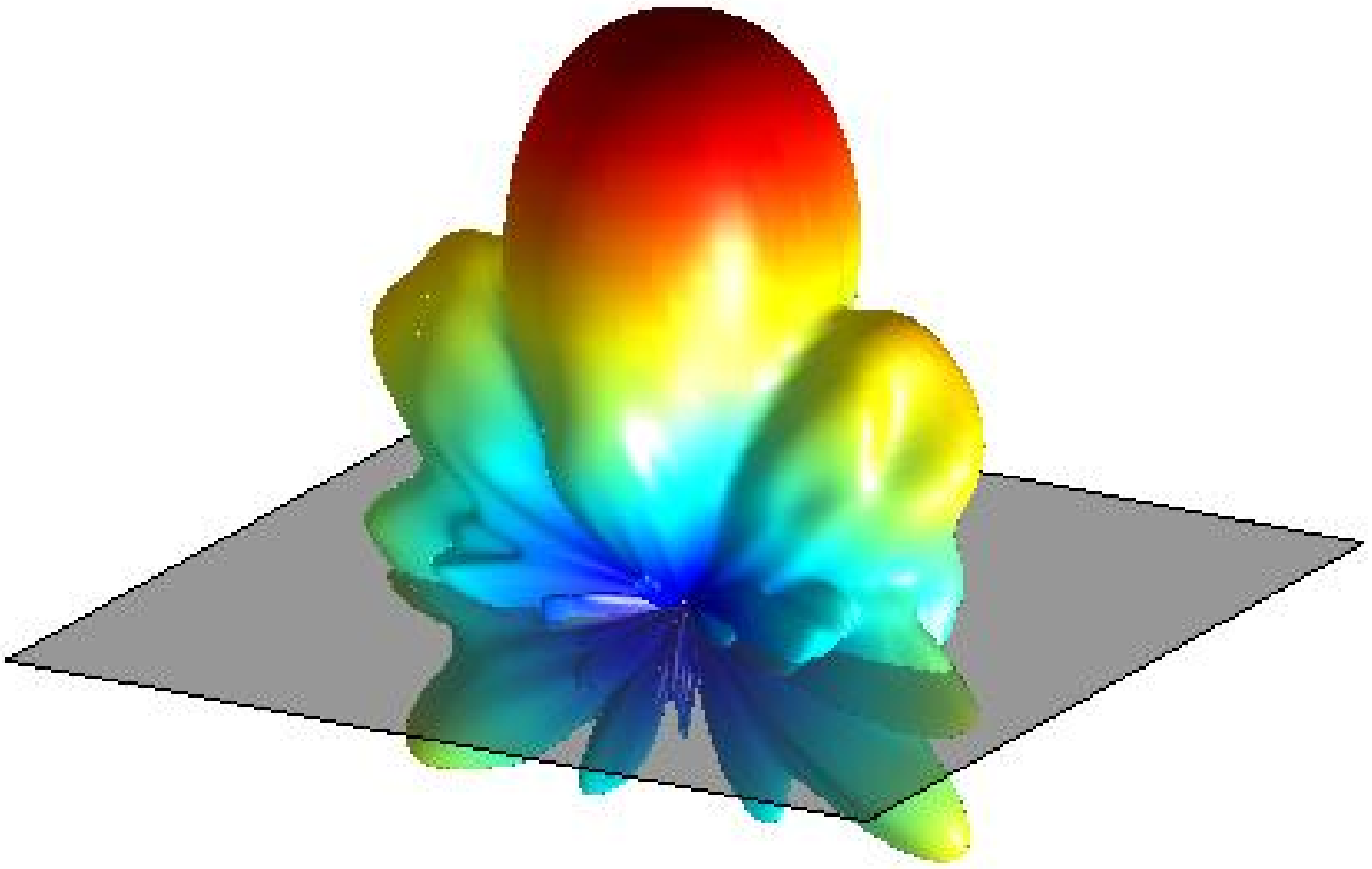

Polar plot of the fields at 100m

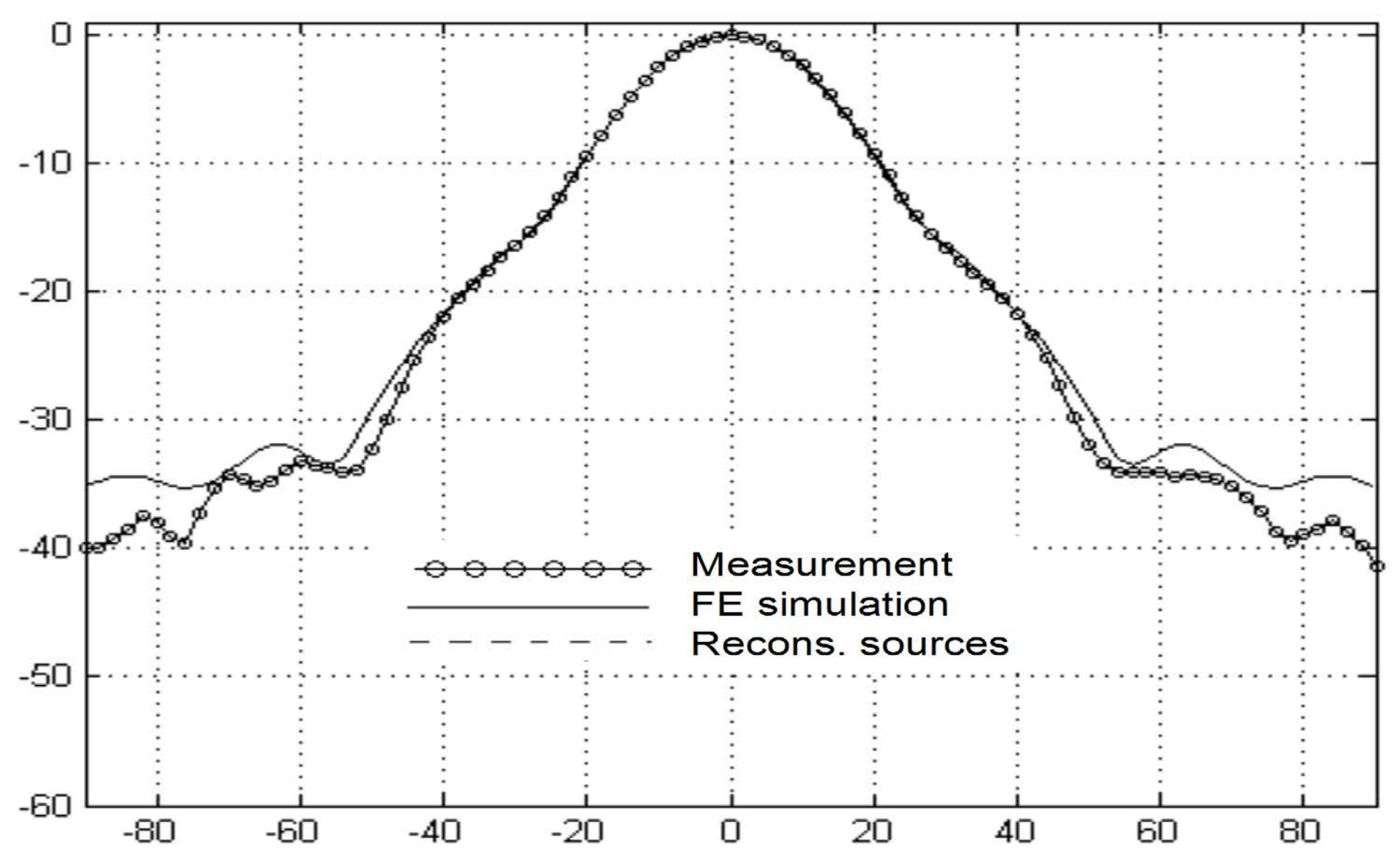

Comparison of the Far Field for Finite Element , this method and Measurements

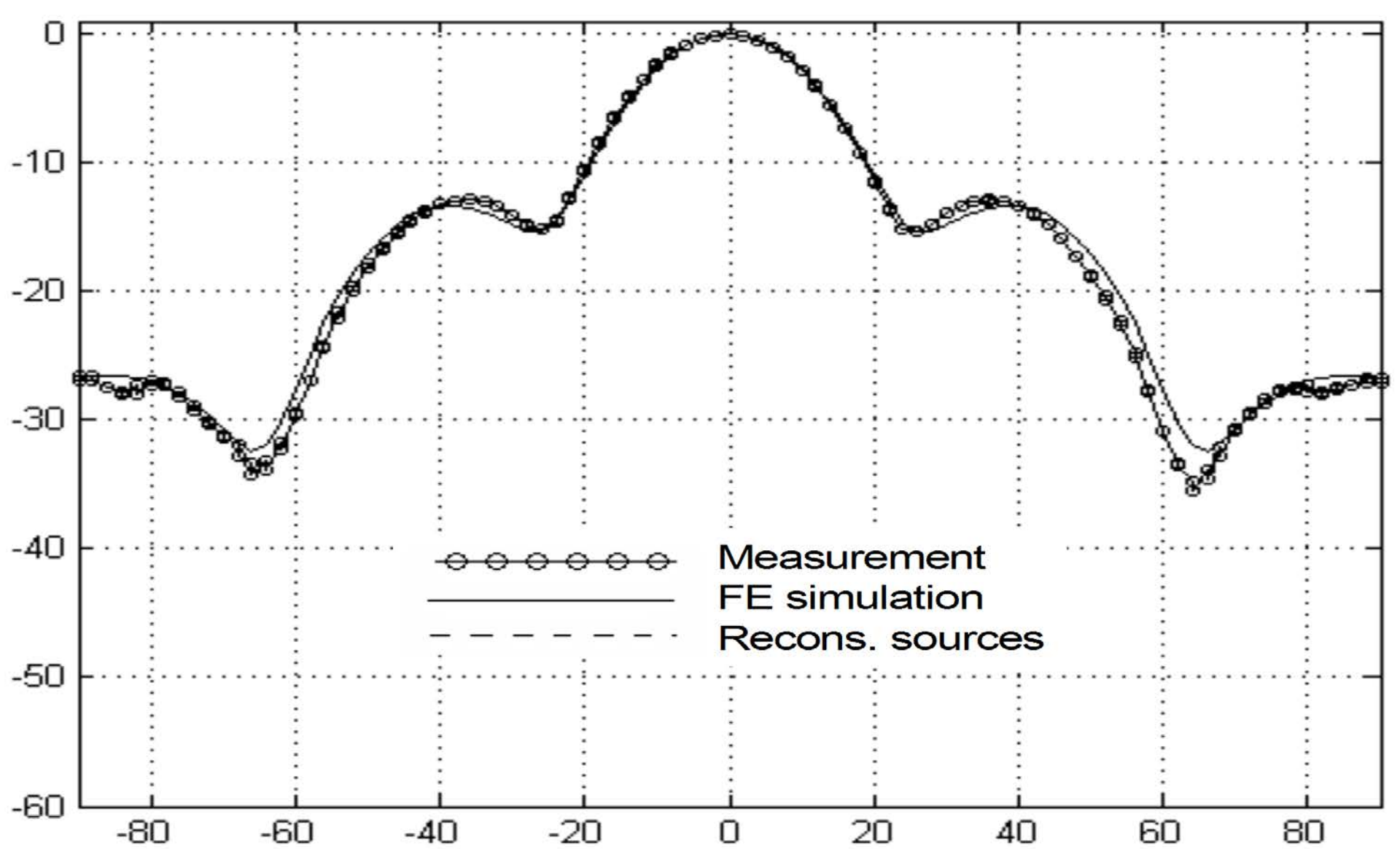

Comparison of the Far Field for Finite Element , this method and Measurements

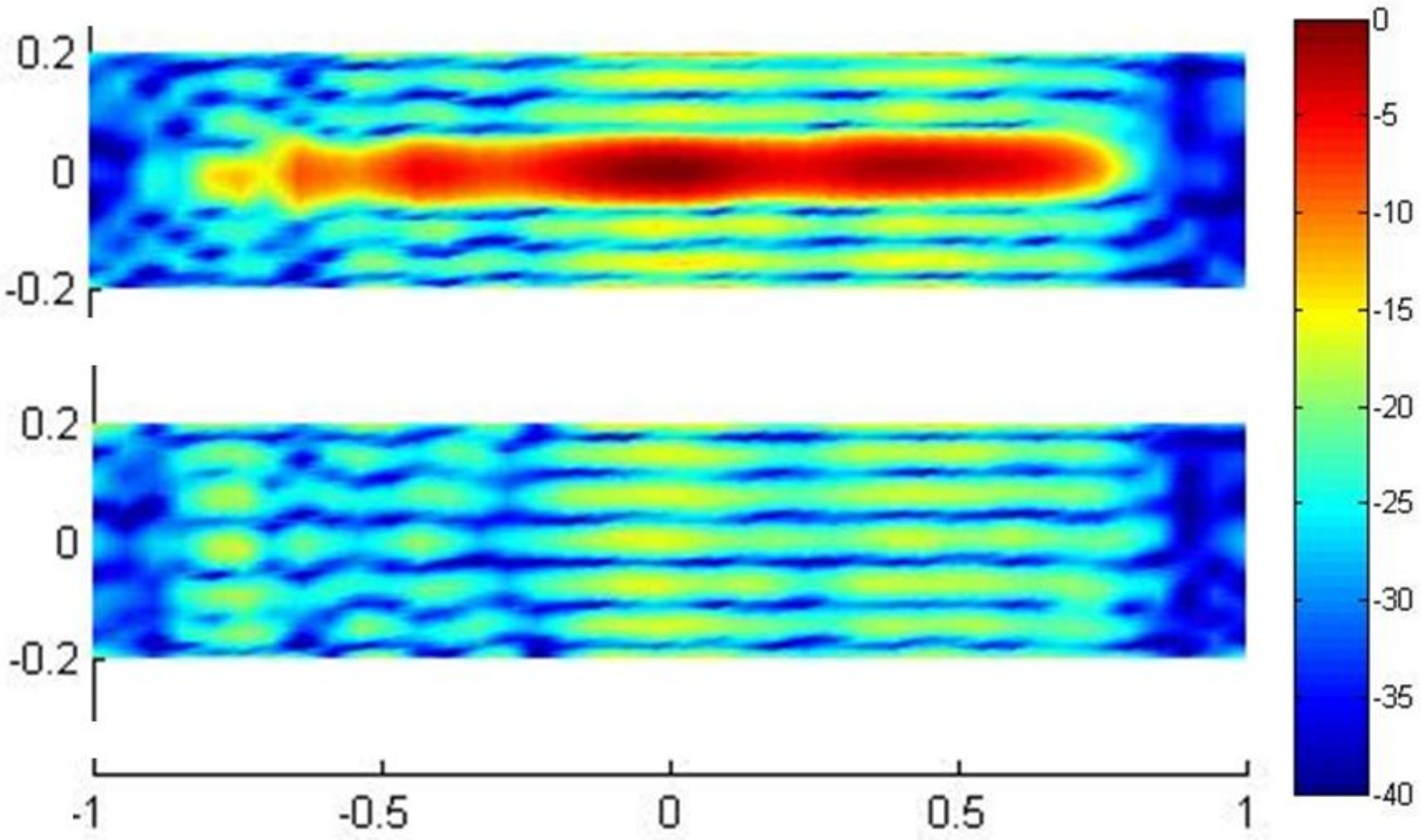

F=1800 MHz; Planes located at z1 = 0, and z2 = –0.2 m;
A planar domain of size 2.0 m × 0.4 m (antenna: 1.6 m × 0.3 m)
EqMC consisted of 120 × 40 Hertzian dipoles
as basis functions

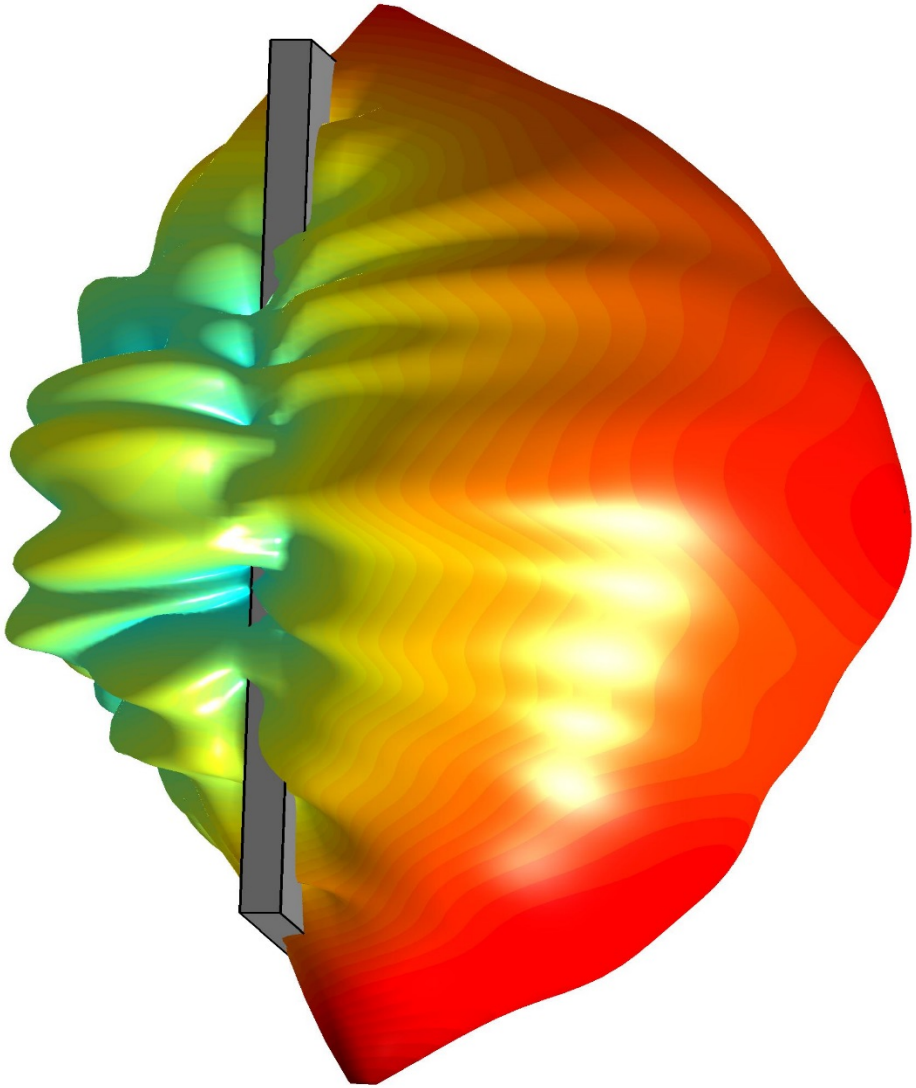

Polar plot of the fields at 50cm

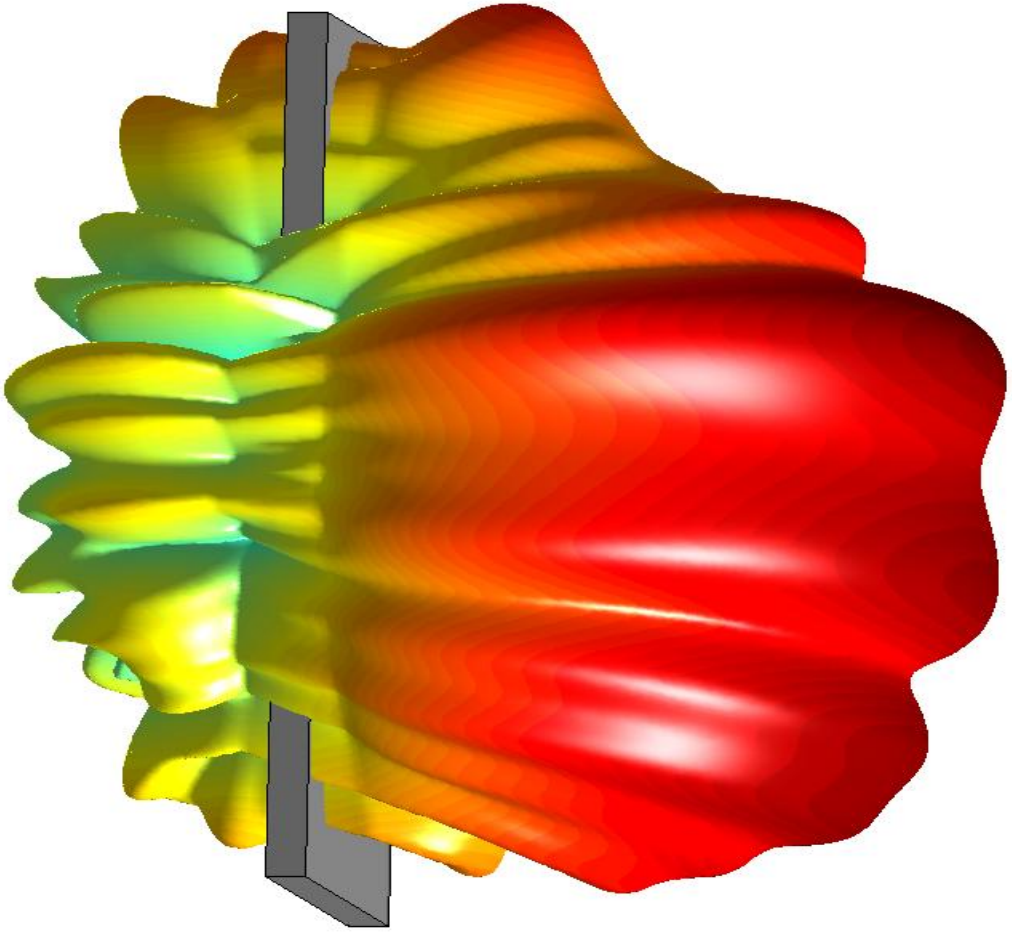

Polar plot of the fields at 1m

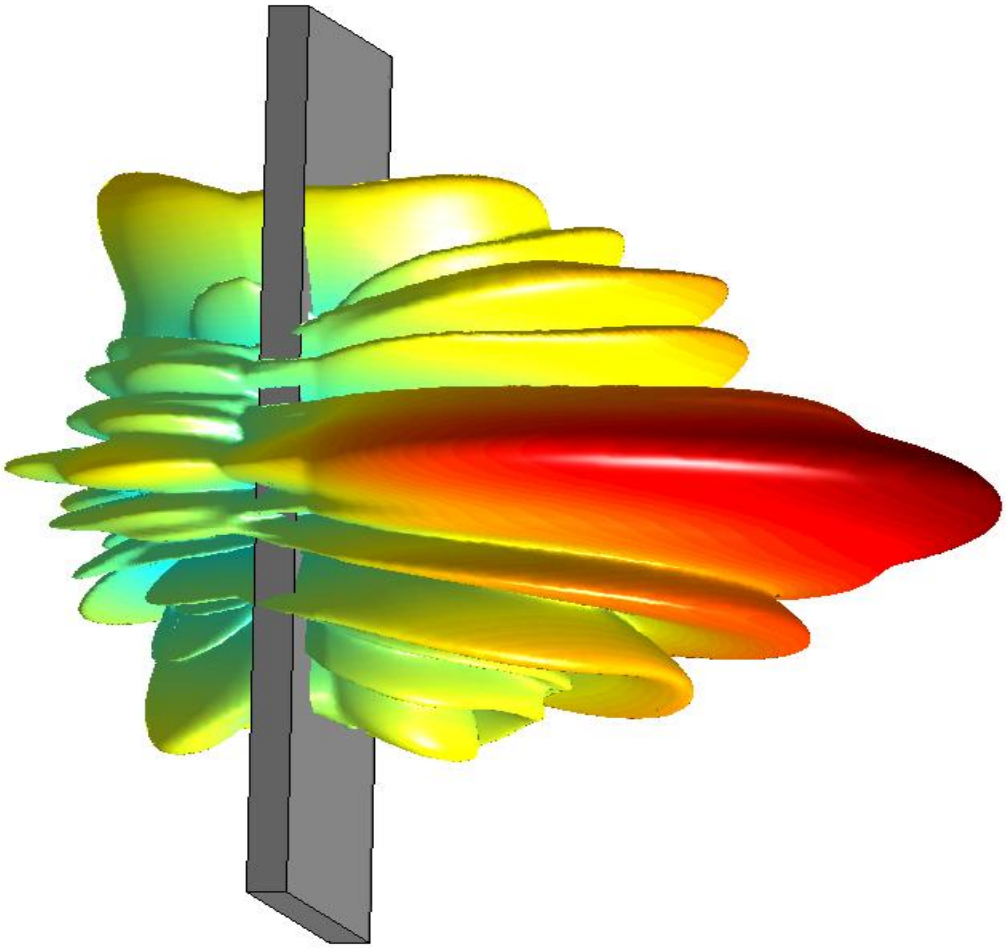

Polar plot of the fields at 100m

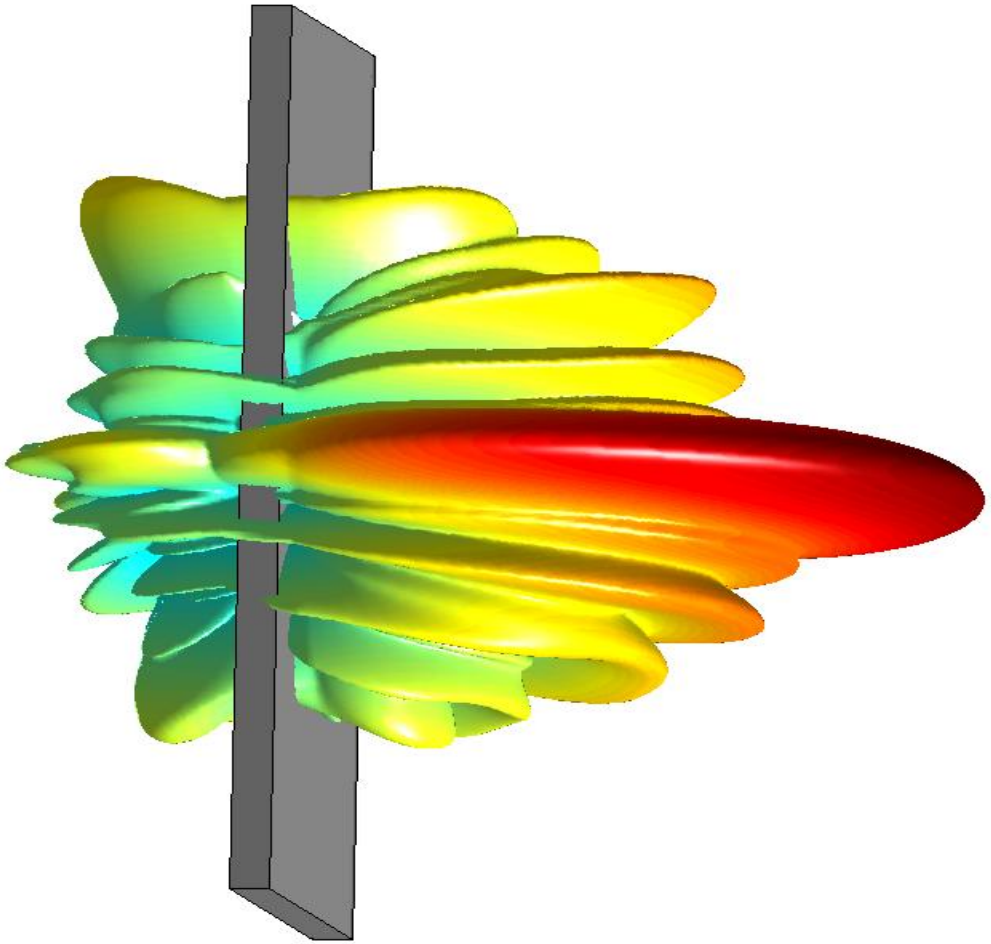

Polar plot of the fields at 1000m

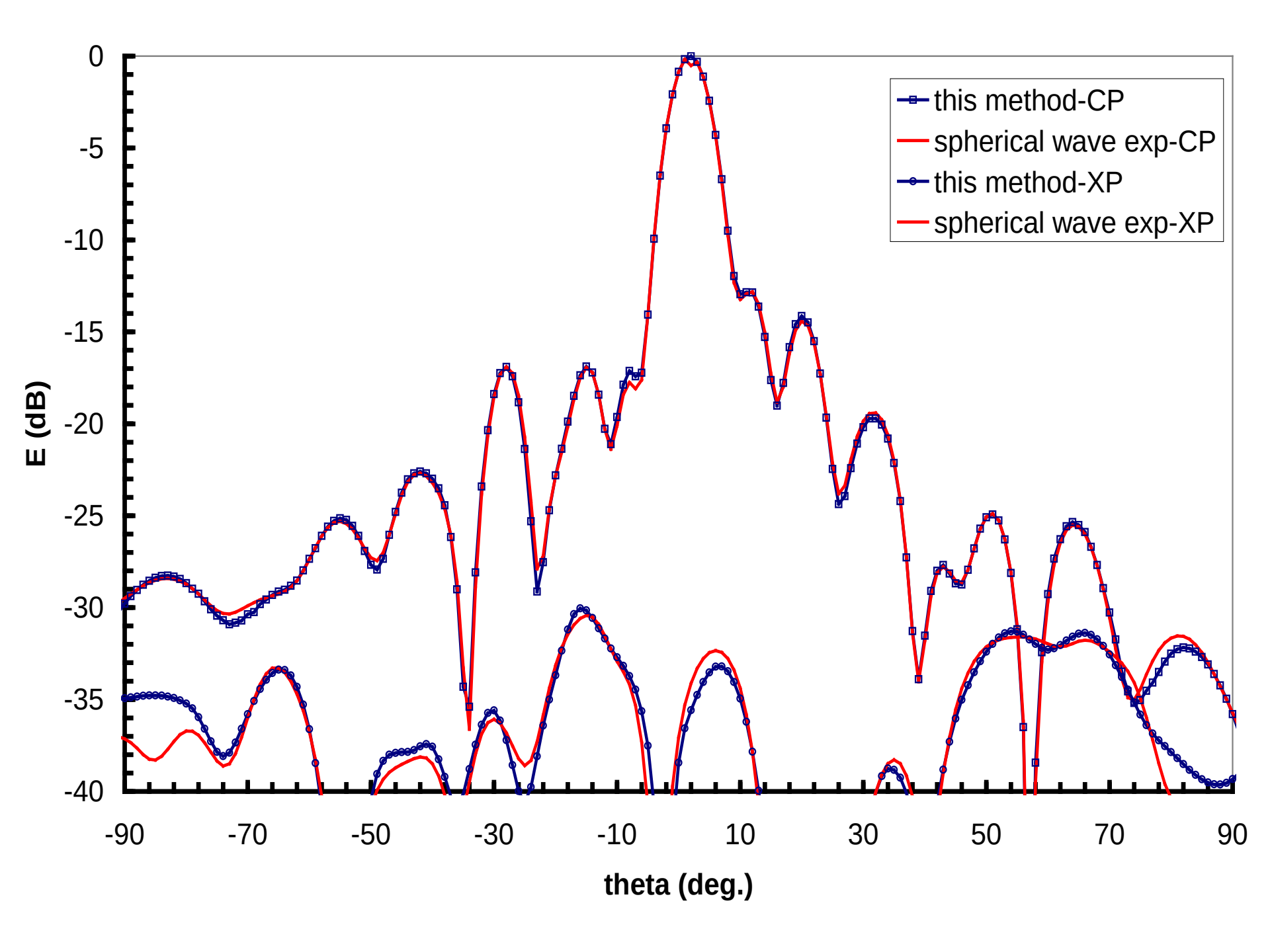
this method-CP
spherical wave exp-CP
this method-XP
spherical wave exp-XP
E (dB)
0
-5
-10
-15
-20
-25
-30
-35
-40
-90
-70
-50
-30
-10
10
30
50
70
90
theta (deg.)

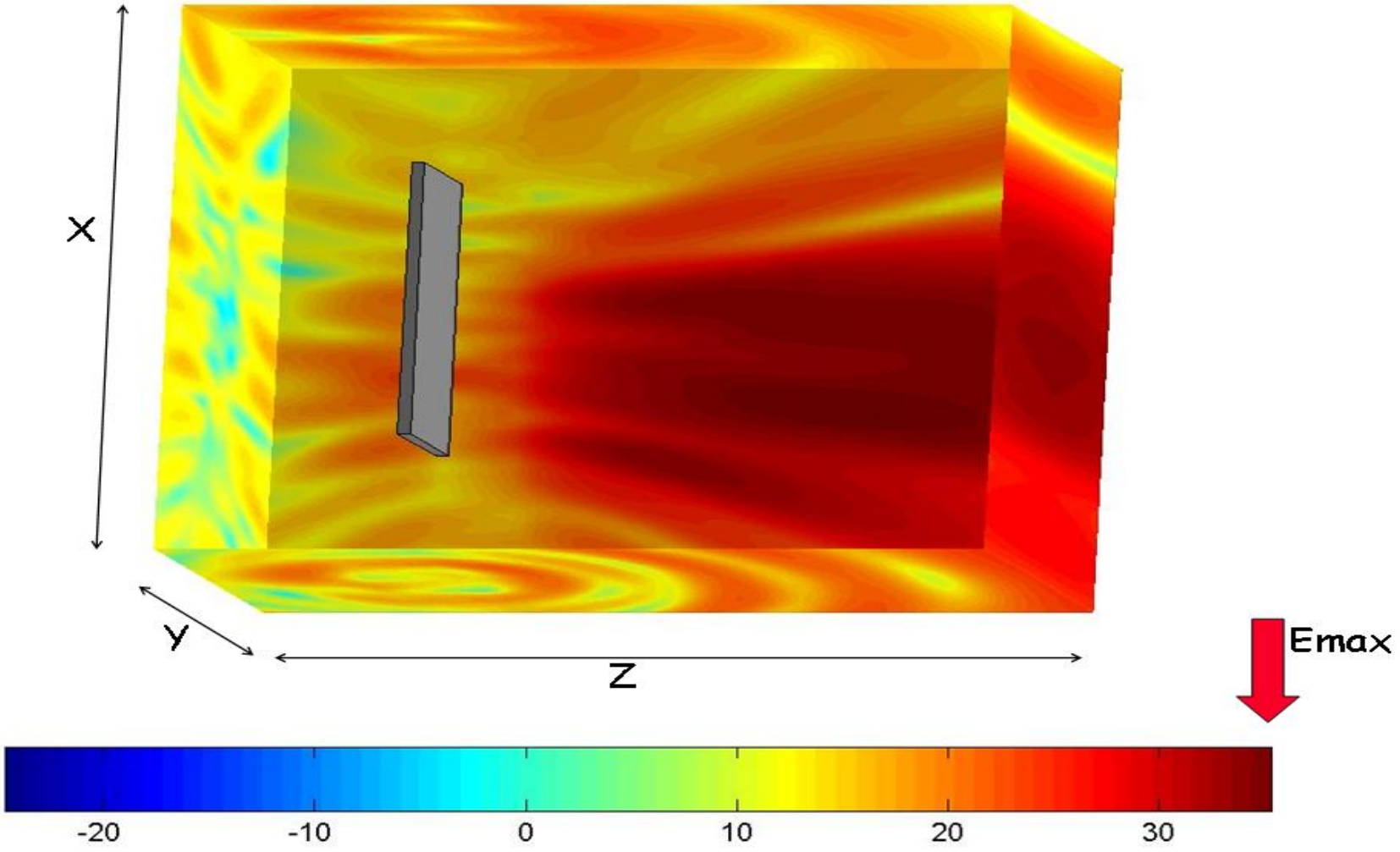

Box size around the antenna 3 m × 2 m × 4 m,
EIRP value of 1300 Watts ;
For Spain *Emax* = 58.34 V/m (35.3 dBV/m)

Equivalent problem

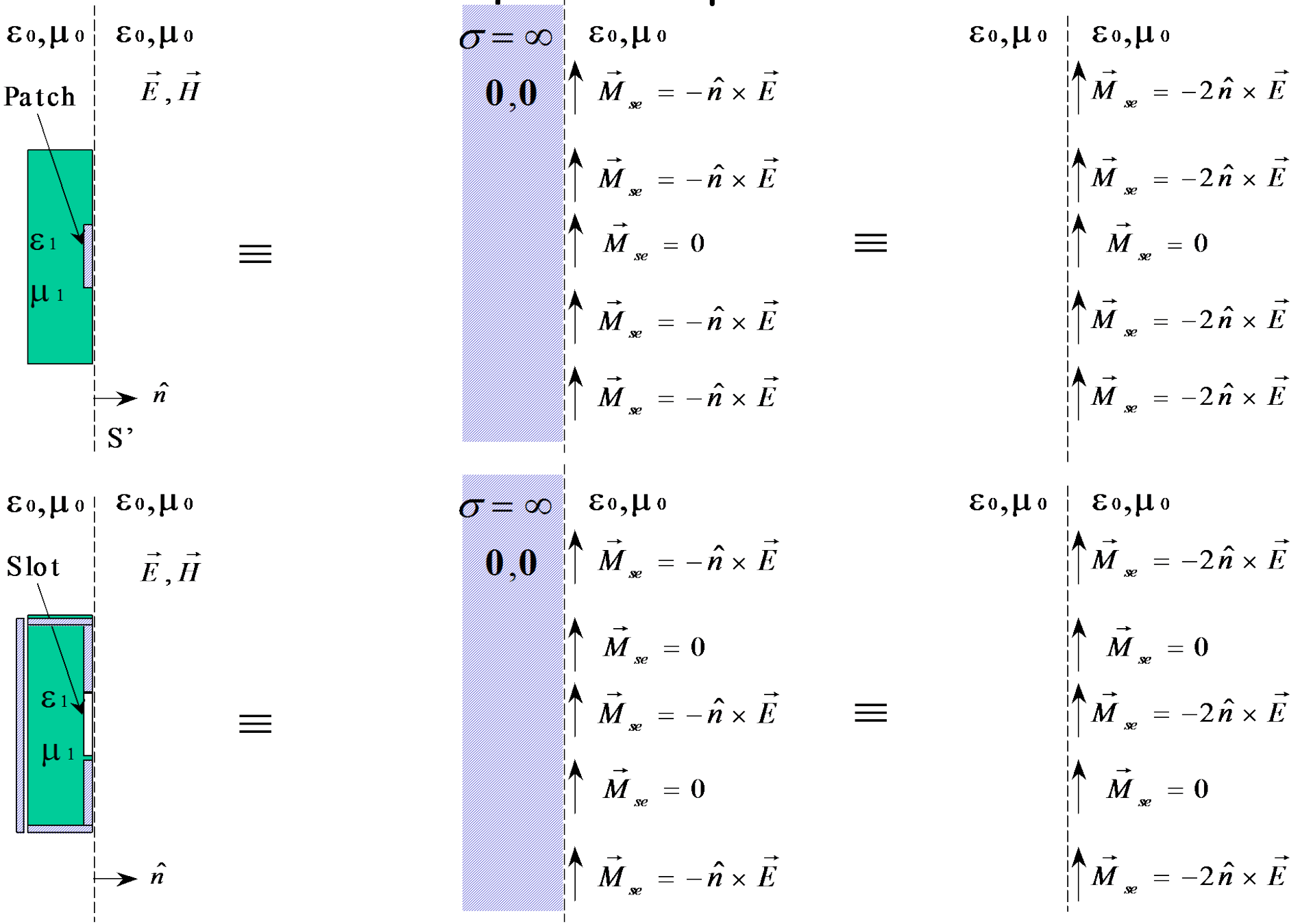

Proposed direct optimization

Ampl. Data - Scanning
$|E_{1,meas}|$, $|E_{2.meas}|$,..

Establishment of Equivalent problem

$$\vec{E}(\vec{M}) = \int_{source\ domain} \vec{M} \cdot Green\_func \cdot ds$$

$$\vec{E}(\vec{M}) \cdot \vec{E}^{*}(\vec{M}) - \vec{E}_{meas} \cdot \vec{E}^{*}_{meas} = 0$$

Numerical solving: optimize cost function

$$\min \quad F\left(\sum_{n} \left\| \vec{E}_n \cdot \vec{E}^{*}_n - \vec{E}_{n,meas} \cdot \vec{E}^{*}_{n,meas} \right\| \right), \quad n = 1,..,N$$

N arbitrary scanning points

$\vec{M}$, sources

$$\mathbf{E}_{\text{meas},\,x} = -\mathbf{G}\mathbf{M}_y$$

$$\mathbf{E}_{\text{meas},\,y} = \mathbf{G}\mathbf{M}_x$$

$$\mathbf{G}_{k,l} = \int_{\Omega_l}\int \frac{e^{-jk_0R}}{4\pi R^2}(z_k - z')\left[jk_0 + \frac{1}{R}\right] ds'$$

Matrix Equation: G M = E

Amplitude Only

Matrix Equation: G M = |E|

Results

From synthesized data:

- Chessboard-like magnetic current density

From measured data:

"Splas" antenna: Remote user terminal of a CDMA satellite system. (Prodat) with Reflector and splash plate (subreflector) antenna

Reconstructed sources of the "chessboard" magnetic current

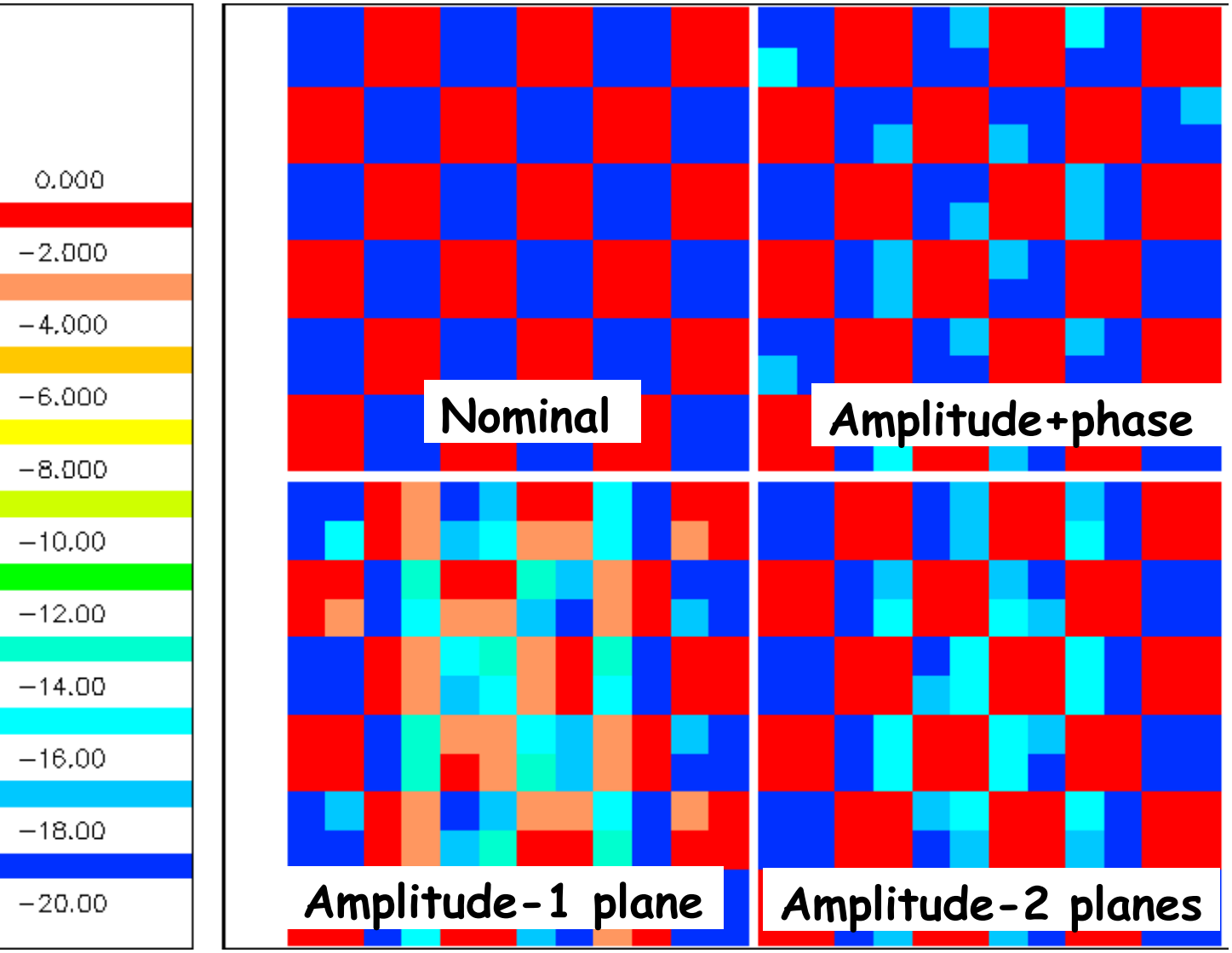

Nom. Source:
4λx 4λ
12x12 source cells

Scanning:
planar,2 planes
of 8λx 8λ
(160x160 points)
R1= 2λ
R2= 4λ

Source recons:
(same nominal)

Far-field "chessboard" magnetic current

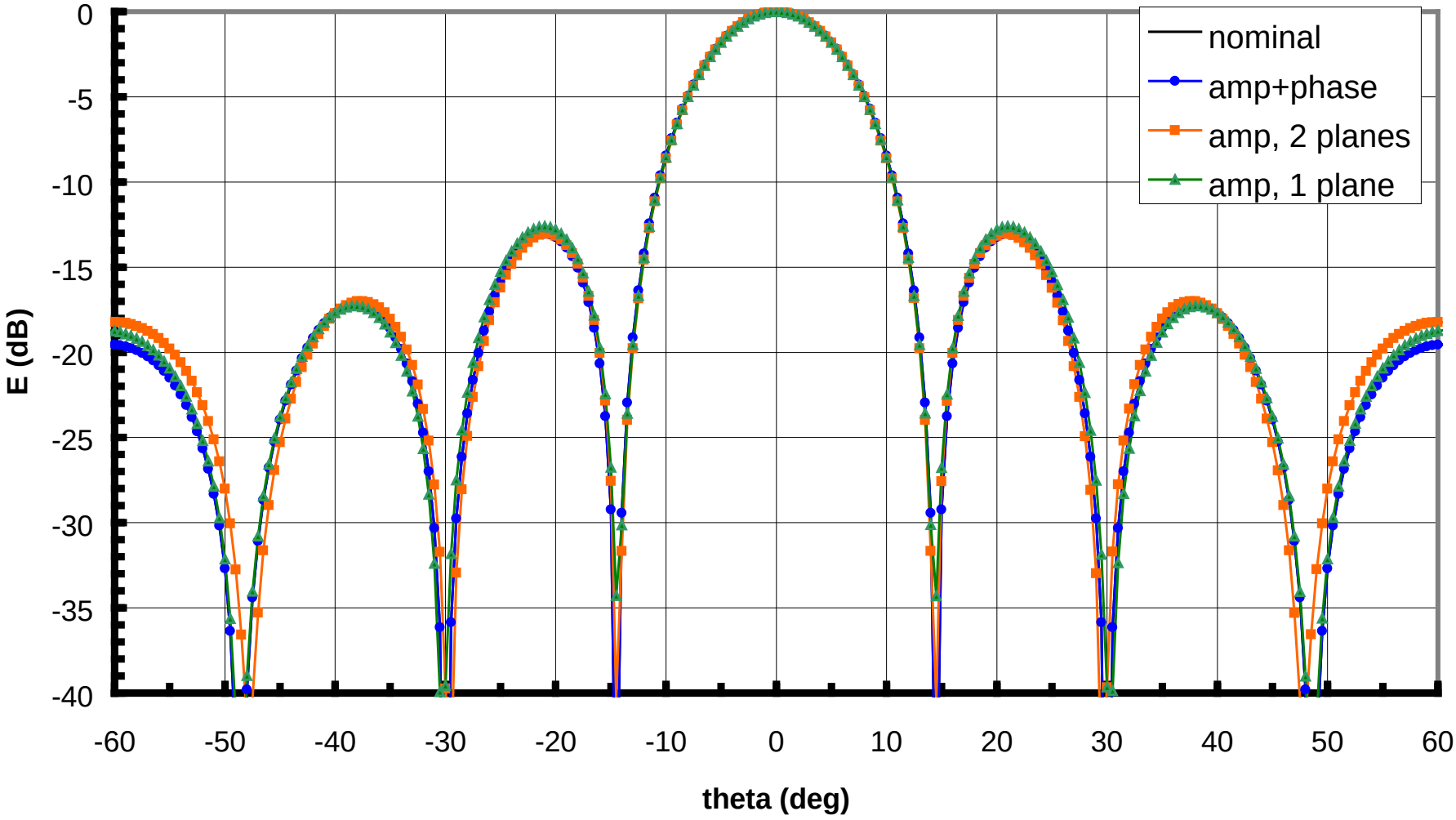

Convergence of iterative CG solution "chessboard"

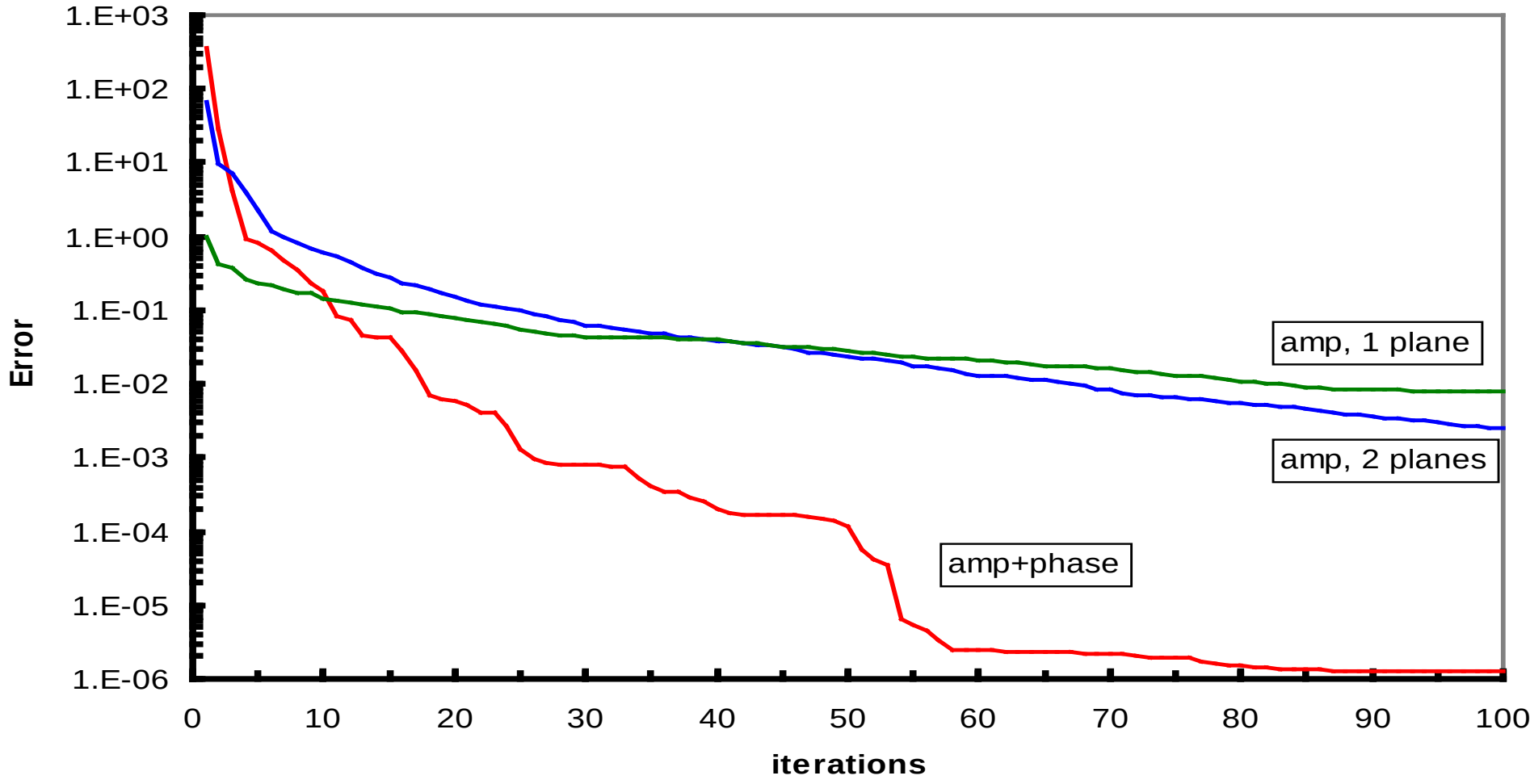

Results from measurements, "splas"

Antenna: Remote user terminal of a CDMA satellite system (Prodat)

- Reflector and splash plate (subreflector) antenna
- Diameter=0.4m
- Freq=12,625 GHz, linear pol.

Scanning:

Planar, 0.88m×0.88m, 88x88 field points.

- R_1=0.4 m, R_2=1.0m

Measurement facility

Laboratorio de Ensayos, Secr. Gral. Comunicaciones (MCYT), El Casar, Spain

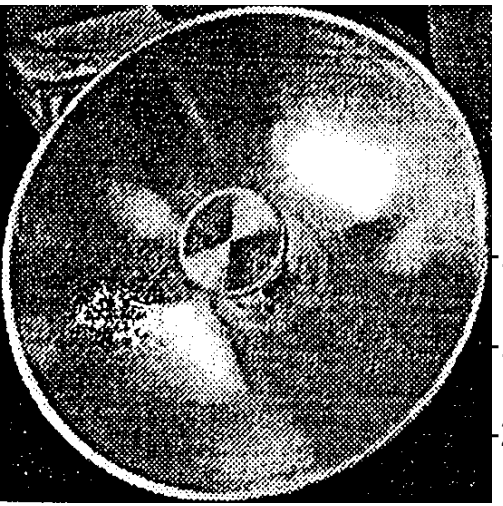

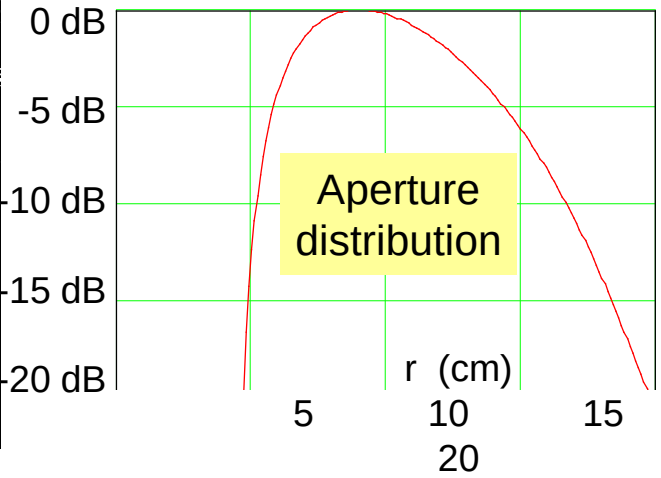

Reconstruction of sources, "splas"

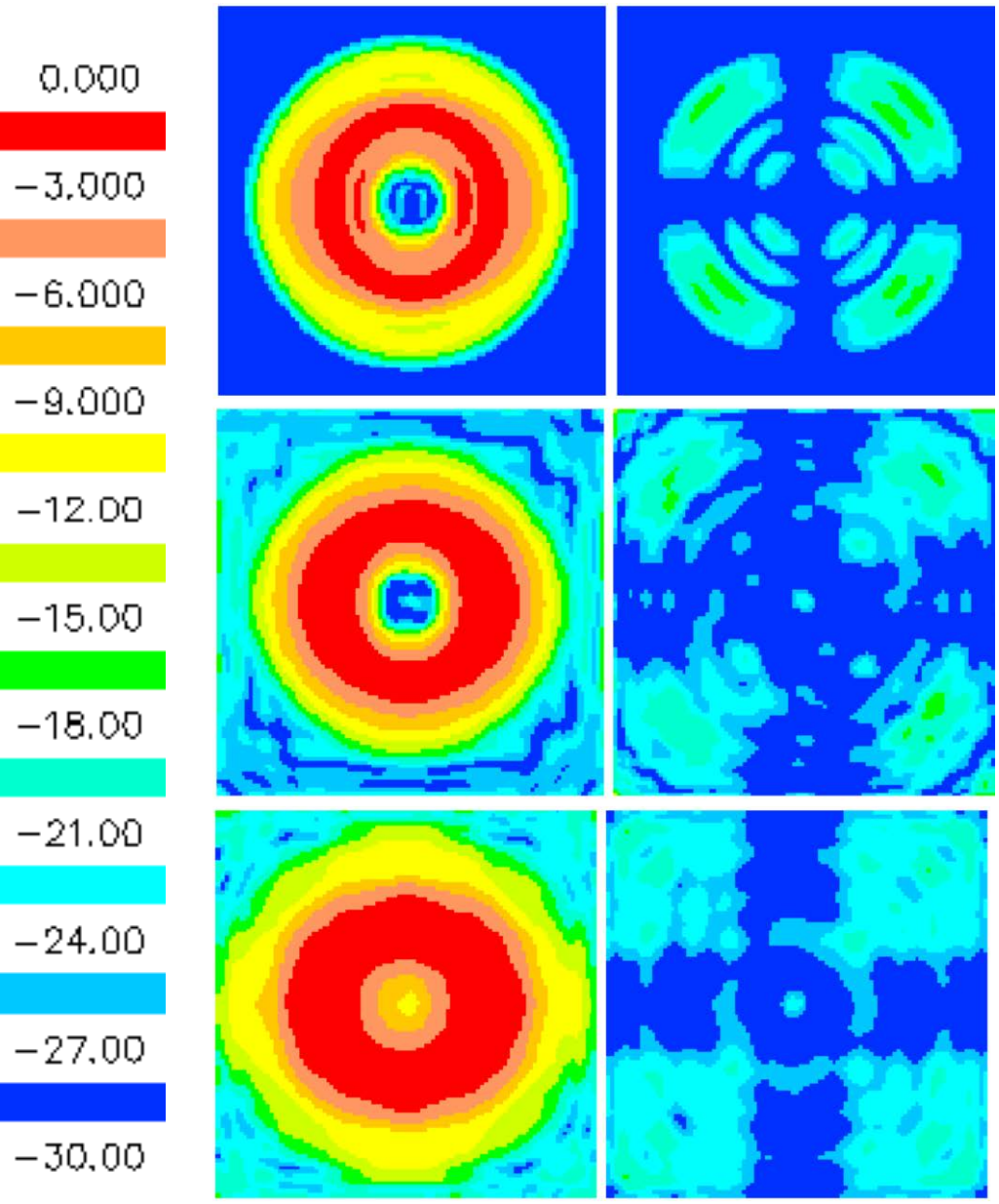

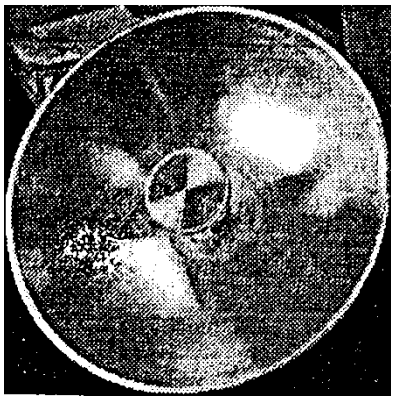

Electric field (Ex, Ey) at the aperture of the "splas" antenna.

a) from amplitude and phase
b) amplitude 2 planes
c) amplitude 1 plane.

Far-field, φ=0 –plane , "splas"

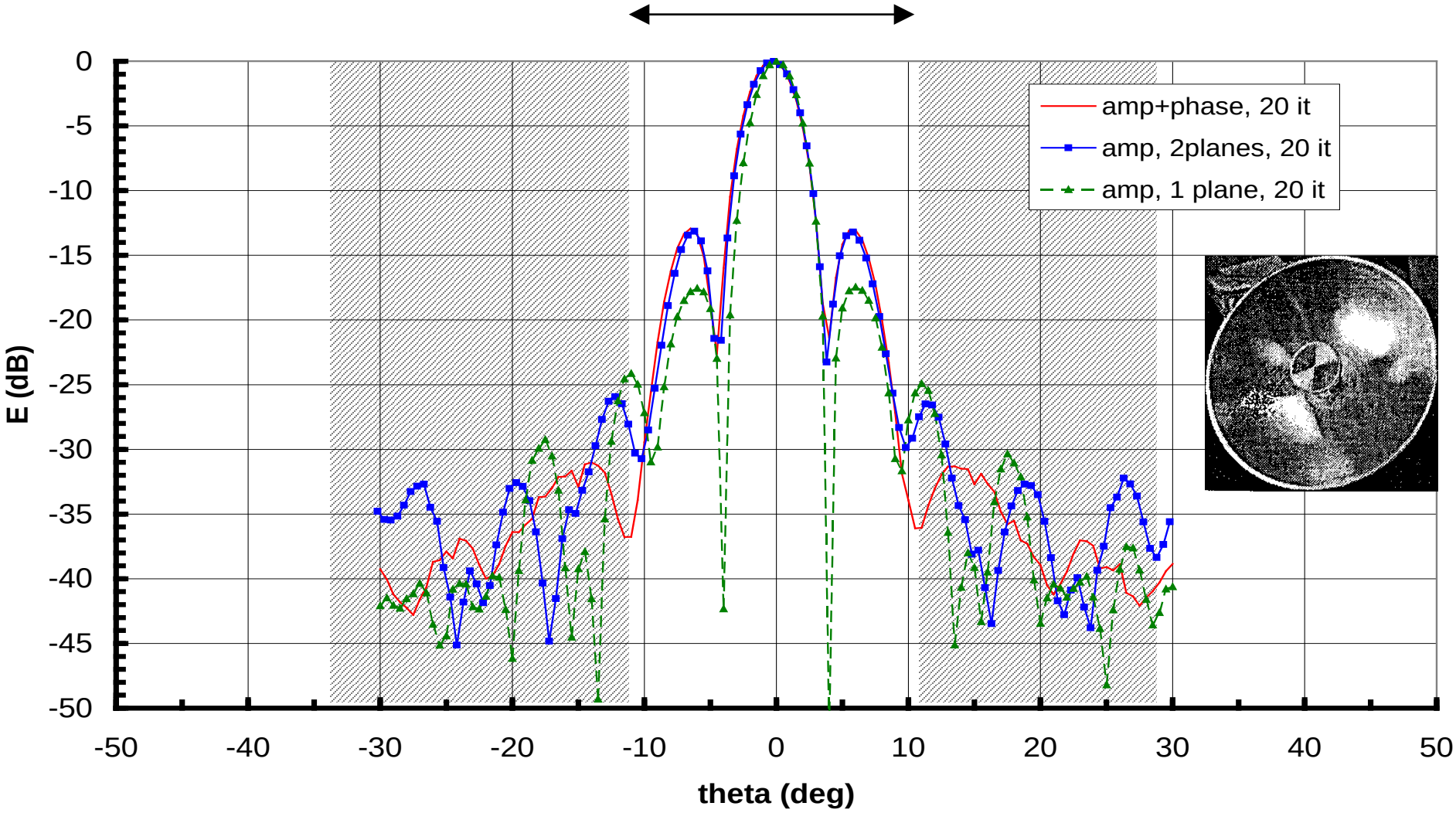

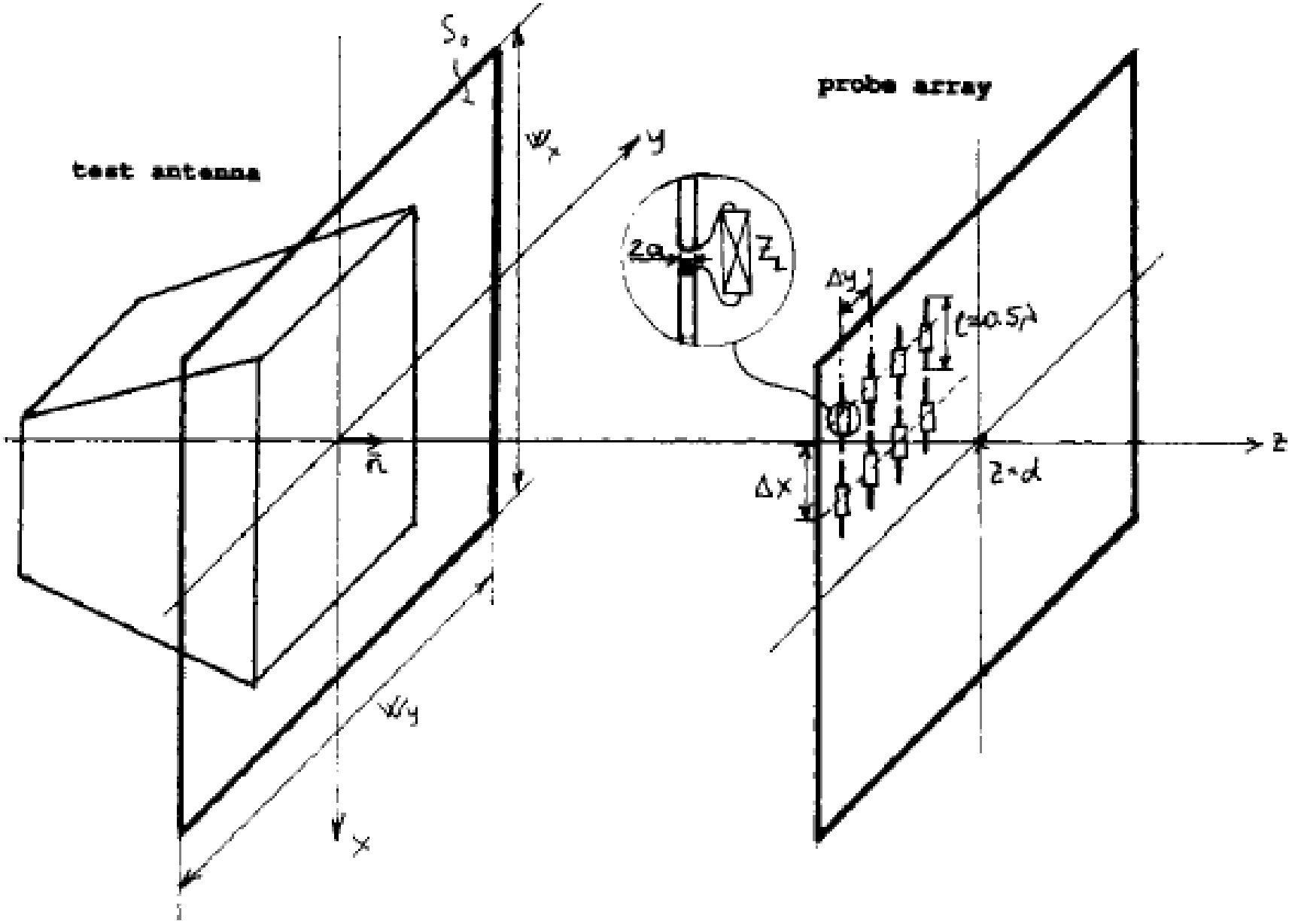

Planar near-field measurement using phased array as probe antenna.

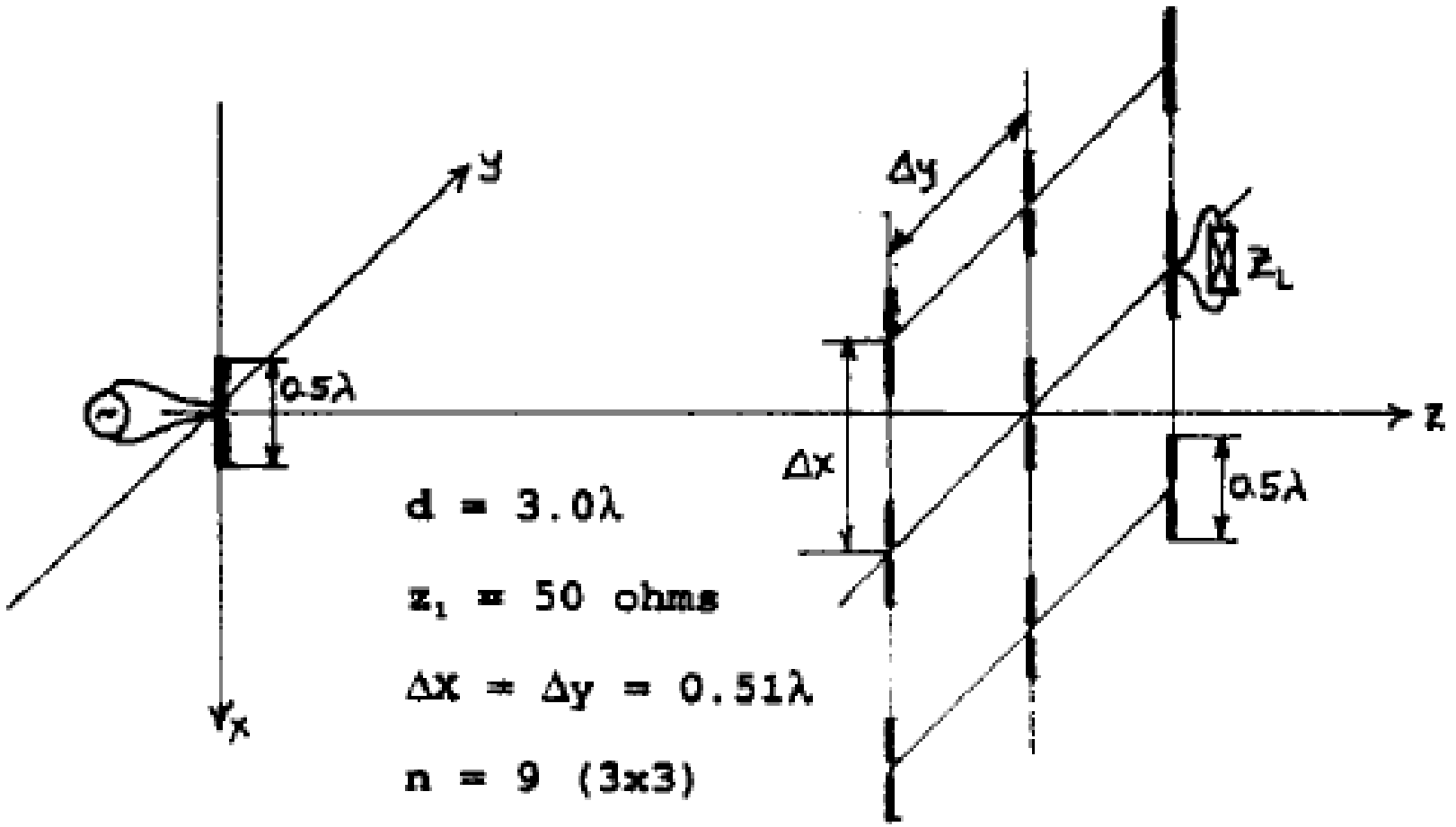

Fig. 4. Planar near-field measurement configuration. The test antenna is a resonant size electric dipole. The probe antenna is a phased array ($n = 9$).

TABLE I

INPUT IMPEDANCE OF THE TEST ANTENNA AS A FUNCTION OF THE NUMBER OF ELEMENTS OF PHASED ARRAY PROBE

n	Z_{in}
1	$73.402 + j41.654$
9	$74.398 + j39.747$
25	$71.644 + j39.339$
49	$73.218 + j40.535$
81	$72.113 + j39.696$
121	$73.149 + j39.705$
169	$72.874 + j40.454$
225	$72.350 + j40.256$
441	$72.948 + j39.716$
961	$72.776 + j40.387$
Single	$73.129 + j41.797$

Sub-wavelength Imaging

1. **Fields need not be sampled at the Nyquist rate of 0.5λ. The fields can be computed further apart.**
2. **Existence of evanescent waves improves the resolution of the reconstruction of the sources. The presence of evanescent waves does not make the solution procedure unstable.**
3. **Sub-wavelength resolution of imaging as the sampling is relegated to the source plane.**
4. **Fields need not be measured on a canonical surface. It can be measured along a line, along a plane, or over an arbitrary shaped surface.**

Sub-wavelength Imaging

5. **No need to mechanically move a probe. One could place an array of receiving antennas.**
6. **Truncation error in the measurement has less influence on the accuracy of the source/far field reconstruction.**
7. **For planar measurement planes, this method is more accurate than the conventional Fourier techniques at the expense of 3 to 4 times slower computationally than the FFT as it is implemented through the conjugate gradient and the FFT technique.**

Sub-wavelength Imaging

8. **Can easily be extended to amplitude-only data measured over one plane or over multiple planes.**
9. **This methodology is based on Maxwellian Physics and therefore the transformations are quite accurate and in most cases even exact.**